HELSINGIN YLIOPISTO
HELSINGFORS UNIVERSITET
UNIVERSITY OF HELSINKI

MASTER'S THESIS
DEPARTMENT OF GEOSCIENCE AND GEOGRAPHY
SOLID EARTH GEOPHYSICS

BOREHOLE MAGNETIC RESONANCE METHOD IN HARD ROCK ENVIRONMENTS: A CASE STUDY FROM THE OLKILUOTO SPENT NUCLEAR FUEL REPOSITORY SITE

Aino Karjalainen
12/2020

Supervisors:
Emilia Koivisto (University of Helsinki)
Minna Kuusisto (Posiva Oy)
Kirsti Korkka-Niemi (University of Helsinki)

University of Helsinki
Faculty of Science
Department of Geoscience and Geography
PL 64 (Gustaf Hällströmin katu 2)
00014 Helsingin yliopisto

HELSINGIN YLIOPISTO
HELSINGFORS UNIVERSITET
UNIVERSITY OF HELSINKI
MATEMAATTIS-LUONNONTIETEELLINEN TIEDEKUNTA
MATEMATISK-NATURVETENSKAPLIGA FAKULTETEN
FACULTY OF SCIENCE

Tiedekunta - Fakultet - Faculty	Koulutusohjelma - Utbildningsprogram - Degree programme	
Faculty of Science	Master's programme in geology and geophysics	
Tekijä - Författare - Author		
Aino Iida Elina Karjalainen		
Työn nimi - Arbetets titel - Title		
Borehole magnetic resonance method in hard rock environments: a case study from the Olkiluoto spent nuclear fuel repository site		
Opintosuunta - Studieinriktning – Study track		
Solid Earth Geophysics		
Työn laji - Arbetets art - Level	Aika - Datum - Month and year	Sivumäärä - Sidoantal - Number of pages
Master's thesis	2020	103 + 2 attachments

Tiivistelmä - Referat - Abstract

NMR Services Australia (NMRSA) Pty Ltd has developed a Borehole Magnetic Resonance (BMR) tool which is based on the principles of nuclear magnetic resonance (NMR). Drillhole NMR tools have been used mostly in sedimentary environments for oil and gas exploration while applications in hard, heterogeneous, crystalline bedrock are still lacking. This study aims to test the BMR method in a hard rock environment, and for determining hydrogeological parameters in the spent nuclear fuel disposal site, the Olkiluoto island. Essentially, the objective is to design an optimal BMR data processing workflow and calibrate the estimated hydrogeological parameters, currently optimized for data from sedimentary environments, to suit the crystalline bedrock.

For testing the BMR method in hard, crystalline bedrock, Posiva Oy, the Finnish expert organization responsible of spent nuclear fuel disposal, made test measurements in the drillholes of the spent nuclear fuel repository site, island of Olkiluoto. The collected data was processed with WellCAD software using additional NMR module. The BMR tool derives T_2 distribution (representing pore size distribution), total porosity, bound water and moveable water volumes and permeability calculated with two different models. Some processing parameters (main/burst sequence, moving averages, temperature gradient, cutoff values) were tested and adjusted to fit into crystalline bedrock. Magnetizing material of the surface environment strongly disturbed the uppermost ~20.0 m portions of the measurement data. Some noise was encountered also deep in bedrock, which was cut away from the signal. A list of criteria was created for recognizing noise.

The BMR data was compared with other drillhole data acquired by Posiva, i.e. fracture and lithology logs, seismic velocities and hydrogeological measurements. It was observed that the T_2 distribution and total porosity correlate rather well to logged fractures and seismic velocities. Lithological variations did not correlate to BMR consistently, mostly because of the strong dependency on fracturing. Permeabilities were compared to earlier conducted hydrogeological measurements, with an intention to calibrate the permeability calculation models. However, this proved to be challenging due to the significant differences of the BMR method and conventional hydrogeological measurements. Preferably, the permeability models should be calibrated by laboratory calibration of the drillhole core, and possibly a new permeability model suitable for crystalline bedrock should be created.

Avainsanat - Nyckelord - Keywords

Nuclear magnetic resonance, borehole magnetic resonance, spent nuclear fuel repository, Olkiluoto, borehole geophysics

Säilytyspaikka - Förvaringsställe - Where deposited

HELDA- Digital repository of the university of Helsinki

Muita tietoja - Övriga uppgifter - Additional information

38 figures and 5 tables

HELSINGIN YLIOPISTO
HELSINGFORS UNIVERSITET
UNIVERSITY OF HELSINKI
MATEMAATTIS-LUONNONTIETEELLINEN TIEDEKUNTA
MATEMATISK-NATURVETENSKAPLIGA FAKULTETEN
FACULTY OF SCIENCE

Tiedekunta - Fakultet - Faculty	Koulutusohjelma - Utbildningsprogram - Degree programme	
Matemaattis-luonnontieteellinen tiedekunta	Geologian ja geofysiikan maisteriohjelma	
Tekijä - Författare - Author		
Aino Iida Elina Karjalainen		
Työn nimi - Arbetets titel - Title		
Ydinmagneettinen resonanssi –menetelmä kiteisessä kallioperässä: tapaustutkimus Olkiluodon käytetyn ydinpolttoaineen loppusijoituskohteesta		
Opintosuunta - Studieinriktning – Study track		
Kiinteän maan geofysiikka		
Työn laji - Arbetets art - Level	Aika - Datum - Month and year	Sivumäärä - Sidoantal - Number of pages
Pro Gradu	2020	103 + 2 liitettä

Tiivistelmä - Referat - Abstract

NMR Services Australia (NMRSA) Pty Ltd on kehittänyt BMR-kairareikälaitteen (englanniksi *borehole magnetic resonance*), joka perustuu ydinmagneettiseen resonanssiin (englanniksi *nuclear magnetic resonance*, NMR). NMR:ään perustuvia kairareikälaitteita on käytetty lähinnä sedimenttikiviympäristöissä öljyn- ja kaasunetsintään, mutta heterogeenisen, kiteisen kallioperän sovellukset ovat puuttuneet. Tämä tutkimus pyrkii testaamaan BMR-menetelmää kiteisessä kallioperässä ja määrittämään hydrogeologisia parametreja käytetyn ydinpolttoaineen loppusijoituskohteessa Olkiluodossa. Tarkoituksena on suunnitella optimaalinen BMR-aineiston prosessointisekvenssi ja saada BMR-mittausten pohjalta määritellyt hydrogeologiset parametrit kalibroitua kiteiseen kallioperään.

Posiva Oy, asiantuntijaorganisaatio, joka on vastuussa käytetyn ydinpolttoaineen loppusijoituksesta, suoritti BMR-testimittauksia loppusijoituspaikalla Olkiluodossa testatakseen BMR:n soveltuvuutta kiteiseen kallioperään. Testimittauksista saatu aineisto prosessoitiin WellCAD-ohjelmiston NMR-laajennuksella. BMR-aineiston pohjalta voidaan tuottaa T_2-jakauma (edustaa huokoisuusjakaumaa), kokonaishuokoisuus, sitoutuneen ja liikkuvan veden tilavuudet ja permeabiliteetti laskettuna kahdella eri mallilla. Joitakin prosessointiparametreja (main/burst-sekvenssi, liukuva keskiarvo, lämpötilagradientti, cutoff-arvot) testattiin ajamalla testejä ja muokkaamalla parametrit sopivaksi kiteiseen kallioperään. Pintaympäristön magnetoituva materiaali häiritsi huomattavasti ylimpiä ~20.0 m osuuksia mittausaineistosta. Jonkin verran kohinaa, joka leikattiin pois varsinaisesta signaalista, havaittiin myös syvällä kairareiässä. Kohinan tunnistamiseksi laadittiin kriteeristö.

BMR-aineistoa verrattiin muihin Posivan kairareikäaineistoihin, mm. rako- ja litologialogeihin, seismisiin nopeuksiin ja hydrogeologisiin mittauksiin. Havaittiin, että T_2-jakauma ja kokonaishuokoisuus vertautuivat jokseenkin hyvin rakoihin ja seismisiin nopeuksiin. Litologian vaihtelu ei vertautunut BMR:ään järjestelmällisesti, johtuen erityisesti voimakkaasta korrelaatiosta rakoiluun. Permeabiliteetteja verrattiin muihin hydrogeologian mittaustuloksiin, tarkoituksena kalibroida permeabiliteettimallien laskukaavat kiteiseen kallioperään sopivaksi. Kalibrointi osoittautui kuitenkin haastavaksi, johtuen suurista eroista BMR:n ja perinteisten hydrogeologian kairareikämittausten välillä. Ideaalitilanteessa permeabiliteettimallit tulisi kalibroida laboratoriossa kairasydämeen. Mahdollisesti tulisi myös luoda uusi, kiteiseen kallioperään sopiva permeabiliteettimalli.

Avainsanat - Nyckelord - Keywords

Ydinmagneettinen resonanssi, kairareikien magneettinen resonanssi, käytetyn ydinpolttoaineen loppusijoitus, Olkiluoto, kairareikägeofysiikka

Säilytyspaikka - Förvaringsställe - Where deposited

HELDA- Helsingin yliopiston digitaalinen arkisto

Muita tietoja - Övriga uppgifter - Additional information

38 kuvaa ja 5 taulukkoa

TABLE OF CONTENTS

1. INTRODUCTION

1.1 Background of the present study

Nuclear magnetic resonance (NMR) phenomenon was discovered by Bloch (1946) and Purcell et al. (1946). In NMR, atomic nuclei respond to an applied external magnetic field and precess. When the precessing nuclei interact with the magnetic field, measurable signals are produced. This finding was soon applied to well logging for oil and gas exploration (e.g. Brown and Gamson 1960, Kleinberg and Jackson 2001, Nikias and Eyraud 1963) and medicine as magnetic resonance imaging (MRI) (Lauterbur 1973). NMR well logging produces estimates of pore size distribution, total porosity, permeability and water content (Coates et al. 1999). It has been used as an alternative of conventional well logging techniques, such as neutron, bulk-density and acoustic travel-time porosity logging, as it produces estimates of several parameters with one measurement and is not influenced by matrix material. Australian innovative technology company NMR Services Australia (NMRSA) Pty Ltd has developed a BMR (Borehole Magnetic Resonance) tool that is slimmer and lighter than most of the earlier NMR drillhole logging tools (A presentation given by Ryan Gee at 12.11.2018 in University of Helsinki). This makes it suitable also for hard, crystalline bedrock where boreholes are often narrow. The earlier NMR tools were developed for larger holes, and the drillhole NMR method has previously been mostly applied in sedimentary environments (Qteq 2018). Case studies on NMR well logging in crystalline bedrock are lacking. One of the main aims of this study is to test and gain experience of BMR in the crystalline bedrock. If the BMR method proves to be successful, it could be used to refine and certify the results of or even replace some hydrogeological measurements.

Posiva Oy is an expert organization responsible of the spent nuclear fuel disposal in Finland. They carry out several groundwater measurements in drillholes to study the properties of groundwater to ensure the bedrock suitability for the disposal facility on the island of Olkiluoto in western Finland (e.g. Löfman 1999, Hirvonen and Hatanpää 2006, Posiva's website, visited on 16.6.2020). The island of Olkiluoto has suitable geological environment for final disposal (McEwen and Äikäs 2000); the bedrock is reasonably intact (groundwater flows almost entirely in fractures at the disposal depth, 400.0–450.0 m), seismic activity and hydraulic gradients are low, and no mineral deposits exist in the

area. In 2019, Posiva wanted to test the BMR method in their drillholes, because BMR could speed up the measurements and cut the costs if it is able to replace several individual drillhole measurements. Due to extensive geological, hydrogeological and geophysical studies conducted on the Olkiluoto island, the disposal site provides plenty of reference material to study the suitability of the BMR method.

1.2. History of the method and previous studies

NMR was developed for well logging purposes through the second half of the 20th century. The first NMR tools were developed already in the 1960s by Brown and Gamson (1960), but the first commercial NMR tool was made by Schlumberger in the 1970s (Herrick et al. 1979). The early NMR tools took advantage of the Earth's magnetic field, which is rather weak, and therefore the tools were limited in capability. The first modern NMR drillhole logging tools, equipped with a permanent magnet, were introduced in the 1990s by NUMAR Corp. (a subsidiary of Halliburton Co.) and Schlumberger Ltd (Coates et al. 1991, Morriss et al. 1993). Generally, these tools have a magnet generating magnetic field around the tool and this stray field is used to probe the formation outside the drillhole (Sucre et al. 2011, Walsh et al. 2013).

During the past years, drillhole NMR has been developed mostly for the usage of oil and gas industries because it is able to detect water and hydrocarbon content and estimate porosity and permeability of the reservoir (e.g. Kleinberg et al. 1994). These tools are developed specifically for the typical environment of oil and gas reservoirs (elevated temperature and pressure) and for probes large in diameter. Recently, new NMR tools, which are suitable for small drillholes and designed for hydrogeological and mining purposes, have been developed (e.g. Dlubac et al. 2013, Knight et al. 2012). NMR tools have been used to estimate several hydraulic parameters including water content, hydraulic conductivity and pore-size distribution (e.g. Johnson et al. 2012, Dlubac et al. 2013). The hydraulic parameters measured from drillhole NMR logs have been found to compare favorably to geologic, drilling, natural gamma radiation, electromagnetic induction wellbore flow and neutron probe logging and to slug tests (Walsh et al. 2013, Dlubac et al. 2013, Johnson et al. 2012). One of the new drillhole NMR tools is Borehole Magnetic Resonance (BMR) developed by NMRSA Pty Ltd (NMRSA's website, visited on

5.11.2020). This year NMRSA Pty Ltd separated from Qteq Pty Ltd. This is why some references for NMRSA`s BMR tool refer back to Qteq. By far, only one article has been published about NMRSA's BMR (Krejci et al. 2018), studying hydrogeological characterization in sedimentary environment and comparing the BMR data to pumping tests and drill cores.

1.3. Objectives of the present study

As such, NMR logging equipment has been used mostly in soft rock environments and applications in hard, heterogenous, crystalline bedrock are still lacking. This calls for test measurements and comparison with earlier data acquired by other measurement techniques in the hard rock environments.

This study aims to test the BMR method in a hard rock environment, and to determine hydrogeological parameters in the spent nuclear fuel disposal site, the Olkiluoto island. Essentially, the objective is to calibrate the BMR data processing workflow and the estimated hydrogeological parameters, currently optimized for data from sedimentary environments, to suit into crystalline bedrock.

Section 2 describes background of the Olkiluoto island site investigations and geological setting of the area. Especially hydrogeological conditions have been an essential part of the site investigations to ensure long-term safety of the spent nuclear fuel repository. Section 3 goes through fundamentals of NMR physics behind the NMR measurements and describes the estimated petrophysical parameters. The BMR measurements were performed in three drillholes, two short drillholes in the ONKALO spent nuclear fuel disposal facility and in one long surface drillhole. The data acquisition procedure is presented in Section 4. Section 4 also contains a summary of Posiva's earlier drillhole studies. The BMR data was processed in WellCAD software with additional NMR module, enabling testing multiple processing parameters and calibration of the estimated parameters to suit crystalline bedrock (explained in Section 5). Calibration was assisted with comparison to reference data from Posiva's earlier hydrogeological drillhole measurements. Functionality, accuracy and reliability of the BMR method was considered by

comparing the results to Posiva's drillhole measurements (e.g. seismic velocities, drillhole imaging, core logging) in WellCAD and statistically. Section 6 discusses the results and Section 7 summarizes the conclusions.

The BMR method gave promising results. This work presents a data processing workflow that can be modified and applied for other crystalline bedrock environments. Pore size distribution and total porosity could be derived with reasonable accuracy, but water content and permeability models need more precise calibration than possible with the reference data available for this work.

2. GEOLOGICAL BACKGROUND

2.1. Background of the site investigations

According to e.g. Aaltonen et al. (2016) and Posiva's website (visited on 5.6.2020), extensive site investigations have been conducted in Finland since 1987 by Posiva Oy and its predecessor YJT (Nuclear Waste Commission of Finnish Power Companies) to locate a suitable repository site for spent nuclear fuel. The Finnish Parliament ratified Posiva's application to build the repository to Olkiluoto island, in the municipality of Eurajoki in 2001. Three main reasons for choosing the Olkiluoto island as the repository site were (McEwen and Äikäs 2000): 1. Suitable, reasonably intact bedrock, 2. Spent nuclear fuel of the Olkiluoto nuclear power plant is temporarily preserved in the Olkiluoto island, close to the potential final disposal site, 3. Since the Olkiluoto nuclear power plant has been operating in the area since 1970's, the public acceptance for the final disposal repository was also good.

To assess the long-term safety of the repository, geological and hydrogeological properties of the Olkiluoto island bedrock have to be well understood; Posiva has conducted comprehensive geological, hydrogeological, geophysical and geotechnical studies at surface and underground, in the ONKALO research tunnel, later decided to be also used as the final disposal repository. According to e.g. Aaltonen et al. (2016), the surface studies include about 60 drillholes which have been carefully studied with geophysical and hydrogeological methods and geological logging has been performed to the core. Pilot holes

are drilled inside ONKALO before excavating new tunnels to ensure the suitability of the bedrock for tunneling. Also, some short drillholes are drilled in ONKALO in places where the bedrock geology has to be studied in more detail.

According to e.g. Posiva Oy (2013), the spent nuclear fuel is disposed in the depth of 400.0–450.0 m according to the KBS-3 (an abbreviation of *kärnbränslesäkerhet*, nuclear fuel safety) concept, based on multiple-barrier principle. The barriers include copper-iron canister, bentonite buffer, tunnel backfill and bedrock. The barriers will isolate the radioactive substance until the radiation has decreased to a safe level. Bedrock as the final barrier has to be intact and dry; if the radionuclides manage to escape from the other barriers, they are carried to the surface by groundwater flowing in fractures of the bedrock. With long exposure, groundwater may cause corrosion on the copper-iron canisters, which is also a threat for radionuclide release. Due to these scenarios, brittle deformation structures and groundwater properties have been important research objectives in the Olkiluoto island.

2.2. Paleoproterozoic tectonic evolution of Southern Finland

Olkiluoto island is located in southwestern Finland, in Southern Finland Subprovince of Svecofennian Province (Figure 1). The area has gone through variable geological history including multiple collisions and orogens, which have formed the current geology of the island.

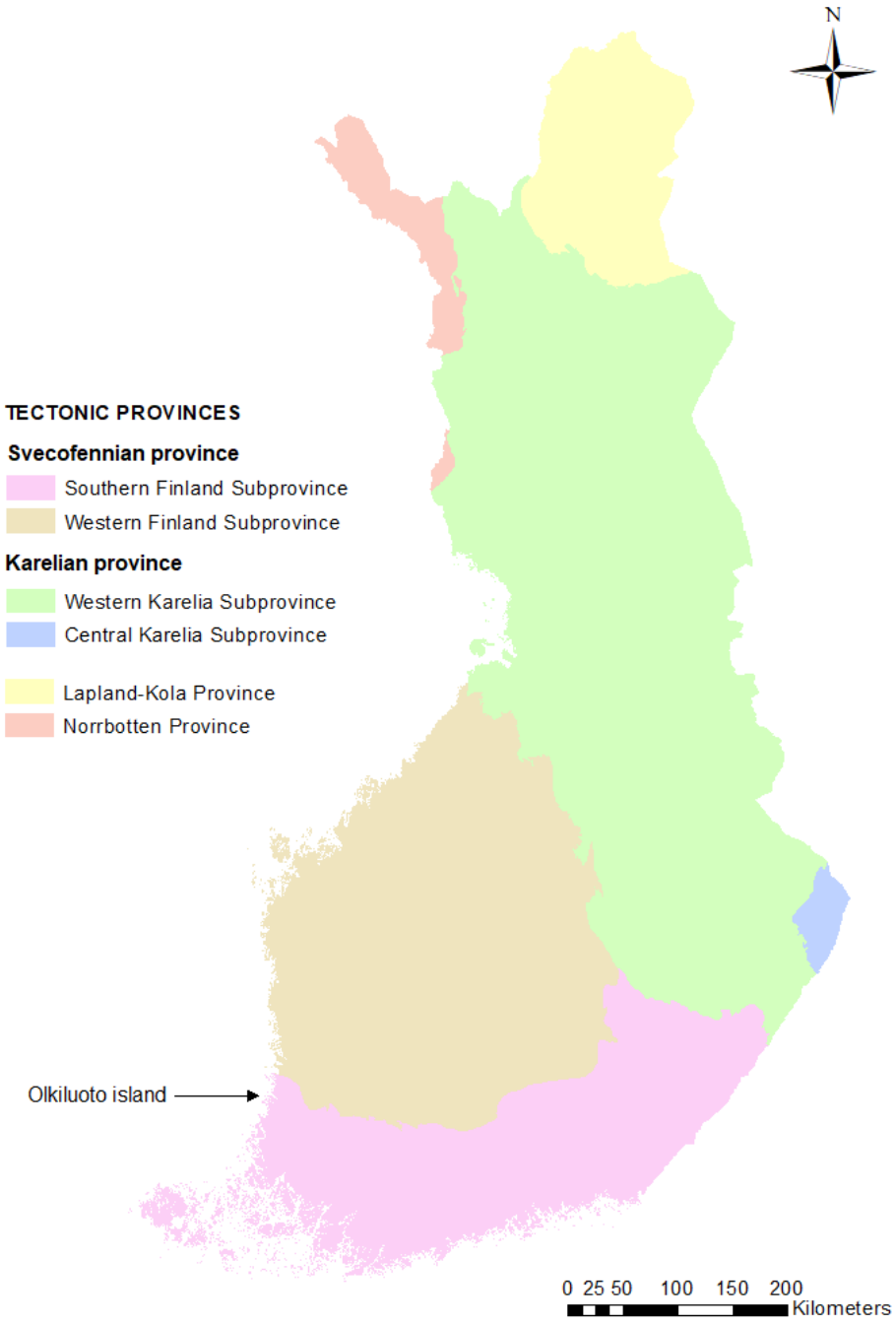

Figure 1: Tectonic provinces of Finland and location of Olkiluoto island. Base map: Bedrock of Finland 2016, 1:1 000 000, tectonic provinces, © Geological Survey of Finland.

The Precambrian bedrock of Finland has been divided into four tectonic provinces (Figure 1) and the Olkiluoto island is a part of the Svecofennian Province. According to e.g. Nironen et al. (1997) and Lahtinen (1994), the Svecofennian Province was formed between 1.93 Ga and 1.8 Ga either during one long Svecofennian orogeny or through small, separate accretions of several microcontinents. The Svecofennian Province is divided into two

subprovinces, and one of them is the Southern Finland Subprovince in which the southern Satakunta area, including Olkiluoto, belongs. Bedrock of the Southern Finland Subprovince was formed mainly at 1.89–1.87 Ga when island arcs and terranes accreted onto Archean bedrock (Nironen 1997, Lahtinen et al. 2005). At 1.91–1.86 Ga, the Western Finland Subprovince collided with the Karelia Province, and the Southern Finland Subprovince collided with the Western Finland Subprovince and the Karelian Province. This is seen as thickening of the crust and extensive formation of synorogenic granitoids and earliest deformation structures, which are dated to 1.89–1.87 Ga (Selonen and Ehlers 1998, Nironen 1999, Väisänen 1999). Lahtinen et al. (2005) refer to this stage as the Fennian orogeny.

According to Lahtinen et al. (2005), in the Svecobaltic orogeny, Sarmatian plate collided with the Fennoscandian shield at 1.84–1.80 Ga. The Southern Finland Subprovince received a thermal pulse (650.0–825.0 °C) and the rocks went through high-grade metamorphism (mostly amphibolite-facies conditions) while the crust shortened and thickened (e.g. Lahtinen et al. 2005, Korsman et al. 1984, Korsman et al. 1999, Aaltonen et al. 2016).

2.3. Geology of the Olkiluoto island

Lithological map of the Olkiluoto area has been shown in Figure 2. According to Aaltonen et al. (2016), the bedrock of the Olkiluoto consists of high-grade supracrustal metamorphic rocks, which include migmatised metapelites, meta-arenites and pyroclastic metavolcanites. These migmatites have paleosome material, which is composed of e.g. mica gneisses, mafic gneisses, quarzitic gneisses and tonalitic-granodioritic-granitic (TGG) gneisses. Palaeoproterozoic felsic, granitic-tonalitic plutonic rocks, granitic pegmatoids and diabase dykes are intruded into the supracrustal rocks. The rocks have gone through metamorphosis in variable metamorphic conditions; temperature has varied from 660 to 700 °C and pressure from 3.7 to 4.2 kbar (Tuisku and Kärki 2010). Apart from the diabase dykes, the mineral assemblages of the rock types belong to the upper amphibolite facies.

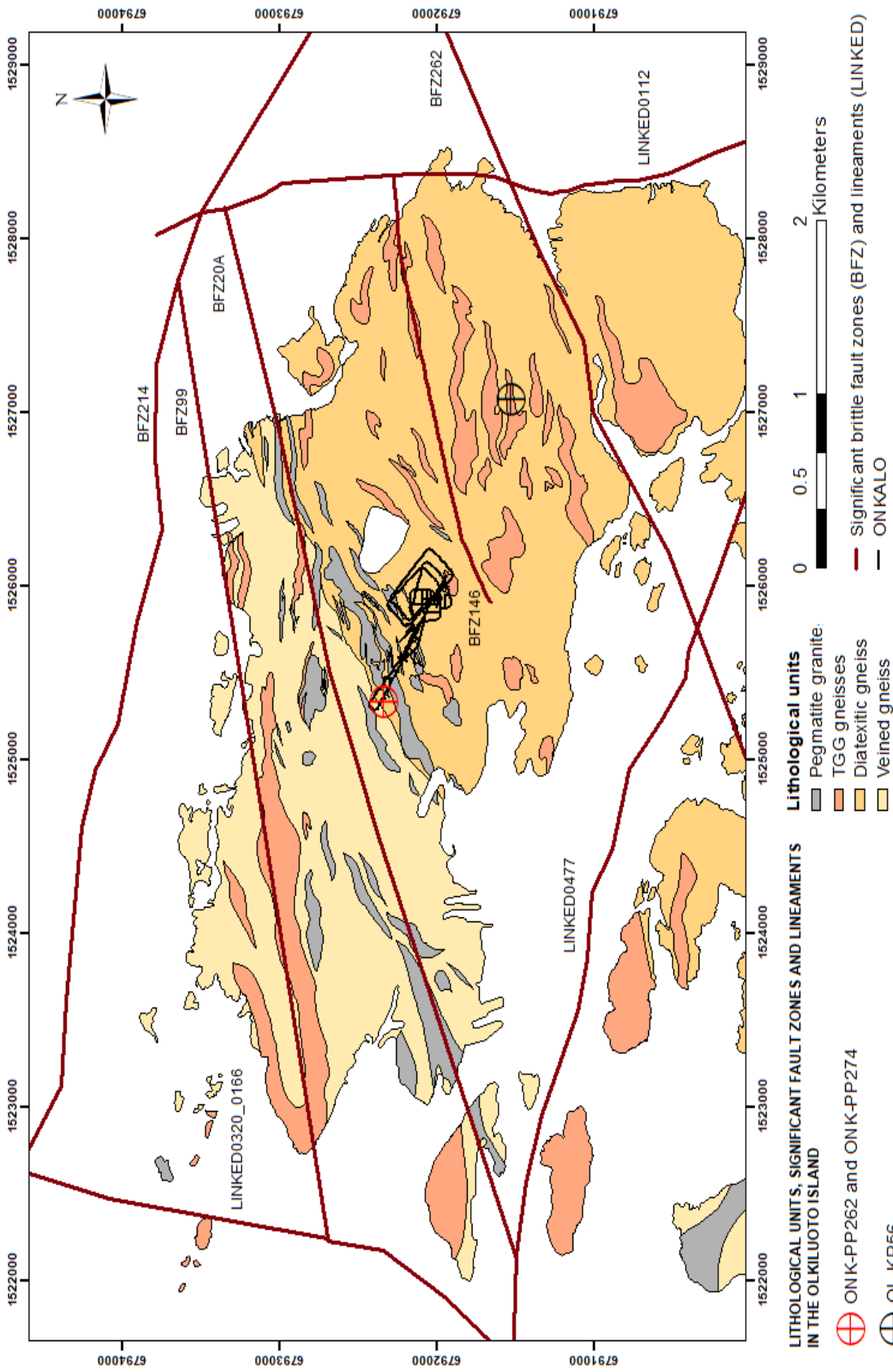

Figure 2: Lithological units, significant brittle fault zones and lineaments in the Olkiluoto island, location of the drillholes ONK-PP262, ONK-PP274 and OL-KR56 and ONKALO access tunnel. The name "LINKED" refers to the formation process of the structure by linking together different types of lineaments, e.g. topographic and geophysical (Hellä et al. 2009).

The Olkiluoto island is cut by three fracture sets (e.g. Fox et al. 2012). The first is a subhorizontal set, which comprises most of the observed fractures in Olkiluoto. It strikes north-northeast, dips to the east-southeast, and is lying subparallel to the mean bedrock foliation direction. The second is a subvertical set which strikes north-south. The third is a subvertical set which strikes roughly east-west.

According to Aaltonen et al. (2016), the detected faults in the Olkiluoto island are divided into three groups. The division is based on their geometrical properties. The first group consists faults dipping southeast with low dip angle. The second group has east-west striking faults, which dip gently to moderately from south-southeast to south-southwest. The third group consists subvertical to vertical faults striking from north to south or north-northwest to south-southwest. Significant faults are shown in Figure 2.

2.4. Hydrogeology of the Olkiluoto island

The island of Olkiluoto forms an individual hydrogeological unit. According to Koskinen et al. (2012), the annual rainfall is c. 530.0 mm and all the surface waters flow directly to the sea. The overall groundwater flow pattern is controlled mostly by topography variations, which are gently undulating (average elevation 5.0 m and highest point 18.0 m from the sea level). Flow direction below the island is mostly downwards, and on the shoreline and below the sea the flow directs mostly horizontally and/or upwards (e.g. Löfman 1999).

Besides the topography, hydraulically conductive fracture zones have an effect on the groundwater flow pattern. According to e.g. Vaittinen et al. (2020), hydrogeological zones (HZs) are utilized to describe the hydrogeological structure of the island; they are hydraulically significant site-scale zones. HZs have elevated transmissivity, containing interconnecting fractures in which groundwater prefers to flow and are often connected to brittle fault zones (BFZs). Less flow occurs in fractures in rock masses between the HZs. Smaller hydrogeological structures are described with local repository-scale hydrogeological zones (HZLs), which are outside site-scale zones.

According to Vaittinen et al. (2020), the most significant hydrogeological structure intersecting the drillhole OL-KR56 (location shown in Figure 2) used in the BMR measurements is the HZ146, which has been connected to brittle fault zone 146 (BFZ146). It cuts OL-KR56 at 339.6–385.8 m (Figure 3). Another highly visible structure is HZL11, which intersects at 122.7–124.7 m. It may be connected to BFZ327, but this is uncertain (discussed more in Section 4.2.1). HZ20B and HZ21 have also been predicted to intersect OL-KR56 at depths of 820.0 m and at 1155.0 m.

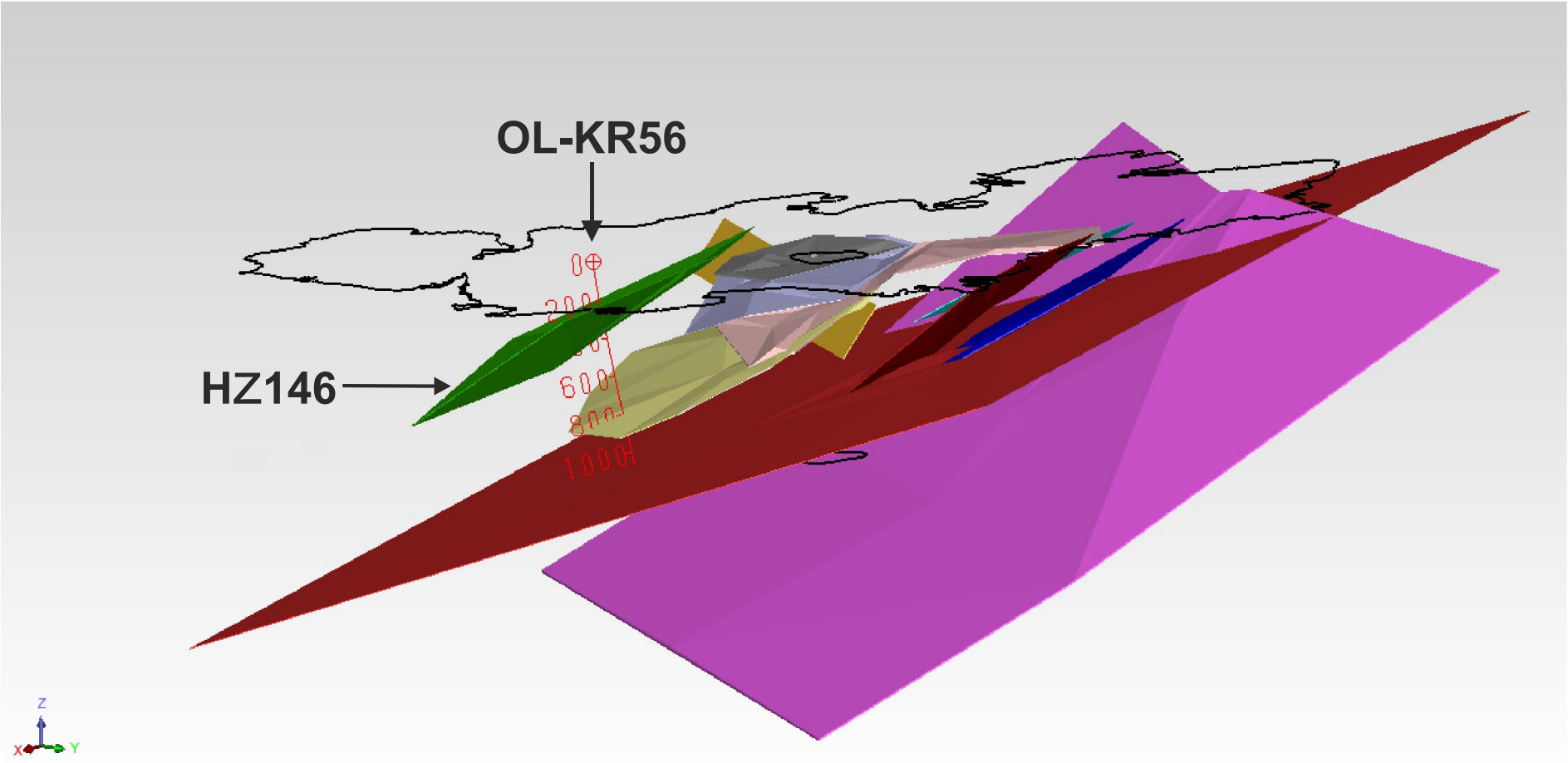

Figure 3: 3D visualization of the basic hydrogeological structure model consisting of 14 HZs on top of Olkiluoto island borders, view towards southwest. Colors represent different HZs for better distinctiveness. According to Vaittinen et al. (2020), OL-KR56 is cut by HZ146 around 339.6–385.8 m.

3. THEORETICAL BACKGROUND

A few basic physical concepts have to be understood to interpret nuclear magnetic resonance (NMR) logging data. This section goes though nuclear magnetic resonance physics, steps in NMR measurement sequence, NMR data processing and reviews the estimated petrophysical parameters.

3.1. Nuclear magnetic resonance physics

If nucleus that has a magnetic moment in an external magnetic field is perturbed by an oscillating magnetic field, it responds by producing a measurable electromagnetic signal which has a frequency characteristic of the magnetic field of the nucleus. The oscillating frequency of the magnetic field matches with the intrinsic frequency of the nucleus. This phenomenon is called nuclear magnetic resonance.

3.1.1. Atomic nuclei in NMR

All nuclei, neutrons and protons, have a spin, an intrinsic angular momentum. If the nucleus is electrically charged, it has a magnetic momentum; the spinning charged particle constitutes a little current loop, which produces a magnetic field (Chabay and Sherwood 2011). The overall spin of an atomic nucleus depends on the number of neutrons and protons. If the number is even, the overall spin is zero. This is why NMR measurements can be made only on nuclei that have an odd number of protons and neutrons. Hydrogen (^{1}H) has only one proton, one electron and no neutrons, which produces a relatively large magnetic moment and a strong signal. Hydrogen is present in both water and hydrocarbons, and so far hydrogen nuclei responses have been utilized in almost all NMR logging studies (Coates et al. 1999).

3.1.2. Static magnetic field, polarization and precession

In the beginning of an NMR measurement sequence (discussed in the following section), a strong static magnetic field is utilized to align the nuclei. When the static field is applied,

it exerts a torque on the nuclei and aligns the spin axes with the field. Thus, the nuclei are polarized. The axes of the nuclei move perpendicular to the torque in a motion called precession (Figure 4). According to e.g. Bloch (1946) and Cowan (1997), when the static field is applied to the nuclei, they will precess around the direction of the field. The precessional frequency (f) is called Larmor frequency and is given by

$$f = \frac{\gamma B_0}{2\pi} \tag{3.1}$$

where B_0 is the magnetic field strength and γ is the gyromagnetic ratio, a measure of strength of the nuclear magnetism for a specific nucleus (Coates et al. 1999). According to Cowan (1997), for hydrogen,

$$\frac{\gamma}{2\pi} = 42.58 \ \frac{MHz}{T} \tag{3.2}$$

Larmor frequency (Equation 3.1) is proportional to the strength of the static magnetic field and the gyromagnetic ratio of the nucleus. If we are measuring only hydrogen nuclei, the gyromagnetic ratio has a fixed value and thus, according to Equation 3.1, the Larmor frequency is only a function of the static magnetic field.

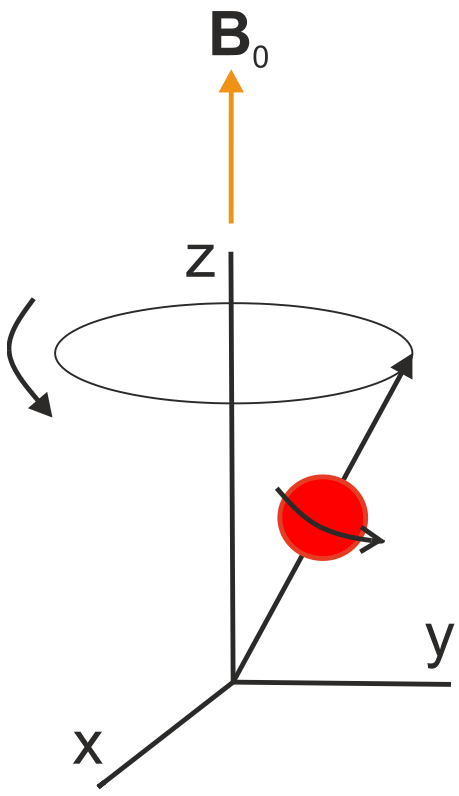

Figure 4: Precessing nuclei in an external magnetic field $\mathbf{B_0}$.

According to e.g. Bloch (1946), when an external magnetic field is applied on a proton, its nuclear spin angular momentum vector may exist in one of two quantum energy states.

The energy state depends on the orientation of the precessional axis with respect to the direction of the external magnetic field. Preferred state is the low-energy state, where the precessional axis is parallel to the magnetic field direction. If the precessional axis is anti-parallel to the magnetic field direction, the proton is in the high-energy state (Figure 5).

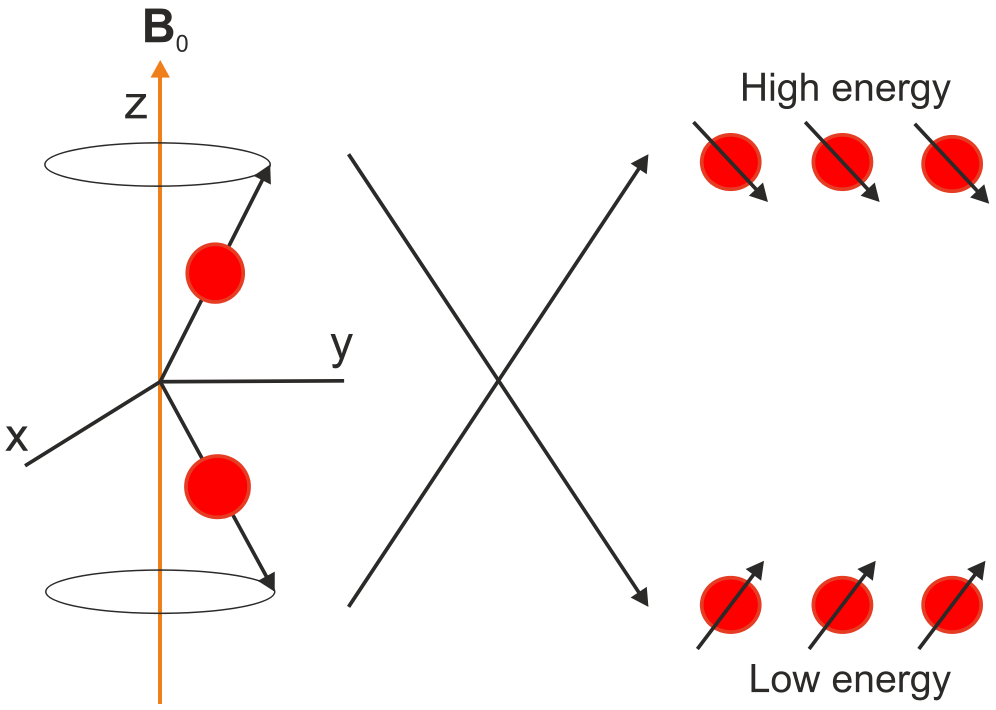

Figure 5: Energy state of the nucleus is determined by the alignment of the precessional axis and the direction of the applied external magnetic field $\mathbf{B_0}$.

When the static magnetic field is applied to a number of protons, more proton spins are precessing parallel to the magnetic field than anti-parallel. Bulk magnetization M_0, which forms the signal measured by NMR devices, is the difference between the number of protons precessing parallel to the magnetic field to the number of protons precessing anti-parallel (e.g. Coates et al. 1999). M_0 is defined as the net magnetic moment per unit volume. According to e.g. Cowan (1997), if N number of nuclei per unit volume is assumed, M_0 is given by Curie's Law as

$$M_0 = \mathrm{N}\frac{\gamma^2 h^2 I(I+1)}{3(4\pi^2)kT}\mathbf{B_0} \qquad (3.3)$$

where k is the Boltzmann's constant ($1.380649 \cdot 10^{-23}\ \frac{\mathrm{J}}{\mathrm{K}}$), T is absolute temperature (in Kelvins), h is the Planck's constant ($6.62607015 \cdot 10^{-34}$ J·s) and I is the spin quantum number of the nucleus.

3.1.3. Oscillating magnetic field

In an NMR measurement sequence, an oscillating magnetic field is applied to tip the precessing nuclei and to generate so called spin echo series, which is the raw data recorded by the NMR tool. Frequency of the oscillating magnetic field is the Larmor frequency and thus, it is in resonance with the nuclei. The oscillating field is turned on and off in a sequence. When the field is turned off, the protons begin to de-phase and thus, the precessions of the protons are not in-phase. This leads to decrease in net magnetization. According to Cowan (1997) and Fukushima and Roeder (1981), the magnetization is tipped through an angle which can be expressed as

$$\theta = \gamma B_1 T \tag{3.4}$$

where is θ is the tip angle, B_1 is the amplitude of the oscillating field and T is the time over which the oscillating field is applied.

3.1.4. Spin echo series

NMR generates a series of spin echoes by re-phasing the de-phased protons caused by the inhomogeneities in the magnetic field. Spin echo is the re-phasing of the precessing nuclei with a pulse of the oscillating magnetic field, resulting as a change in amplitude as a function of time. A receiver coil measuring magnetization in transverse direction detects a decaying signal when the protons de-phase. The decay is called free induction decay (FID) (e.g. Carr and Purcell 1954, Cowan 1997). Inhomogeneities in the magnetic field cause FID. The inhomogeneities are due to the magnetic field gradient and to molecular processes occurring in the measured material. The magnetic field has inhomogeneities which make the protons at different locations to precess with different Larmor frequencies producing the decay. However, this effect is reversible. The magnetization vectors of the protons in the transverse planes can be re-phased with a new pulse of the oscillating magnetic field. This aligns the faster and slower precessing nucleus generating a spin-echo (Cowan 1997).

Inhomogeneities in the static magnetic field cause de-phasing of the nucleus, which is reversible with oscillating magnetic field pulses. However, also molecular interactions

and diffusion result as de-phasing, which is irreversible. Once the de-phasing has begun, protons can no longer be re-phased and the spin-echo series will decay.

3.2. Performing an NMR measurement

NMR measurement consists of two parts; in the first one, a static magnetic field is applied to align the nuclei. In the second one, an oscillating magnetic field is used to tip the nuclei. NMR usually applies 180° pulses of the oscillating magnetic field repeatedly to generate a series of spin echoes, which is shown in Figure 6. This series of spin echoes can be recorded. The whole pulse series is called a CPMG sequence (named after its inventors: Carr, Purcell, Meiboom and Gill) (Carr and Purcell 1954, Meiboom and Gill 1958).

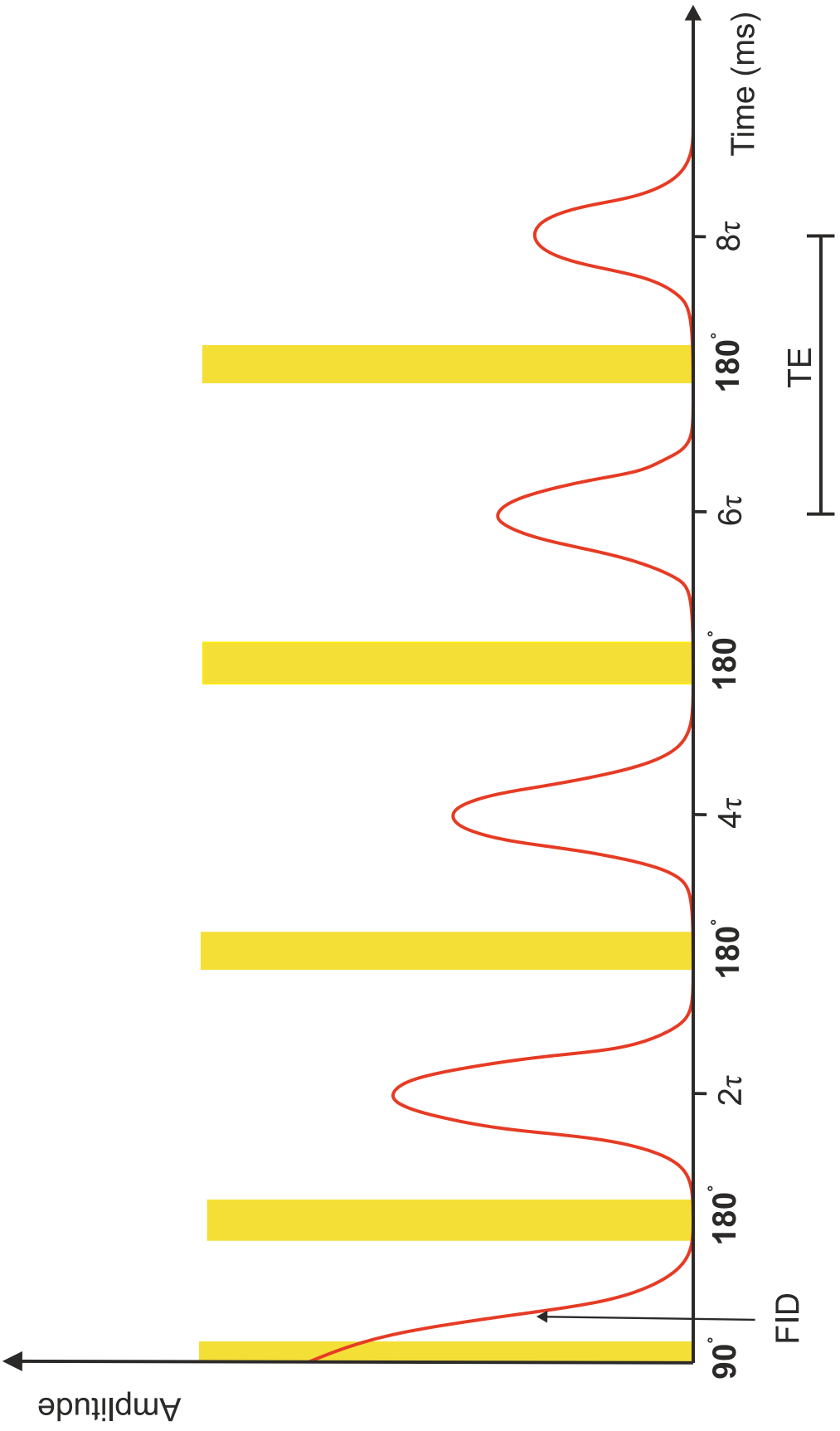

Figure 6: CPMG pulse sequence is used to generate the spin echoes. The CPMG pulse sequence consists of 90° pulse followed by a series of 180° pulses. The spin echoes follow the pulses with decreasing amplitude. TE is the inter-echo spacing, time between the echo peaks. FID is Free Induction Decay.

3.2.1. Part A: Polarization with static magnetic field

The measurement sequence begins with polarizing the hydrogen nuclei with a static magnetic field $\mathbf{B}_0$ as described in 3.1.2. $\mathbf{B}_0$ is kept on during the whole measurement sequence. The nuclei start to precess with Larmor frequency in the direction of $\mathbf{B}_0$. The nuclei are polarized after they have aligned in the static magnetic field. According to Fukushima and Roeder (1981) and Bloch (1946), polarization does not occur immediately; it grows with time and is affected by a time constant called longitudinal relaxation time, T_1:

$$M_z(t) = \boldsymbol{M_0}(1 - e^{\frac{-t}{T_1}}) \tag{3.5}$$

where t is nuclei exposure time to the static magnetic field, $M_z(t)$ is the magnitude of magnetization at time t when the direction of the magnetic field is aligned along the z axis and $\boldsymbol{M_0}$ is the maximum magnetization in a given magnetic field.

The time at which magnetization has reached 63 % of its final value is T_1 (Bloch 1946, Coates et al. 1999).

3.2.2. Part B: Applying an oscillating magnetic field

After the polarization has been reached, the nuclei are tipped with an oscillating magnetic field $\mathbf{B}_1$ as described in 3.1.3. The tipping begins with a 90° pulse of $\mathbf{B}_1$ (Figure 6), with which the axis of the precessing nuclei are moved by 90° to a transverse plane. Then, the $\mathbf{B}_1$ field is turned off, nuclei begin to de-phase and FID is formed (Figure 6). After complete de-phasing, 180° pulse of $\mathbf{B}_1$ is applied to re-phase the nuclei. Thus, a complete spin-echo is formed. Inter-echo spacing (TE) is the time between the echo peaks, which can be also defined as 2τ (Figure 6). TE is the same time that transpires between the 180° pulses of $\mathbf{B}_1$ and τ it the time that transpires from the 90° pulse of $\mathbf{B}_1$ to the first 180° pulse.

NMR applies a series of 180° pulses of the $\mathbf{B}_1$ field to form a complete spin-echo series, the CPMG sequence. Between these pulses, irreversible de-phasing occurs (mechanisms and reasons for irreversible de-phasing are explained in Section 3.3.) and the following spin-echo does not reach as high amplitude as the previous one. NMR logging tool measures the amplitude of the spin echoes in the CPMG sequence to monitor the transverse magnetization decay and the irreversible de-phasing. The transverse relaxation time is referred as to T_2, a time constant of the transverse magnetization decay. According to e.g. Cowan (1997), amplitude of the transverse magnetization $M_x(t)$ is the amplitude of the CPMG series at time t, which is given by

$$M_x(t) = M_{0x} e^{\frac{-t}{T_2}} \tag{3.6}$$

where M_{0x} is the magnitude of transverse magnetization at $t = 0$.

3.3. NMR relaxation mechanisms of fluids in rock pores

Understanding the NMR relaxation mechanisms in rock pores is critical for assessing the petrophysical properties. The relaxation mechanism include longitudinal (T_1) and transverse (T_2) relaxation, which are affected by bulk, surface and diffusion-induced relaxations. T_1 describes the time it takes from the nuclei to reach polarization and T_2 the time from the nuclei to de-phase.

Longitudinal relaxation (T_1) occurs when the static magnetic field polarizes the nuclei. The preferred energy state for the nuclei is the low-energy state, in which the nuclei are aligned along the static magnetic field. The precessing nuclei moving to low-energy state are releasing energy to the surroundings. Transverse relaxation (T_2) occurs when the polarized nuclei start to de-phase, but no energy change to surroundings is involved. Therefore, transverse relaxation is always faster than longitudinal relaxation but also less than or equal to longitudinal relaxation (Cowan 1997).

Generally, when the measured substance is a solid, the nuclei achieve much smaller T_2 than T_1 (Guimaraes 1998). When the substance is a reservoir fluid and in a homogeneous magnetic field, T_2 is approximately equal toT_1. If the fluid is in a gradient magnetic field

and a CPMG measurements set is used, T_2 is smaller than T_1. The difference is controlled mostly by the gradient of the field, inter-echo spacing and fluid diffusivity (Bendel 1990). When a fluid fills a porous medium (e.g. rock) both T_2 and T_1 are remarkably decreased. The relaxation mechanisms of the nuclei are different for solid and fluid.

Three independent relaxation mechanisms are present for fluids in porous rocks: bulk fluid processes (affecting both T_1 and T_2), surface relaxation (affecting both T_1 and T_2) and diffusion in the presence of magnetic field gradients (affects only T_2 relaxation). According to e.g. Kenyon (1992), all three processes act in parallel. T_1 and T_2 times of pore fluids are given as:

$$\frac{1}{T_2} = \frac{1}{T_{2bulk}} + \frac{1}{T_{2surface}} + \frac{1}{T_{2diffusion}} \tag{3.7}$$

$$\frac{1}{T_1} = \frac{1}{T_{1bulk}} + \frac{1}{T_{1surface}} \tag{3.8}$$

where T_2 is the transverse relaxation time of the pore fluid measured by the CPMG sequence, T_{2bulk} is the T_2 relaxation time of the pore fluid as it would be measured in a container so large it would neglect effects of the container, $T_{2surface}$ is the T_2 relaxation time of the pore fluid resulting from surface relaxation, $T_{2diffusion}$ is the T_2 relaxation time of the pore fluid as induced by diffusion in the magnetic field gradient, T_1 is the longitudinal relaxation time of the pore fluid, T_{1bulk} is the T_1 relaxation time of the pore fluid as it would be measured in a container so large it would neglect effects of the container, and $T_{1surface}$ is the T_1 relaxation time of the pore fluid resulting from surface relaxation.

The type of fluid (oil, gas or water) filling the rock pores, pore size, wettability of the rock and strength of surface relaxation affect the relative importance of the relaxation mechanism.

3.3.1. Bulk relaxation

Bulk relaxation is determined by the physical properties of the fluid, e.g. viscosity, density and chemical composition. It can be measured when surface relaxation has been eliminated by placing the fluid into a large container. Then, the fluid is subjected to a homogeneous magnetic field and a CPMG sequence. Environmental conditions, such as temperature and pressure, affect the bulk relaxation as well. According to e.g. Vinegar (1995), bulk relaxation times for water are given as:

$$T_{1bulk} \cong 3\left(\frac{T_K}{298\eta}\right) \tag{3.9}$$

$$T_{2bulk} \cong T_{1bulk} \tag{3.10}$$

where T_K is temperature (Kelvins) and η is fluid viscosity (cP).

3.3.2. Surface relaxation

Surface relaxation occurs at the pore-grain boundary of the rock. According to Kenyon (1992), Brownstein and Tarr (1979) and Kleinberg et al. (1994) the dominant term in T_1 and T_2 relaxation times, which is also known as the diffusion limit, is given as

$$\frac{1}{T_{2surface}} = \rho_2\left(\frac{S}{V}\right)_{pore} \tag{3.11}$$

$$\frac{1}{T_{1surface}} = \rho_1\left(\frac{S}{V}\right)_{pore} \tag{3.12}$$

where ρ_2 is T_2 surface relaxivity, ρ_1 is T_1 surface relaxivity and $\left(\frac{S}{V}\right)_{pore}$ is ratio of the surface area of the pores (S) to the volume of the fluid (V).

According to Equations (3.11) and (3.12), surface relaxation is controlled by the ratio of pore surface area to fluid volume and surface relaxivity. The higher is the surface area S, the more likely it is that the fluid molecules interact with the pore walls (NMRSA 2018). The surface-to-volume ratio $\left(\frac{S}{V}\right)_{pore}$ is also directly correlated to the pore size of the rock. Surface relaxivity is characterized by the abundance of paramagnetic atoms at or near the pore surfaces. This results as variation of surface relaxation with mineralogy (Chang et al. 1994).

3.3.3. Diffusion-induced relaxation

According to e.g. Coates et al. (1999), in a gradient magnetic field and subjected to a long inter-echo spaced CPMG sequence, water goes through diffusion-induced relaxation. For water, $T_{2diffusion}$, the diffusion mechanism relaxation time constant is important for detection. The T_2 relaxation rate ($1/T_2$) increases when a significant gradient exists in the magnetic field, because molecular diffusion causes more de-phasing. The de-phasing is due to the molecule moving into a region in which strength of the magnetic field is different and thus also the precession rate is different from other molecules which have not moved during the measurement. Therefore, 180° $\mathbf{B_1}$ pulse will not re-phase these nuclei. Diffusion does not affect the T_1 relaxation rate.

According to Bendel (1990), the diffusion-induced relaxation rate is given as

$$\frac{1}{T_{2diffusion}} = \frac{D(\gamma GTE)^2}{12} \tag{3.13}$$

where D is the molecular diffusion coefficient, γ is the gyromagnetic ratio of a proton, G is the field-strength gradient (G cm^{-1}) and TE is the inter-echo spacing used in the CPMG sequence (Figure 6).

The diffusion coefficient is controlled by physical properties, such as molecular composition and viscosity. Also, environmental conditions (temperature and pressure) have an effect on the diffusion. According to Mardon et al. (1996), the molecular diffusion coefficient is given for water as

$$D_w \cong 1.2\left(\frac{T_K}{298\eta}\right) * 10^{-5} cm^2/s \tag{3.14}$$

where D_w is the molecular diffusion coefficient for water, T_K is the temperature (Kelvins) and η is viscosity.

Molecules in fluid often move only in the rock grain-fluid interface and/or by the interfacial tension of the fluids. This results as different diffusion coefficient for a fluid in a rock and a bulk fluid at the same pressure and temperature conditions (Prammer et al. 1995). For water, diffusion effects become negligible at short inter-echo spacings. The inter-

echo spacing can be selected while performing the NMR measurement to achieve the desired result.

3.4. Processing of NMR data

The recovered raw data from the NMR tool is the spin-echo train. Purpose of the data processing is to extract T_2 distribution, which we can think of as pore size distribution, from the raw data.

This is done with a mathematical inversion process, usually referred as echo-fitting. The T_2 distribution of the rocks is normally a continuous function. To simplify the function to fit into the spin echoes, the echo-fitting process uses a multi-exponential model assuming that the T_2 distribution consists of m discrete relaxation times T_{2i} with corresponding porosity components ϕ_i (Coates et al. 1999). The T_{2i} values are pre-selected, and the echo-fitting process tries to determine the porosity components for each distribution. Equation 3.15 displays a system of equations that represent single echoes (Coates et al. 1999).

$$
\begin{aligned}
echo(1) &= \phi_1 e^{-\left(\frac{t(1)}{T_{2,1}}\right)} + \phi_2 e^{-\left(\frac{t(1)}{T_{2,2}}\right)} + \phi_3 e^{-\left(\frac{t(1)}{T_{2,3}}\right)} + \cdots + \phi_m e^{-\left(\frac{t(1)}{T_{2,m}}\right)} + noise \\
echo(2) &= \phi_1 e^{-\left(\frac{t(2)}{T_{2,1}}\right)} + \phi_2 e^{-\left(\frac{t(2)}{T_{2,2}}\right)} + \phi_3 e^{-\left(\frac{t(2)}{T_{2,3}}\right)} + \cdots + \phi_m e^{-\left(\frac{t(2)}{T_{2,m}}\right)} + noise \\
echo(n) &= \phi_1 e^{-\left(\frac{t(n)}{T_{2,1}}\right)} + \phi_2 e^{-\left(\frac{t(n)}{T_{2,2}}\right)} + \phi_3 e^{-\left(\frac{t(n)}{T_{2,3}}\right)} + \cdots + \phi_m e^{-\left(\frac{t(n)}{T_{2,m}}\right)} + noise
\end{aligned}
\qquad (3.15)
$$

where $t(i) = i\,TE$ and $i = 1, \ldots n,$ is the time when the i^{th} echo was acquired.

Equation 3.15 consists of n linear functions with m unknowns, where n is much larger than m (the number of T_2 values or bins). The equation must be inverted in a way to achieve the "best" set of ϕ_i (Golub and Van Loan 1983), but the solution is complicated due to the fact that ϕ_i must be equal or greater than zero and that the fit to a sum of multi-exponentials is unstable. According to Coates et al. (1999), a regularization (a chosen smoothness of the inversion) must be involved with Equation 3.15. This means that the inverse is a function of both measured spin echoes and the regularization. The regularization is partly controlled by the signal-to-noise ratio of the data. According to Qteq

(2018), the signal-to-noise ratio of the early echoes can be improved by using burst sequences, a series of short CPMG sequences with short wait time and small number of echoes. The burst sequences can be stacked together and combined to the main CPMG sequence. The final result of the ϕ_i is not unique; distributions with different shapes can appear as good fits to the decay curve (Coates et al. 1999). Therefore, interpretation of fine details of the decay curves must be careful. However, the area under the curve (representing porosity) and the time location of high-porosity bins can be considered accurate.

3.5. NMR petrophysics

NMR relaxation mechanisms produce a wide range of petrophysical information. The basis of all petrophysical information is the processed T_2 distribution which allows calculating estimates of total porosity, water volumes and permeability.

3.5.1. Cutoff values

T_2 distribution can be divided into different zones based on the size of pores and type of bound water. Typically, in sedimentary environments it is divided into three zones. The division relies on an assumption that bound fluids are concentrated in small pores and moveable fluids in larger pores (Coates et al. 1999). The T_2 cutoff values are related to the volume of a pore; the value can be selected to separate fluids concentrated in small pores and bound to the rock from fluids concentrated in large pores and being moveable.

The first cutoff (cutoff 1), often referred as clay-bound water cutoff, divides the whole bound water volume into clay-bound water and capillary-bound water (Figure 7). In sedimentary environments, the clay-bound water cutoff values are traditionally defined to be in the range of 3 to 10 ms depending on clay mineralogy (e.g. Straley et al. 1997, Qteq 2018). However, significantly smaller values have also been suggested; Testamanti and Rezaee (2017) suggest a value of 0.25 ms for shales, Freedman et al. (1997) 1 ms and Martin and Dacy (2004) 2.8 ms for shaly sandstones.

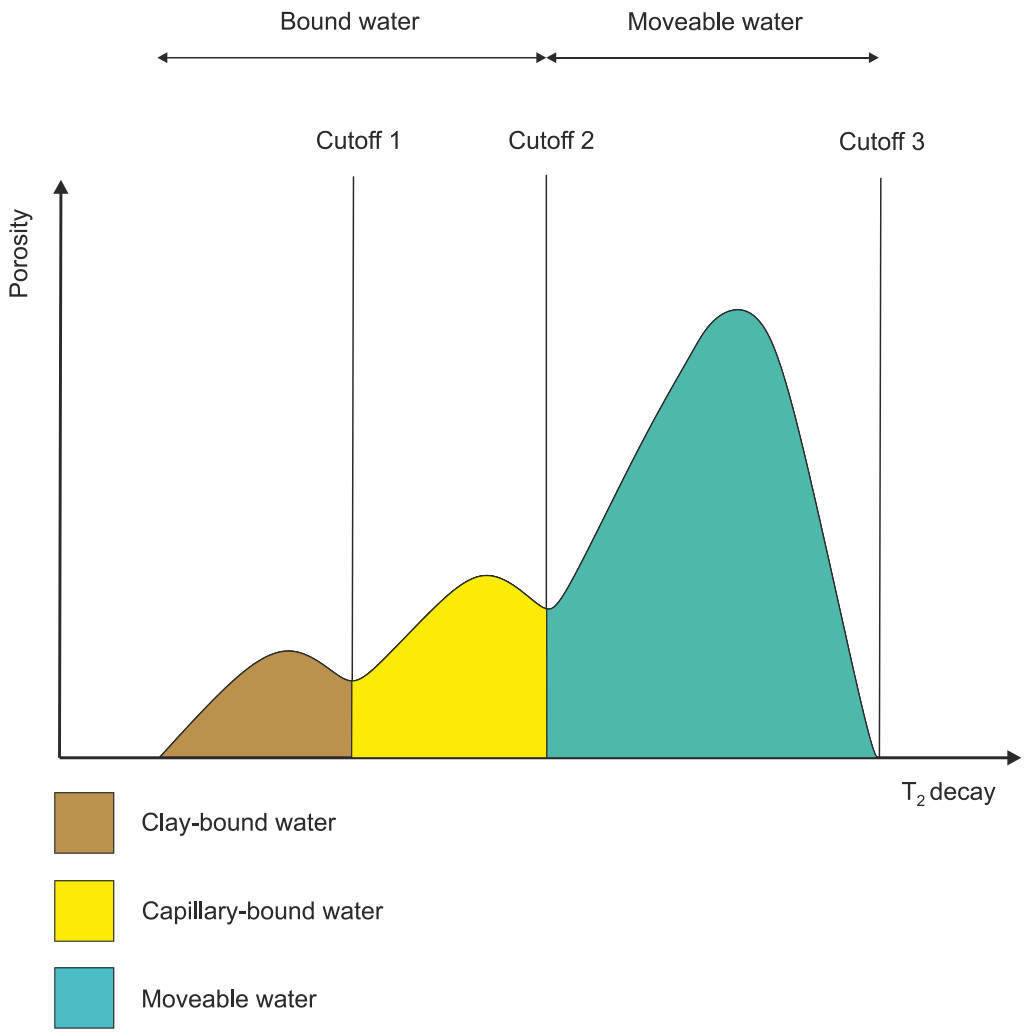

Figure 7: Bound water types by three T_2 cutoff values.

The second cutoff (cutoff 2), often referred as capillary-bound water cutoff, divides the T_2 distribution into bulk volume of irreducible water (BVI) and volume of free fluid (FFI) (see Figure 7). The cutoff value is dependent on lithology; it depends on surface relaxivity (Equations 3.11 and 3.12) which is connected to lithology. Surface relaxivity is characterized by the abundance of paramagnetic minerals (Chang et al. 1994), which results as smaller T_2 value as the amount of paramagnetic material in the formation increases. According to Coates et al. (1997), Coates et al. (1999) and Qteq (2018), commonly used values for the cutoff in sedimentary environments are 33 ms in sandstones and 100 ms in carbonates.

The third cutoff (cutoff 3), often referred as moveable water cutoff, separates the signal from baseline offsets. In sedimentary environments, it is typically set to 3 to 5 s (NMRSA

2018, Coates et al. 1999), because signal coming after several seconds is not reasonable and can be considered as noise.

According to Coates et al. (1999), the cutoff values are not affected only by lithology, but also several other factors including pore-wall chemistry, minor paramagnetic or ferromagnetic minerals, texture, pore throat to pore body ratio and other not well-understood factors. Thus, the cutoff values can vary within a single lithology.

T_2 cutoffs can be determined in laboratory with NMR measurements on core samples. The laboratory analysis is based on measuring the sample with both 100 % water saturated and irreducible conditions and then comparing received incremental porosity to cumulative porosity to find the T_2 cutoff value of the specific sample.

All the currently determined cutoff values are for sedimentary rock types, and no laboratory-calibrated values exist for hard, crystalline bedrock.

3.5.2. Pore size distribution

The fundamental output of an NMR measurement is the T_2 distribution. As discussed earlier, the T_2 value of a single pore is proportional to the surface-to-volume ratio of the pore (Equation 3.11), if the rock is fully saturated with water. Therefore, the T_2 distribution of the whole rock represents the pore-size distribution of the rock. The sum of the amplitudes of each element with specific T_2 value derives total porosity of the rock. The derived total porosity depends on the value of the cutoff 3; it cuts signal from noise, which may increase the total porosity significantly if not being cut. To determine the pore size distribution, a range of T_2 values is considered to correspond to a range of different pore sizes and additionally, water bounding type and volume of the water.

As such, the T_2 distribution can be applied to recognizing lithological units based on pore types, or to estimate grain size in granular rocks (Qteq 2018). Lithological units may show characteristic T_2 distributions, and thus also contacts between different units can be

traced. In granular rocks, bigger grains allow larger pore space between them, which may be shown in T_2 distribution as a small number of large pores.

3.5.3. Permeability models

Permeability is calculated based on a combination of experimental and theoretical relationships concerning porosity, T_2 distribution, water volumes and lithology. In petrophysical applications permeability can be considered to be proportional to the square of some geometrical size. This size is often considered to be the one of the pore throat, which is suggested by the comparison between capillary pressure curves and permeability (Pittman 1992, Thompson et al. 1987). NMR measures essentially the size of the pores, but in many sedimentary rocks, pore size and pore throat size has a significant comparison (Coates et al. 1999).

There are two commonly used permeability models, Timur-Coates (T-C) model and Schlumberger-Doll-Research (SDR) model, which are based on Kozeny-Carman relationship (Kozeny 1927, Carman 1956). The Kozeny-Carman relationship estimates permeability for a packed bed of solids if the flow through is laminar. According to Gueguen and Palcaiuckas (1994), it can be calculated from porosity and the ratio of the total surface area to the total volume of void space of the material:

$$k = a\frac{\phi}{(\frac{S_T}{V_T})^2} \tag{3.16}$$

where *a* is a dimensionless constant capturing the tortuosity and shape of the pores in the material, ϕ is porosity, S_T is the total surface area and V_T is the total volume of void space. For the use with NMR data, the Equation 3.16 was modified by including T_2 relaxation time and adjusting an exponent to the porosity.

In the Mean T_2 model, or SDR (Schlumberger-Doll-Research) model (Kenyon 1997 and Kenyon et al. 1989), T_2 relaxation time has been included by the replacing $\frac{S_T}{V_T}$ ratio with geometric mean of the T_2 distribution, which describes changes in surface-to-volume ratio. According to Kenyon et al. (1988), it gives the permeability as

$$k = aT_{2gm}^2\phi^m \tag{3.17}$$

where T_{2gm} is geometric mean of the T_2 distribution and a is a coefficient depending on the formation type.

In the Free Fluid or T-C model, the T_2 relaxation time was included by replacing the $\frac{S_T}{V_T}$ ratio with the FFI (free fluid volume) to BVI (bulk volume of irreducible water) ratio describing the changes in the surface-to-volume ratio. The ratio is dependent on the value of the cutoff 2 (see Figure 7), which determines the volumes. According to Coates et al. (1999), FFI and BVI are related as

$$FFI = \phi - BVI \tag{3.18}$$

where ϕ is the calibrated porosity of the formation.

According to Timur (1968), Coates and Denoo (1981) and Coates et al. (1999) the Free Fluid model gives the permeability as

$$k = [\left(\frac{\phi}{C}\right)^m \left(\frac{FFI}{BVI}\right)]^2 \tag{3.19}$$

where k is permeability, m is a factor accounting for the amount of porosity that contributes to the water flow and C is a variable dependent on formation processes. Permeability can be converted into hydraulic conductivity with rearrangement of Darcy's law. According to Darcy (1856), Darcy's law is gives hydraulic conductivity as

$$K = \frac{\Delta V}{\Delta t}\frac{L}{Ah} \tag{3.20}$$

where ΔV is volume of water which is measured over time Δt, over a soil specimen with length L and a cross-sectional area A having a hydraulic head h. According to e.g. De Marsily (1986), Darcy's law can be rearranged knowing that the volumetric water flow is dependent on pressure differential on the two sides of the soil sample, permeability and viscosity. The rearranged formula is given as

$$K = \frac{k\rho g}{\mu} \tag{3.21}$$

where k is permeability, ρ is density of water (997 kg m^{-3}), g is gravitational acceleration on Earth (9.81 m s^{-2}) and μ is water viscosity ($1.002 \cdot 10^{-3}$ Pa·s). Water viscosity is dependent on temperature, and it can be taken into account with Vogel-Fulcher-Tammann

equation. According to Vogel (1921), Fulcher (1925) and Tammann and Hesse (1926), it is given as

$$\mu = A^{\frac{B}{T-C}} \tag{3.22}$$

where A is $2.414 \cdot 10^{-5}$ Pa·s, B is 247.8 K, C is 140 K and T is temperature in Kelvins (personal communication with Ryan Gee on 4.11.2020).

According to e.g. Marschall et al. (1997) and Coates et al. (1999), it has been observed that the Coates model is more flexible than the SDR model; when calibrating core carefully, the Coates model has been successfully customized for different formations. SDR model suits better for zones containing only water. Coates et al. (1999) suggests that in fractured formations, permeability estimates from both models are too low, because the models only represent permeability of the matrix. This makes both models hard to fit into crystalline, fractured bedrock. It has been suggested, that the SDR model is better for crystalline bedrock, because of the dual porosity structure of the bedrock (personal communication with Ryan Gee and Benjamin Birt on 2.4.2020, Warren and Root 1963). This is taken better into account in the SDR model with the geometric mean of the T_2 distribution. However, the constants *m* and *a* have to be calibrated to fit into crystalline rocks, because no earlier measurements exists from crystalline bedrock. This can be done either by calibration of the core, for example with Special Core Analysis (Humborstad 2014), or by comparison to other methods deriving similar parameters.

4. RESEARCH MATERIAL

4.1. BMR data acquisition in the Olkiluoto island

4.1.1. NMRSA's BMR tool

Borehole Magnetic Resonance (BMR) tool (Figure 8) is an NMR drillhole tool developed by NMRSA Pty Ltd. According to Qteq (2018) and Coates et al. (1999), the BMR tool consists of two major components: a set of permanent magnets creating the static magnetic field $\mathbf{B}_0$ and an antenna creating the oscillating magnetic field $\mathbf{B}_1$ (Figure 9). The

intention of these magnetic fields is discussed in detail in Sections 3.1. and 3.2. The antenna is also associated with electronics used to detect the oscillating electromagnetic fields generated by the precessing hydrogen nuclei. Additionally, the tool contains a microprocessor to handle the large amount of data generated during every measurement.

Figure 8: NMRSA's BMR tool in its transport box with a stand-off (white tube) installed.

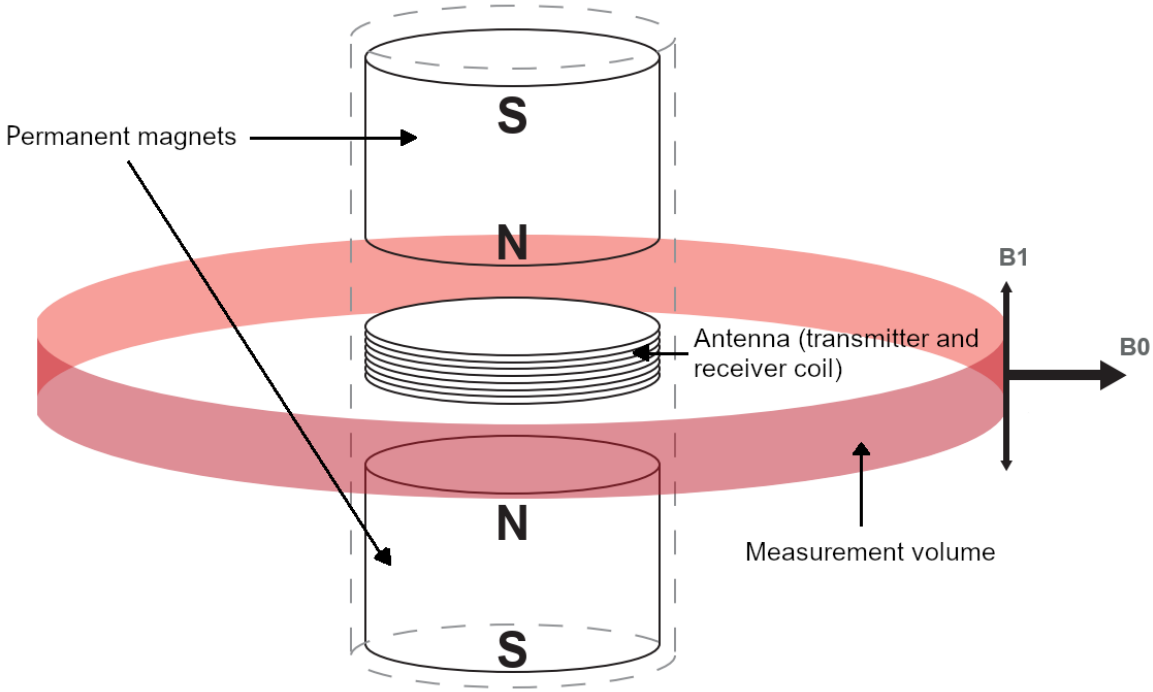

Figure 9: Schematic layout of the Borehole Magnetic Resonance (BMR) tool by NMRSA Pty Ltd. Modified from Qteq (2018).

The permanent magnets create the static $\mathbf{B}_0$ field which decreases in strength outwards from the tool axis. As described in Section 3.1., this makes the hydrogen nuclei precess in Larmor frequency. This frequency also determines the frequency of the $\mathbf{B}_1$ pulses. The applied $\mathbf{B}_1$ pulses are used to tip the nuclei in plane with $\mathbf{B}_1$ and re-phase; this controls also the resonant operating frequency of the BMR tool. In the BMR used in Olkiluoto, the frequency was 639 kHz (personal communication with Ryan Gee on 14.1.2020).

According to Qteq (2018) and Coates et al. (1999), the measurement volume of the BMR tool can be defined by varying the operating frequency, since the magnetic field strength and the corresponding Larmor's frequency varies around the tool. For BMR, the volume is a thin shell around the tool with thickness of approximately 1 cm (Figure 9) (personal communication with Ryan Gee on 14.1.2020). The frequency must be chosen by trading off the investigation depth and signal-to-noise ratio; increasing depth avoids drillhole rugosity but degrades the signal-to-noise ratio.

According to Coates et al. (1999) the vertical resolution of NMR tools depends on the antenna length and logging speed. The magnet of the tool extends above and below the

antenna, which allows the tool to polarize the protons before they enter to the sensitive measurement volume. During a CPMG sequence (see Section 3.2.), the antenna detects both the nuclei tipped to the transverse plane and polarized nuclei which have yet not been tipped. This leads to reduction of the measured amplitude of later echoes if the antenna is too short or if the logging speed is too fast. A longer antenna allows faster logging but decreases the vertical resolution. All in all, if the tool does not move during the measurement, the vertical resolution equals to the length of the antenna. If the tool is moved during the measurement, the vertical resolution is a function of the logging speed. For the BMR tool, the vertical resolution for a stationary measurement is 11.5 cm, but when logging at a wireline speed of 1 m/min, the vertical resolution is approximately 14 cm (personal communication with Ryan Gee, 14.1.2020). In this case, the vertical resolution is also the measurement spacing of the BMR tool; the tool gives a reading approximately at every 14 cm. According to Qteq (2018), to keep the signal-to-noise ratio at a reasonable level, the BMR tool performs several individual CPMG sequences to apply vertical averaging. Thus, the vertical resolution will be a function of antenna spacing, measurement speed and degree of applied vertical averaging.

4.1.2. Measurements in the Olkiluoto Island

The measurements were performed in the Olkiluoto Island on 14.-16.6.2019. Geovisor Oy performed the measurements in three drillholes: surface drillhole OL-KR56 and underground ONKALO holes ONK-PP262 and ONK-PP274. Technical information of the drillholes is presented in Table 1. Location of the drillholes is presented in Figure 2. Holes ONK-PP262 and ONK-PP274 are located in ONKALO, at level -374.7 m.

Table 1: Detailed technical information of the drillholes OL-KR56, ONK-PP262 and ONK-PP274. The coordinate information is obtained from ground level or tunnel wall in Finnish National Coordinate System, channel 1. Modified from Toropainen (2011) and Ripatti et al. (2013).

Drillhole	**OL-KR56**	**ONK-PP262**	**ONK-PP274**
Diameter (mm)	75.7	75.7	75.7
Northing	6791526	6792337.52	6792335.65
Easting	1527076	1525340.87	1525341.79
Elevation (m)	7.4	-357.0	-357.5
Thickness of the overburden (m)	2	0.14 concrete	0
Azimuth (degrees)	296	300	299.6
Inclination (degrees)	85	40	38.5
Max. length (m)	1201.7	25.0	23.9

4.1.3. Measurement in drillhole OL-KR56

Drillhole OL-KR56 is located in the southern part of the Olkiluoto island (Figure 2). The measurement was performed on 15.-16.6.2019. The measurement proceeded until the depth of 634.0 m, where the transmitter quit sending the signal. According to personal communication with Benjamin Birt on 24.11.2020, the BMR tool triggered internal protections due to overloading of the antenna, which occurs in a very low resistivity environment. The low resistivity was due to too saline drillhole water.

4.1.4. Measurements in drillholes ONK-PP262 and ONK-PP274

Drillholes ONK-PP262 and ONK-PP274 are located in ONKALO (Figure 2). The measurements were performed on 14.6.2019. In Figure 10, measurement of the drillhole ONK-PP262 is about to start. Significant noise appeared and the noise was stronger than the signal. Due to the signal quality, the data from drillholes ONK-PP262 and ONK-PP274 is not used in this study.

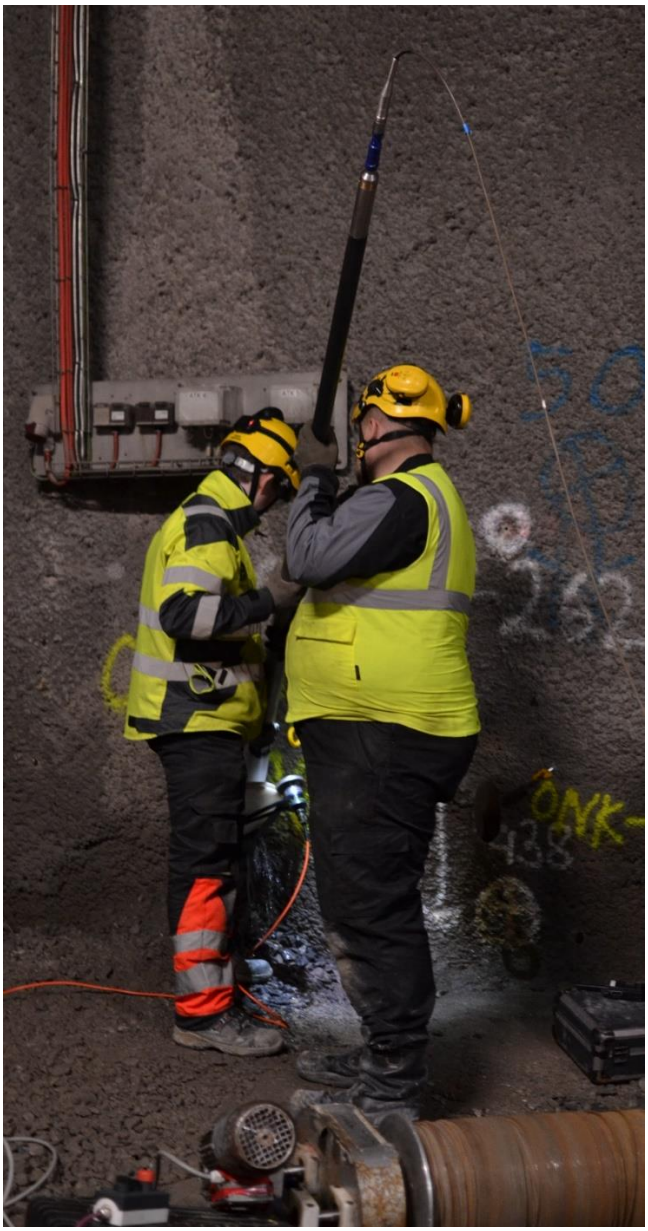

Figure 10: BMR tool about to enter the drillhole ONK-PP262 in ONKALO.

The noise was due to magnetizing materials in ONKALO and possibly, some formation effects of the drillhole. NMR tools are disturbed by magnetic fields formed in other objects and require a fairly undisturbed environment to perform a measurement with reasonable noise-to-signal ratio. Since the drillholes ONK-PP262 and ONK-PP274 are only 25.0 m and 23.9 m in length (Table 1), the BMR tool got disturbed by magnetizing objects located in the measurement area. For example, the tunnel walls of ONKALO are reinforced with shotcrete containing small steel fibers, which get easily magnetized.

4.2. Earlier drillhole studies

4.2.1. Geological studies

Comprehensive geological logging has been made on the core of the OL-KR56 drillhole by Posiva Oy and Suomen Malmi Oy in 2012. The core was also photographed in the core boxes of which two core boxes are shown in Figure 11. The geological logging starts with lithological logging by accuracy of 1 meter, with estimated leucosome content and a written description of the lithological unit. Fracture logging determines depth of all open and closed fractures, their orientation (alpha and beta directions), real dip and dip directions of the fractures calculated from the alpha and beta directions, color of the fracture surface, fracture filling minerals and their thicknesses by accuracy of 0.1 mm, type of the fracture (closed, filled, open, slicken sided, grain filled), fracture profile, joint roughness number, joint alteration number and classification of the fractured zone. Foliation logging includes foliation direction (alpha, beta, dip and dip direction) estimated for sections irregular in length which have the same direction. Foliation type, intensity and rock type are determined for sections 1.0–3.0 m in length. The logging also includes Q-class (rock quality) classification, fracture frequency and RQD (rock quality designation) estimates, fracture zones and core loss determination, weathering degree estimates, core orientation determination and core discing sections. The drillcore logging results from OL-KR56 have been summarized by Toropainen (2012). The following description is based on the Toropainen (2012) report.

OL-KR56 core at 87.31-95.58 m

Figure 11: Two coreboxes of OL-KR56 drillhole core from depth 87.3–95.6 m. Modified from Posiva Oy and Suomen malmi Oy (2012 B).

The drillcore consists mostly of veined gneiss (34.5 %), diatexitic gneiss (32.1 %), pegmatitic granite (13.8 %) and mica gneiss (13.0 %). Tonalite-granodiorite-granite, K-feldspar porphyry and quartz gneiss sections were also found. Graphic log of the lithological and fracture logging is in Appendix B.

2/3 of the core consists of migmatitic gneisses (diatexitic gneiss and veined gneiss) with almost equal proportions. In the first 725.0 m of the drillcore, the diatexitic gneiss is more abundant and the veined gneiss dominates the deeper part. Pegmatitic granite occurs mainly at 40.0–75.0 m and 330.0–790.0 m. Short sections occur irregularly along the drillcore. Mica gneiss occurs as short inclusions in migmatitic gneisses and as longer sections at 70.0–180.0 m and 720.0–1030.0 m. Both mica gneiss and quartz gneiss occur also as local sections and were interpreted as separate rock types when the width of the section was more than one meter. The quartz gneiss occurs at the depths of 575.9–576.9

m, 677.3–678.9 m and 1153.5–1155.0 m. Tonalite-granodiorite-granite occurs as one to nine meters long sections at the depths of 300.0–375.0 m and 790.0–950.0 m. K-feldspar was found only as one short section from depth of 202.5–206.6 m.

2780 fractures were recorded from the drillcore (see Appendix B). 1822 of the fractures (65.5 %) are filled fractures, 632 (22.7 %) are filled slickensided fractures, 184 (6.6 %) are tight fractures, 95 (3.4 %) are open fractures and 47 (1.7 %) are grain filled fractures.

Most fractures zones are scattered along the drillhole, but two significant fracture zones were recognized at depths of 80.0–200.0 m and 347.0–444.0 m. In these zones, the rock is highly fractured or even partly crushed and fracture fillings are often thick and consisting of clay minerals. The 80.0–200.0 m zone is constituted of two brittle zones: at 78.4–99.8 m the drillhole intersects brittle joint intersection (KR56-BJI-7842-9977) and at 141.2–175.8 m brittle fault zone (BFZ327) (OL-KR56 hauraat lävistykset -table, 2020, unpublished). According to Vaittinen et al. (2020), BFZ327 has been suspected to be connected to HZL11, which intersects the drillhole at 122.7–124.7 m (discussed more in Section 2.4.). In OL-KR57, HZL11 and BFZ327 occur at the same depth, but in OL-KR56, BFZ327 begins 20.0 m deeper than HZL11. The 347.0–444.0 m zone is the crossing of BFZ146 connected to HZ146 (discussed more in Section 2.4., see also Figure 3). According to Toropainen (2012), most of the other, scattered fractures have an undulated surface shape, rough profile and high joint roughness number, which indicated high friction on the fracture surface. These fractures are usually filled or tight with low to moderate (0.75–3) joint alteration number. There is an unusually high number of tight fractures compared to other drillcores drilled in Olkiluoto. This is probably at least partly due to the mica gneiss rich lithology; it seems to preserve old and healed fractures during partial melting. No other clear dependency on lithology is seen in the fracture logging.

4.2.2. Hydrogeological studies

The OL-KR56 drillhole has been measured with 1) Hydraulic Testing Unit (HTU) and 2) Posiva Flow Log, Difference flow method (PFL DIFF).

The following description is based on the HTU measurement report of drillhole OL-KR56 by Pulkkinen and Hurmerinta (2019). HTU equipment measures in-situ hydraulic conductivity of a drillhole. The downhole probe consists of two packers isolating the measured section, pressure sensors recording the pressure in the section, a temperature sensor and a single point resistance electrode (see Figure 12). For OL-KR56, the packer spacing was 2.0 m and the measurement begun from depth of 300.0 m and ended when the lower packer reached 702.0 m. The measurement starts with inflating the packers with a pressure of approximately 800 kPA. After this, the pressure is stabilized close to the natural pressure and measured in the test section and above and below the packers. Then, injection is started and continued until a stationary flow is reached. In the final stage, before moving the HTU probe to next position, the packers are deflated, and recovery of the pressure is recorded. As a result, the HTU equipment calculates hydraulic conductivity with three different interpretation methods: Moye, Horner and 1/Q (Ylinen 1994, Kuusela 1986). The resulting hydraulic conductivity represents the whole drillhole length limited by the packers, which includes also intact bedrock and may have either one or multiple fractures. In OL-KR56, the hydraulic conductivity values fall mostly between 10^{-11}-10^{-10} m s^{-1} with higher values resulting only from crossing HZ146 at depth of 339.6–385.8 m (see Figure 3). Results from the HTU measurement are summarized in Figure 13, which also shows elevated transmissivities around HZ146 at 340.0–380.0 m.

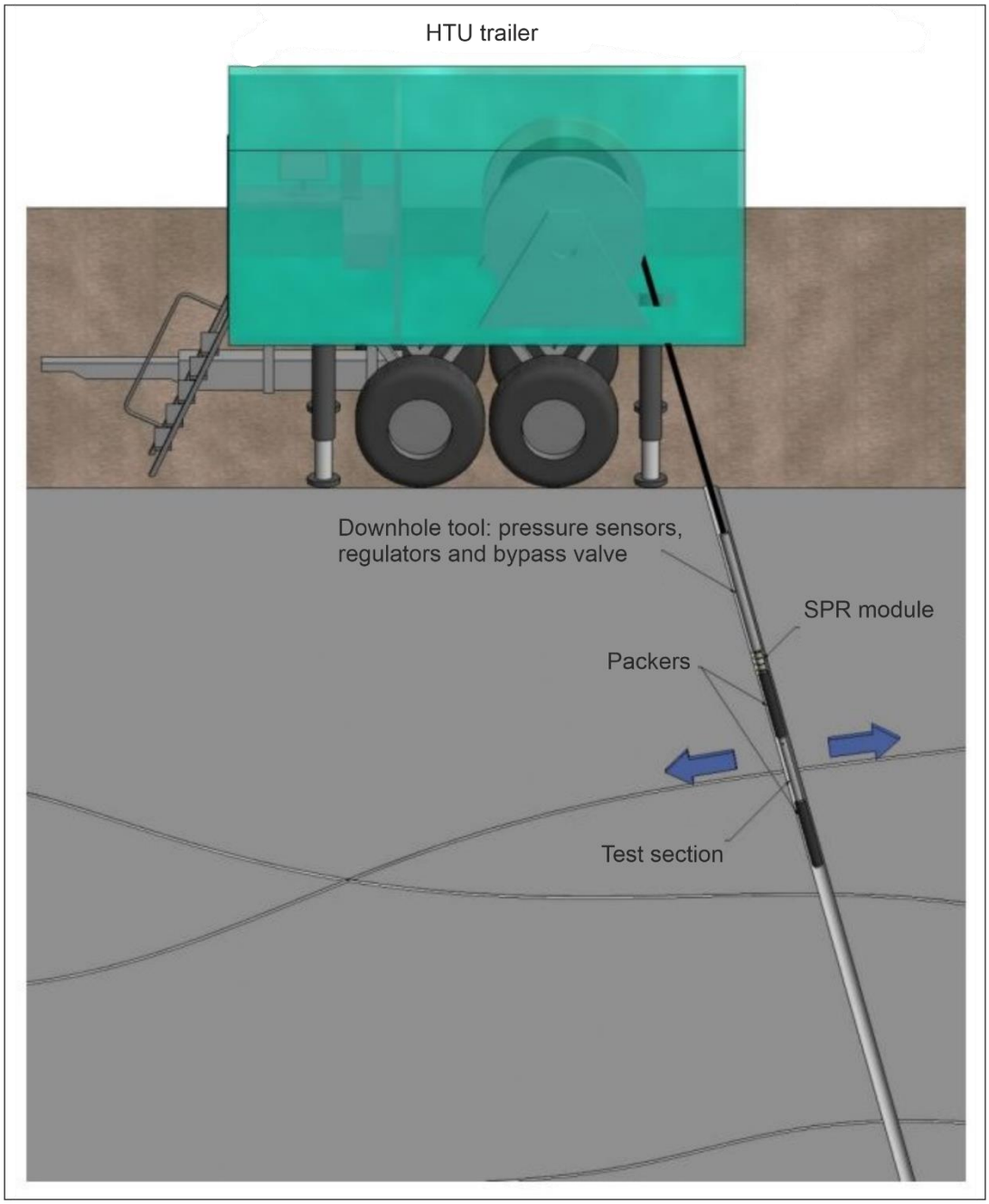

Figure 12: Schematic picture of the HTU system configuration. SPR = Single Point Resistance. Modified from Pulkkinen and Hurmerinta (2019).

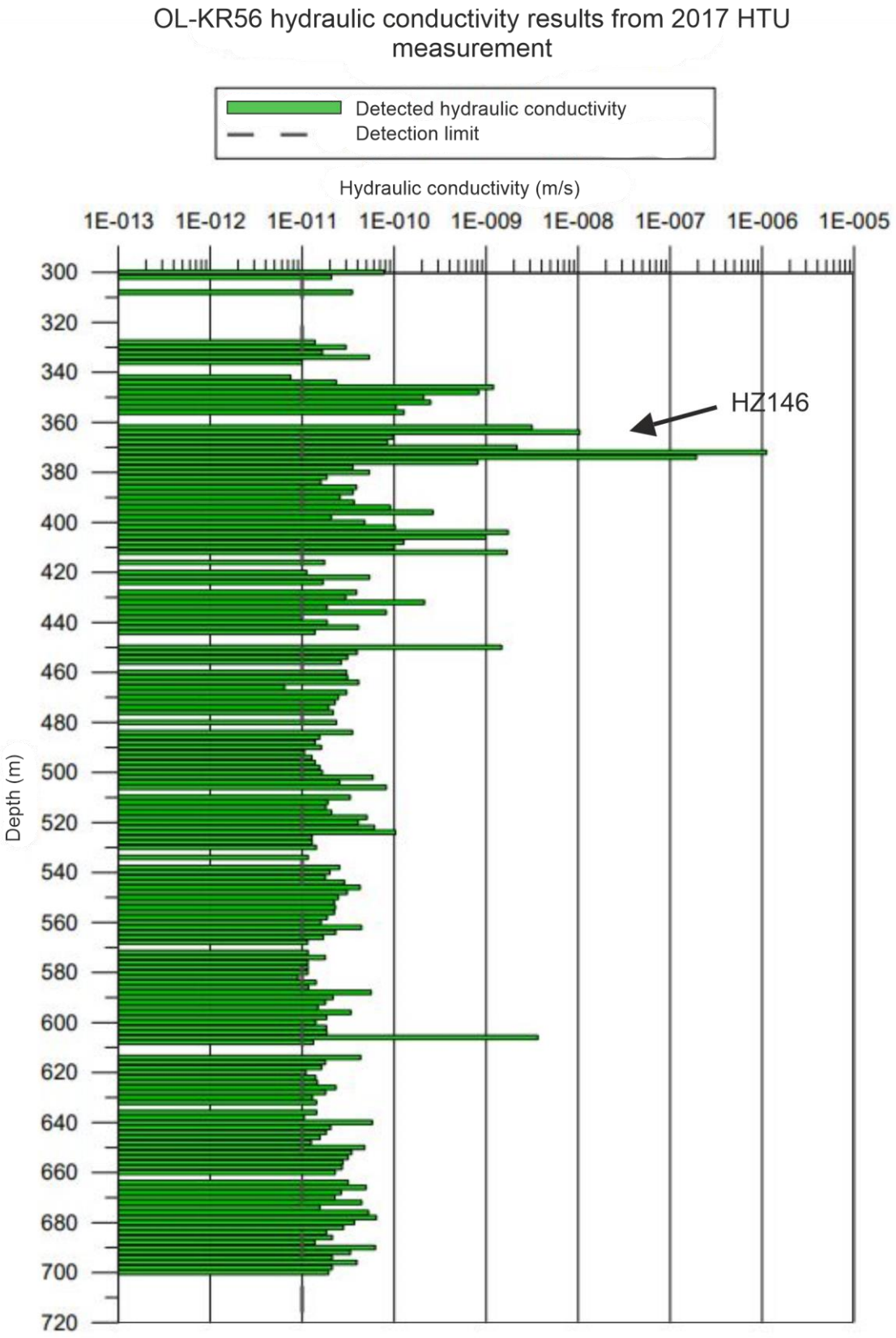

Figure 13: Summarized hydraulic conductivity results from HTU measurement performed in 2017 in OL-KR56. HZ146 (see Figure 3) shows elevated hydraulic conductivity around 339.6–385.8 m. Modified from Pulkkinen and Hurmerinta (2019).

According to e.g. Ripatti et al. (2013), the PFL DIFF probe measures groundwater flow in or out of defined section of the drillhole. The probe isolates the desired section with two packers and flow inside the section is directed through a flow sensor, see Figure 14.

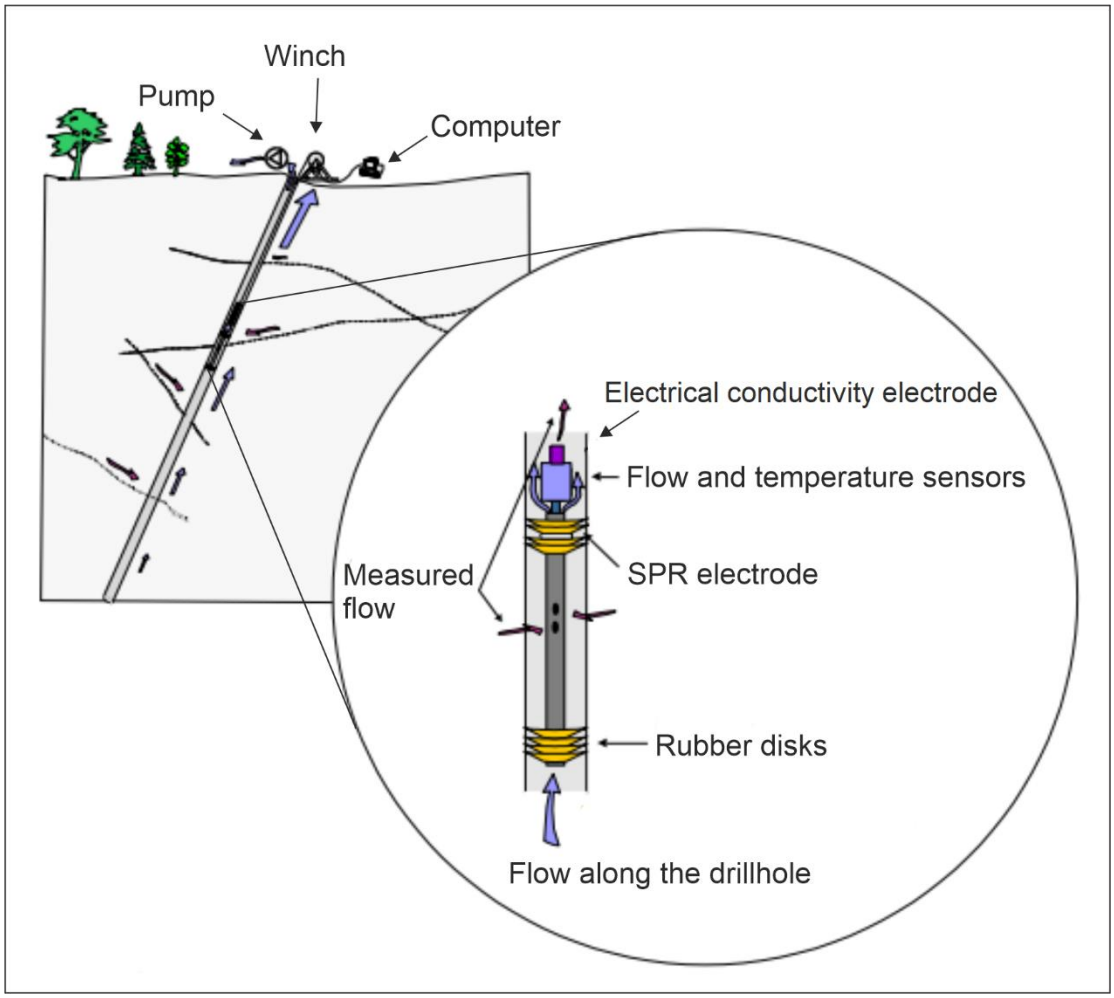

Figure 14: Schematic picture of PFL DIFF probe. SPR = Single Point Resistance. Modified from Ripatti et al. (2013).

Flow along the drillhole is directed around the section with a bypass pipe and discharged from upper or lower end of the probe. Thermistors are used to monitor flow rates into or out the section tracking dilution and its transfer by the moving water. The measurement is performed in both natural conditions and when pumping water out from the drillhole. For OL-KR56, two separate measurements were conducted with packer spacings 0.5 m and 2.0 m. As a result, the PFL DIFF estimates fresh water head into or out from the drillhole with and without pumping, and flow from a fracture to the drillhole or from drillhole to a fracture with and without pumping. Also, fresh water head in the fracture

and PFL transmissivity are determined. PFL transmissivity is determined with two different formulas: Dupuit formula (Marsily 1986) is used in the pumping phase, assuming a cylindrical and steady state flow and Moye formula (Moye 1967) when the flow is assumed to be steady state and cylindrical near the drillhole and spherical further away. The PFL DIFF tool has additional single point resistance electrodes, which are utilized in determining depth of fractures and electrical conductivity electrodes to determine electrical conductivity of both drillhole water and water flowing from the fractures (Figure 14). Sum of the detected flows and transmissivities for the entire drillhole are presented in Table 2. Graphical results for the whole drillhole are summarized in Figure 15, where crossing of HZ146 (see Figure 3) can be seen at depth of 320.0–410.0 m as elevated PFL transmissivity. PFL receives transmissivity values also at 80.0–200.0 m, which is probably due to the two brittle zones and HZL11 intersecting the drillhole (discussed more in Section 4.2.1.).

Table 2: results from PFL DIFF measurement from OL-KR56. Flow 0 is derived from fresh water head without pumping with 2.0 m packer spacing. Notice the negative value; the flow direction is from the drillhole into the bedrock. Flow 1 is derived from fresh water head with pumping with 2.0 m packer spacing. Flow 2 is derived from fresh water head with pumping with 0.5 m packer spacing. Results are sums from the entire drillhole.

Measured variable	**Result**
Flow 0 (mL/h)	-282
Flow 1 (mL/h)	448 210
Flow 2 (mL/h)	447 882
Maximum flow along the drillhole with pumping (mL/h)	982 435
PFL transmissivity with Dupuit formula (m2/s)	1.58·10-5
PFL transmissivity with Moye formula (m2/s)	2.71·10-5
Sum of 2.0 m sections (m2/s)	1.21·10-5
Sum of fractures (m2/s)	1.22·10-5
Pumping rate (mL/h)	576 000

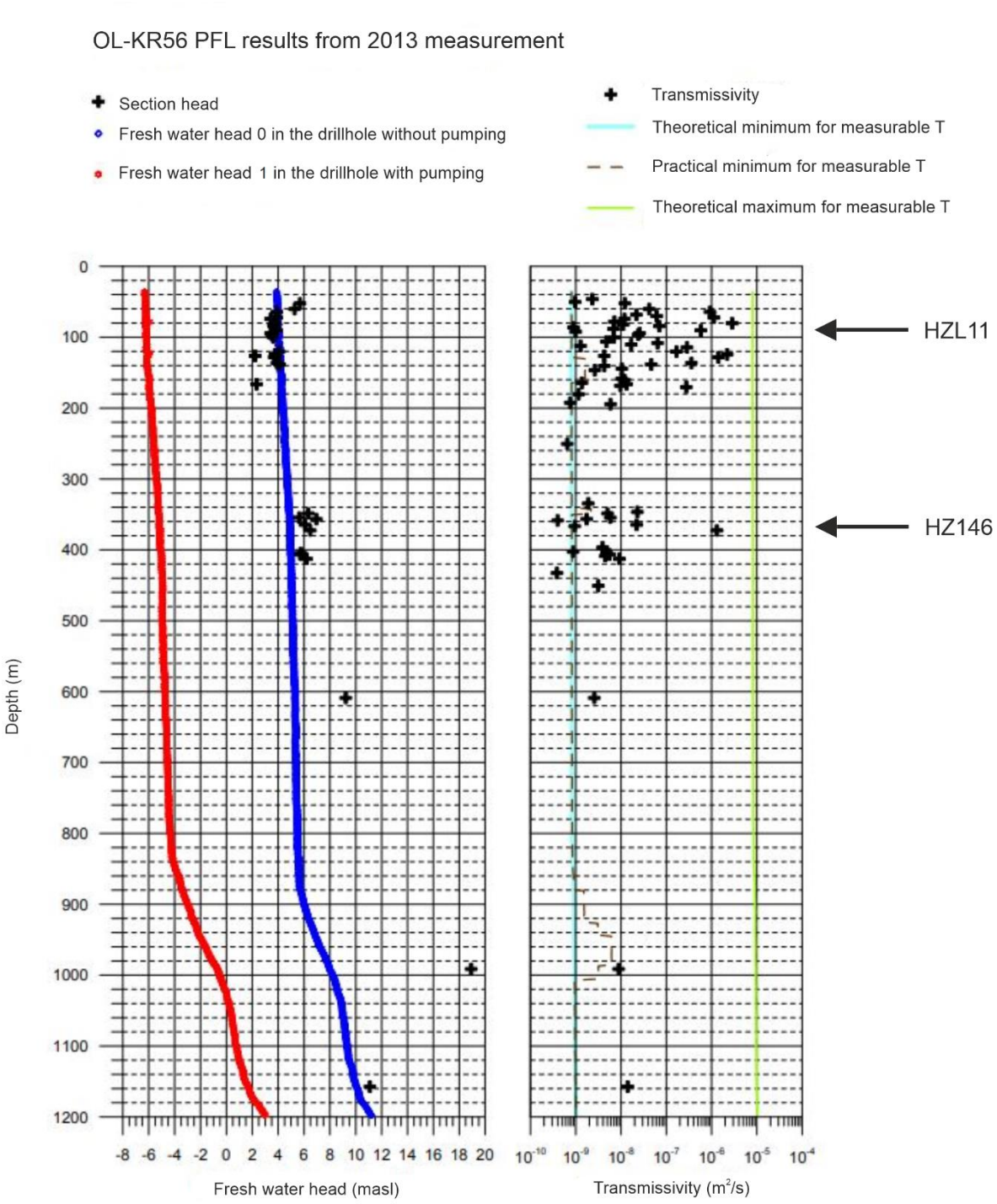

Figure 15: Summarized fresh water head 0 (fresh water head without pumping with 2.0 m packer spacing), fresh water head 1 (fresh water head with pumping with 2.0 m packer spacing) and transmissivity results from PFL measurement performed in 2013. HZL11 and other brittle structures show elevated transmissivity around 80.0–200.0 m and HZ146 around 320.0–410.0 m. Modified from Ripatti et al. (2013).

4.2.3. Geophysical studies

Multiple geophysical studies have been conducted in OL-KR56. A summary of the studies is shown in Table 3.

Table 3: geophysical studies conducted in OL-KR56 drillhole.

Data	**Description**
Optical imaging	Optical televiewer imaging
Acoustic imaging	Acoustic televiewer imaging
Caliper, mechanical	Drillhole diameter
Caliper, from acoustic image	Drillhole diamater interpreted from acoustic image
Fluid resistivity, interpreted	Apparent total dissolved solids calculated from recalibrated resistivity data
Fluid resistivity, processed	Groundwater resistivity in situ and in temperature of 25 C
Sonic full wave form logging, interpreted attenuation	P-wave, S-wave and tubewave attenuation calculated from amplitude ratio between 0.6 and 1.0 m channels
Sonic full wave form logging, interpreted attenuation with four receiver probe	P-wave, S-wave and tubewave attenuation calculated from amplitude ratio between 0.6 and 1.0 m channels
Sonic full wave form logging, interpreted rock mechanics parameters	Youngs modulus, shear modulus, bulk modulus, poisson ratio and apparent Q prime calculated from density and P- and S-wave velocities.
Sonic full wave form logging, interpreted rock mechanics parameters with four receiver probe	Youngs modulus, shear modulus, bulk modulus, poisson ratio and apparent Q prime calculated from density and P- and S-wave velocities from semblance analysis.
Sonic full wave form logging, processed with four receiver probe	P- and S-wave velocities and tube wave energy with semblance analysis.
Sonic full wave form logging, processed with 1.0 m transmitter and receiver separation	P- and S-wave velocities and tube wave energy.
Sonic full wave form logging, processed with 0.6 m transmitter and receiver separation	P- and S-wave velocities and tube wave energy.
Gamma-gamma density, processed	Bedrock density calibrated with petrophysical data of the site
Induced polarization	Bedrock resistivity and chargeability
Natural gamma, QL	Gamma radiation intensity measured with elog
Natural gamma, SH	Gamma radiation intensity measured with gamma-gamma density
Resistivity logging	Bedrock resistivity with Dakhnov correction measured with Elog and with Dual Laterlog deep and shallow
Single point resistance	Bedrock resistance
Magnetic susceptibility	Susceptibility calibrated to test block and level calibrated statistically to petrophysical data

5. RESULTS

This section presents the results of the BMR measurements, processing of the BMR data and comparison to other drillhole data methods. The results are only from the surface drillhole OL-KR56, because of signal quality problems in the other drillholes (discussed in Section 4.1.2.). The results are only shown for the first 635.0 m of the drillhole OL-KR56 due to shut down of the BMR transmitter at this depth. All BMR logs from the OL-KR56 measurement are presented in Appendix A.

5.1. Data processing parameters

First, the BMR data were processed with the NMRSA Post Processing module in Well-CAD. The module allows the user to modify multiple parameters of which moving averages, temperature-related parameters and cutoff values were adjusted. For other processing parameters, the default values were considered to be reasonable. The available processing parameters are listed and explained in Table 4 (personal communication with Ryan Gee on 13.1.2020), along with the tested parameters and final chosen values. When conducting the processing tests, other parameters except for the one that was being tested, were kept at default values (Table 4).

For the testing of the processing parameters, a representative test section was chosen at depth of 532.0–611.0 m (first 9.0 m are shown in Figure 16, where the data has been processed with the chosen processing parameters). This section has clear variations in T_2 distribution, some variation in lithology, both fractured zones and intact bedrock and only minor noise. Depth correction was performed by shifting the logs 4.5 m upwards by comparing the BMR logs (natural gamma, T_2 distribution, total porosity, water content and permeability logs) to Posiva's corrected reference logs (including e.g. natural gamma. seismic velocities, acoustic and optical images, HTU and PFL data). This correction is only approximate; precise correction by anchor points cannot be done for a short section, since comparison to the reference logs is difficult. However, for a short section, the shifting provides a reasonable depth correction, because depth difference remains small within short depth intervals.

Table 4: Processing parameters, parameter options, default values, tested values, chosen values and description. * = tested later in more detailed processing in NMR Workspace.

Parameter	Parameter options	Default value	Tested values	Chosen value	Description
Moving averages	integer	1	1, 3, 5	3	A smoothing function, creates a series of averages of different subsets
Ignore echoes	integer	0	not tested	0	The selected value tells how many echoes are ignored starting from the beginning of the CPMG sequence
Showgui	true/false	true	not tested	true	Display of certain plots in a processing window
Cutoff 1	decimal	3.00e-03	not tested	3.00e-03	Clay bound water cutoff, separates clay bound water from capillary bound water
Cutoff 2*	decimal	3.30e-02	not tested	3.30e-02	Capillary bound water cutoff, separates capillary bound water from moveable water
Cutoff 3*	integer	5	not tested	3	Moveable water cutoff, separates moveable water from noise
T2 start	decimal	1.00e-04	not tested	1.00e-04	Start time for the T2 distribution measurement
T2 end	integer	10.0	not tested	10.0	End time for the T2 distribution measurement
Steps	integer	128.0	64, 128	128	Steps break the T2 distribution into small time steps to determine the porosity in each pore size.
Temp source		geothermal_gradient	not tested	geothermal_gradient	Definition of a chosen temperature gradient
Surface temp	integer	21	not tested	21	Temperature in Celsius at surface level
Temp gradient	decimal	2.2	2.20, 1.4	1.4	Temperature gradient as Celsius / 100 m
Differential	integer	8	not tested	8	Display of certain plots in a processing window
Apply calibration	true/false	true	not tested	true	Display of certain plots in a processing window
Burst	true/false	true	true, false	true	First part of the signal representing small pores
Main	true/false	true	true, false	true	Second part of the signal representing larger pores
Echo multipliers	decimal	[1.21 , 0.95]	not tested	[1.21 , 0.95]	Display of certain plots in a processing window
T1 T2 ratio	decimal	1.6	not tested	1.6	Process for fitting the burst data onto the main

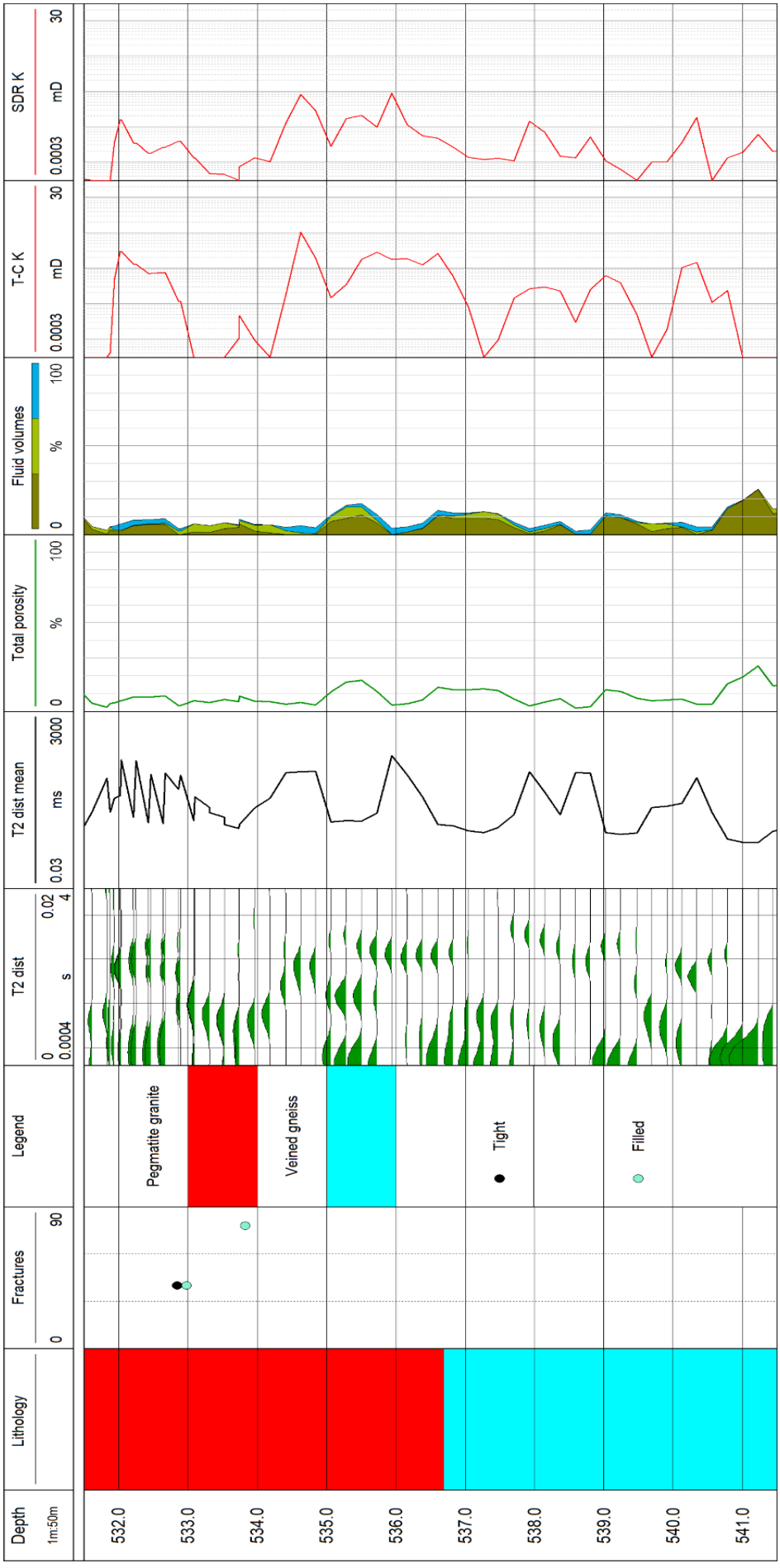

Figure 16: First 9.0 m of the test section, 532.0–541.0 m processed with the chosen values. Lithology. T_2 distribution (T2 dist) , T_2 distribution mean (T2 dist mean) total porosity, fluid volumes and Timur-Coates (T-C K) and Schlumberger-Doll (SDR K) permeabilities. Legend has lithological units and fracture types. Filled fracture has fracture filling minerals, tight fracture has no filling minerals. In the fracture log, scale 0 to 90 is dip of the fracture.

5.1.1. Main and burst sequences

The BMR measurement begins with tipping the spinning nuclei polarized to the direction of the $\mathbf{B}_0$ field with the oscillating $\mathbf{B}_1$ field (Section 1.1. in Theoretical background). Pulses of the $\mathbf{B}_1$ field create a decaying series of spin echoes, which is the raw data recorded by the BMR tool (Figure 6 in Theoretical background). The spin echo data is transferred to T_2 distribution by echo-fitting (Section 3.4. in Theoretical background). Data processing begins in WellCAD by choosing suitable processing parameters.

True and false were tested for main and burst sequences (Table 4) with three different options: 1. Main set to false (off) and burst set to true (on), 2. Main set to true and burst set to false and 3. Both set to true (default setting). Results for the test section are in Figures 17, 18 and 19.

Changing the burst sequence to false does not seem to have significant effect on the results; the logs do not show any observable difference. Setting main to false changes the T_2 distribution significantly. This is seen as smoother signal in the T_2 distribution log (Figure 17), and thus total porosity, water volumes (Figure 18) and permeabilities (Figure 19) are generally lower. In the water volumes, the volumes of different bounding type water are changed, but the change does not show consistency. Around 536–537 m, T_2 distribution log shows significant number of small pores (marked by arrow in Figure 17), while other logs have only very minor signal. This can be seen as increased total porosity, water content and permeability.

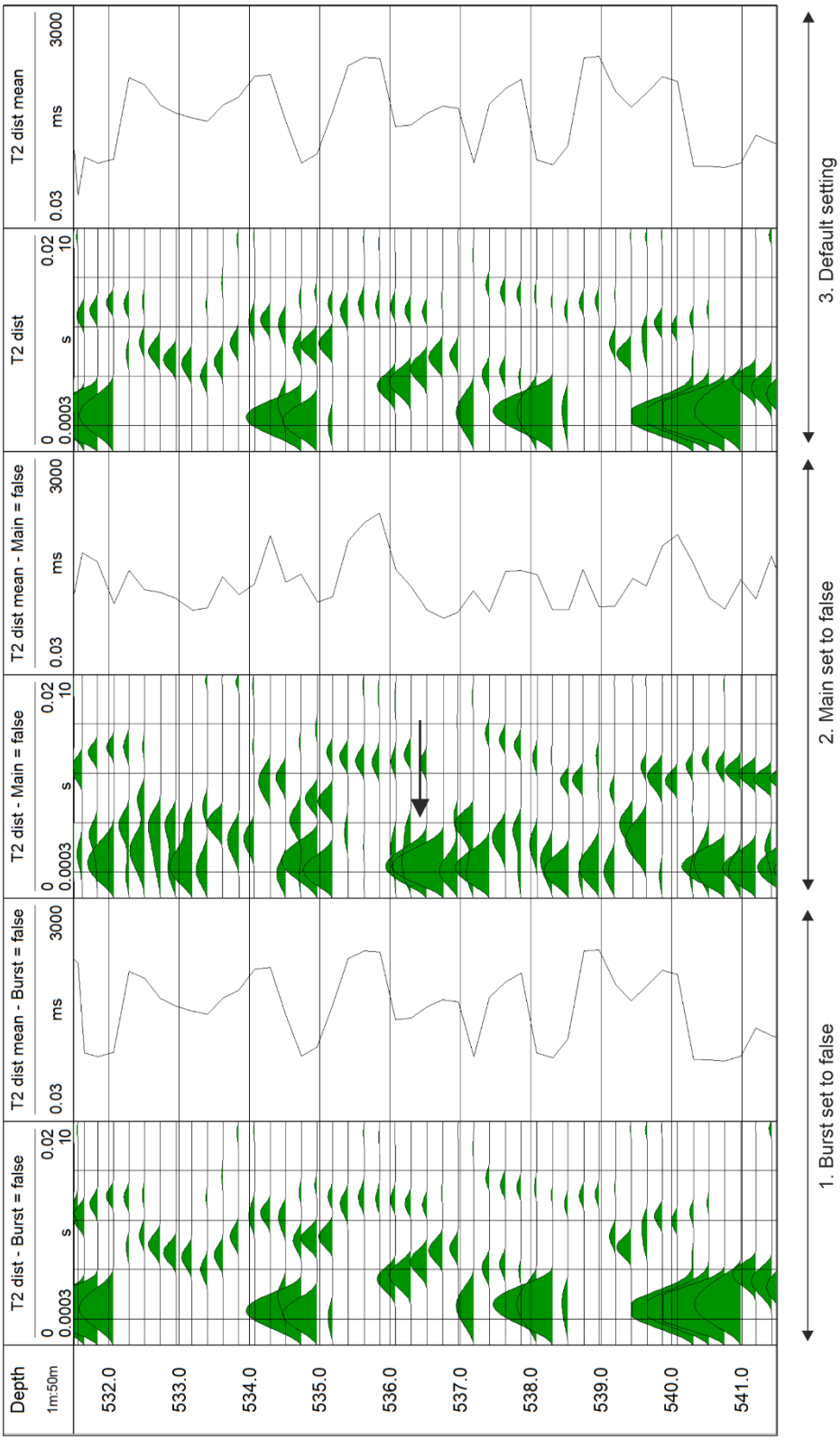

Figure 17: T_2 distribution (T2 dist) and T_2 distribution mean (T2 dist mean) with 1. Main set to true and burst set to false 2. Main set to false and burst set to true 3. Both set to true (default setting). Other processing parameters were kept at default settings. Around 536–537 m in main set to false logs, T_2 distribution shows large number of small pores, which is marked with an arrow. T_2 distribution log has two scales: top one is amplitude in meters and bottom one is relaxation time in seconds

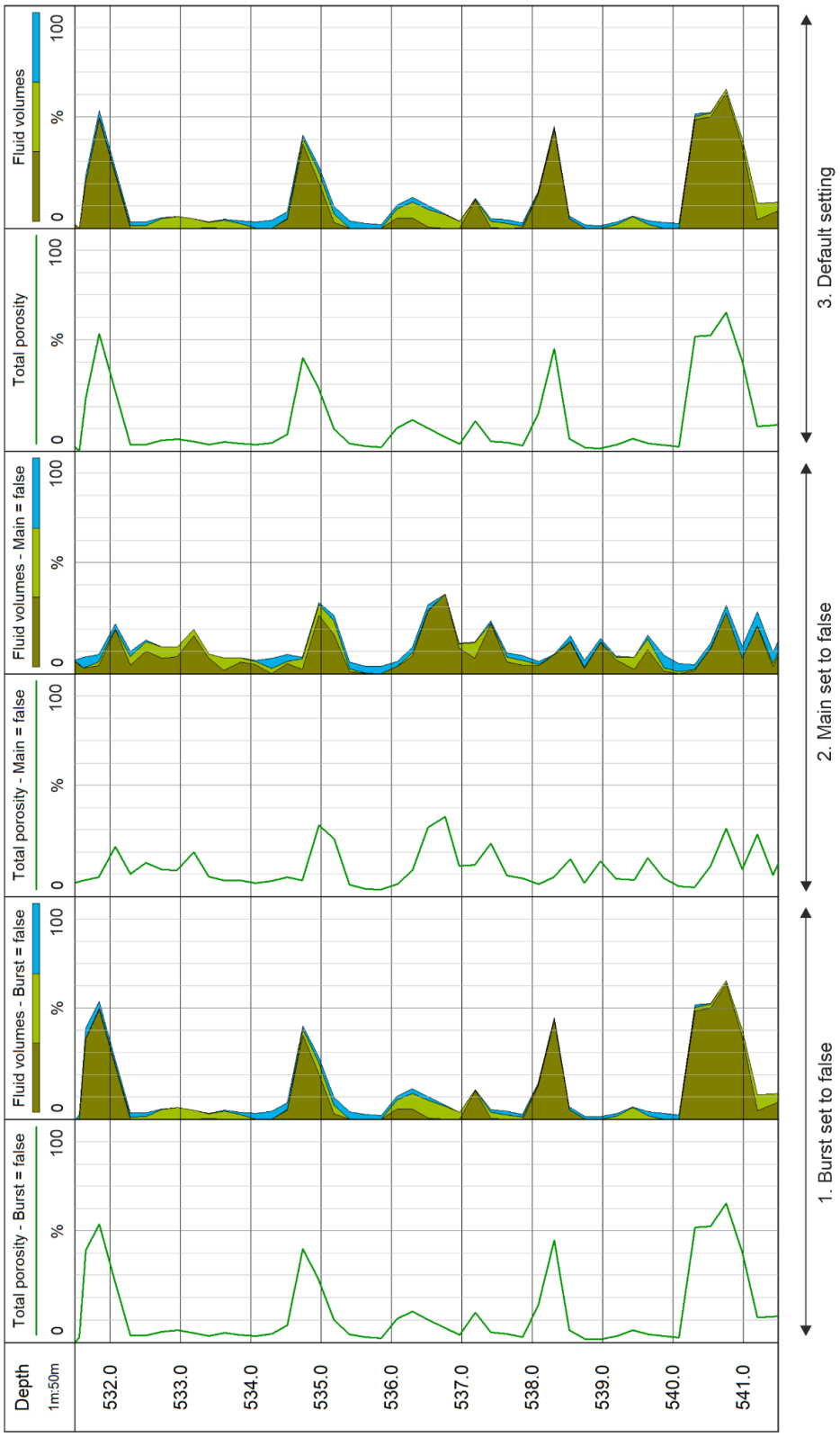

Figure 18: Total porosity and fluid volumes (dark green is clay bound water, light green is capillary bound water and blue is moveable water) 1. Main set to true and burst set to false 2. Main set to false and burst set to true 3. Both set to true (default setting). Other processing parameters were kept at default settings.

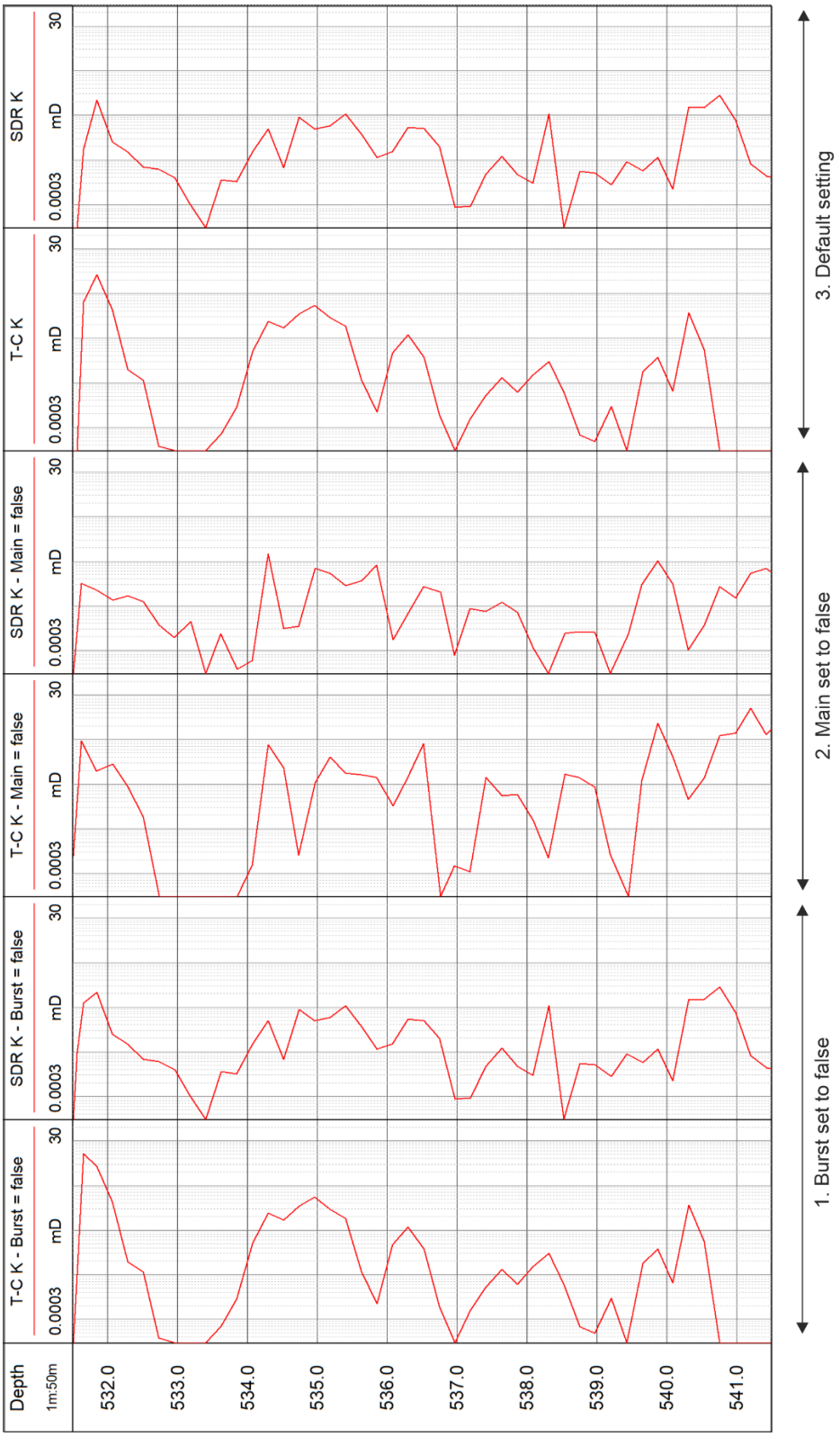

Figure 19: Timur-Coates (T-C) and Schlumberger-Doll (SDR) permeabilities 1. Main set to true and burst set to false 2. Main set to false and burst set to true 3. Both set to true (default setting). Other processing parameters were kept at default settings.

5.1.2. Moving averages

Values 1 (default setting), 3 and 5 were tested for moving averages (Table 4). Averaging emphasizes the signal and cancels out noise. Essentially, the objective was to find a value, which smooths out the noise but leaves the data peaks visible. Results from a test section are in Figures 20, 21 and 22. After running the processing tests, it was observed that value 3 is the most suitable; the data peaks remain visible but most of the noise smooths out. The data peaks were confirmed by comparing the NMR data to other drillhole logs, e.g. to optical and acoustic images, core logging and PFL DIFF data. The default value, which is suitable for most sedimentary environments, is 1. With moving averages set to 1, the log shows some noise (excessive peaks on the left side of the T_2 distribution, which affects also all the other logs) and overlapping in the T_2 distribution (seen in Figure 20, e.g. at depth of 536.0–537.0 m). With moving averages set to 5, the log seems to lose some of the data peaks (the most visible difference is in the total porosity log, Figure 21). In Figure 20, at depth of 535.8 m T_2 distribution has some signal on the right side of the log which is lost when moving averages is set to 5. This also reduces the T_2 distribution mean significantly.

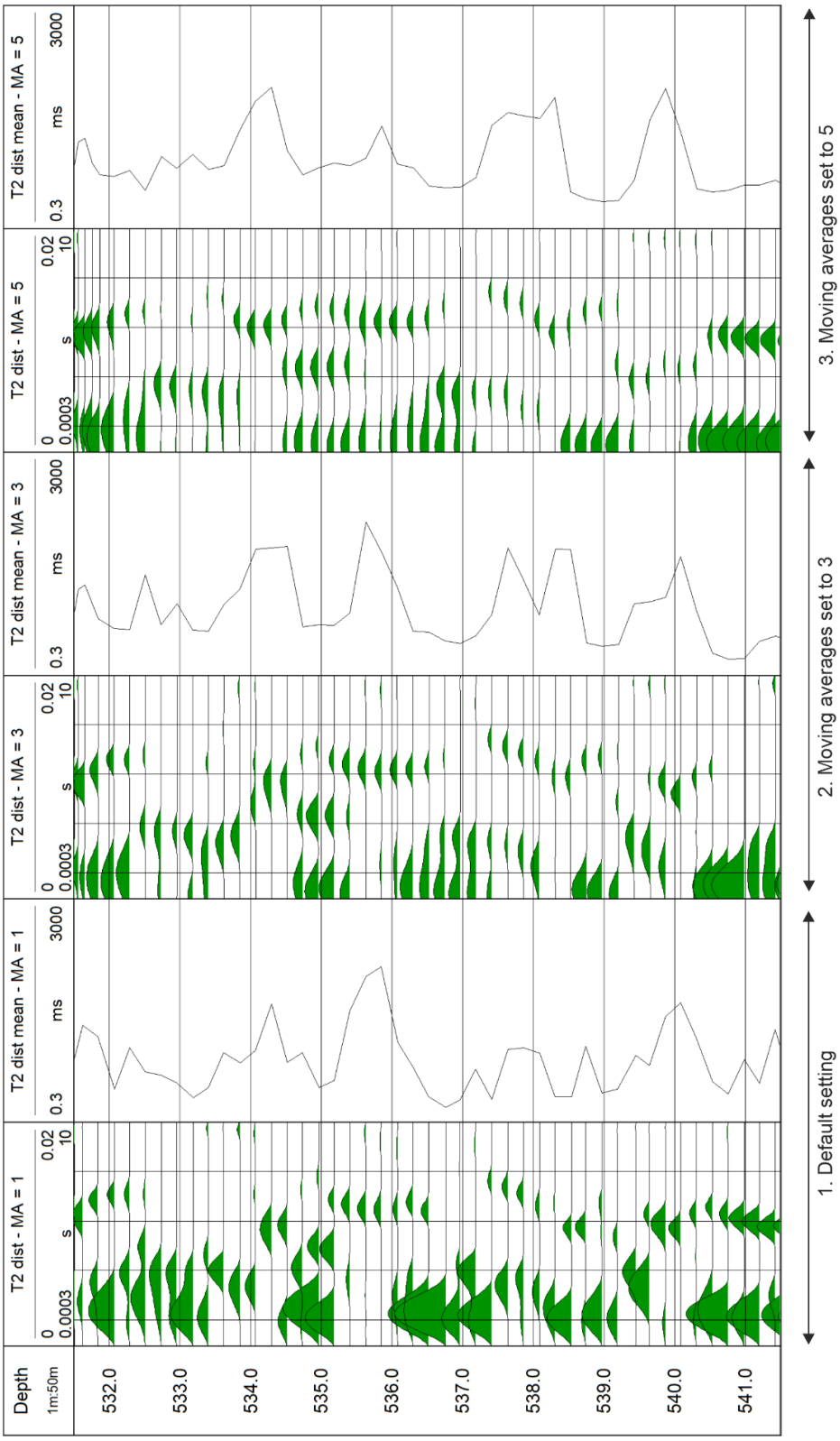

Figure 20: T_2 distribution (T2 dist) and T_2 distribution mean (T2 dist mean) with 1) Moving averages set to 1 (default setting), 2) Moving averages set to 3 and 3) Moving averages set to 5. Other processing parameters were kept at default settings. T_2 distribution log has two scales: top one is amplitude in meters and bottom one is relaxation time in seconds.

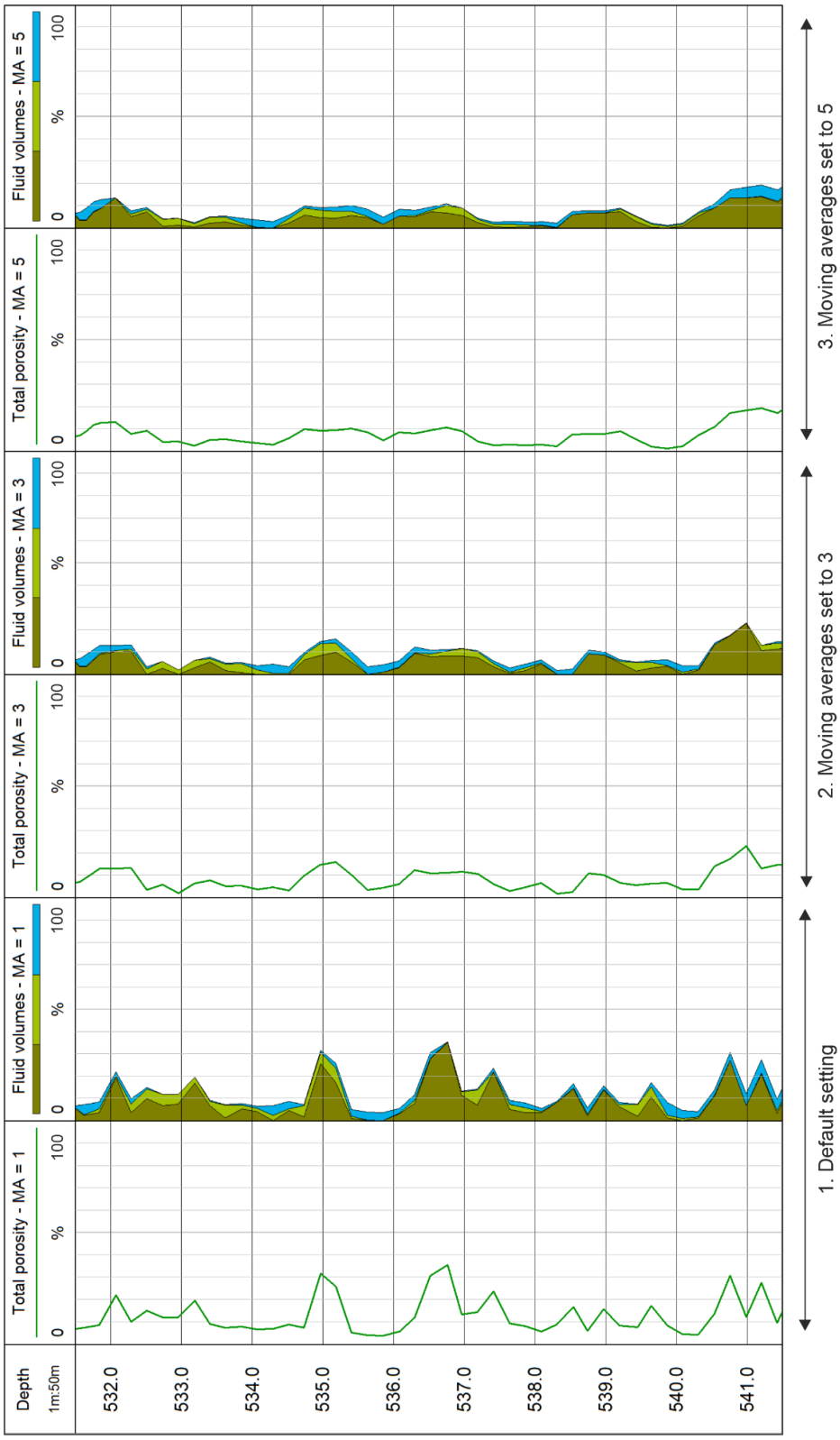

Figure 21: Total porosity and fluid volumes (dark green is clay bound water, light green is capillary bound water and blue is moveable water) with 1) Moving averages set to 1 (default setting), 2) Moving averages set to 3 and 3) Moving averages set to 5. Other processing parameters were kept at default settings.

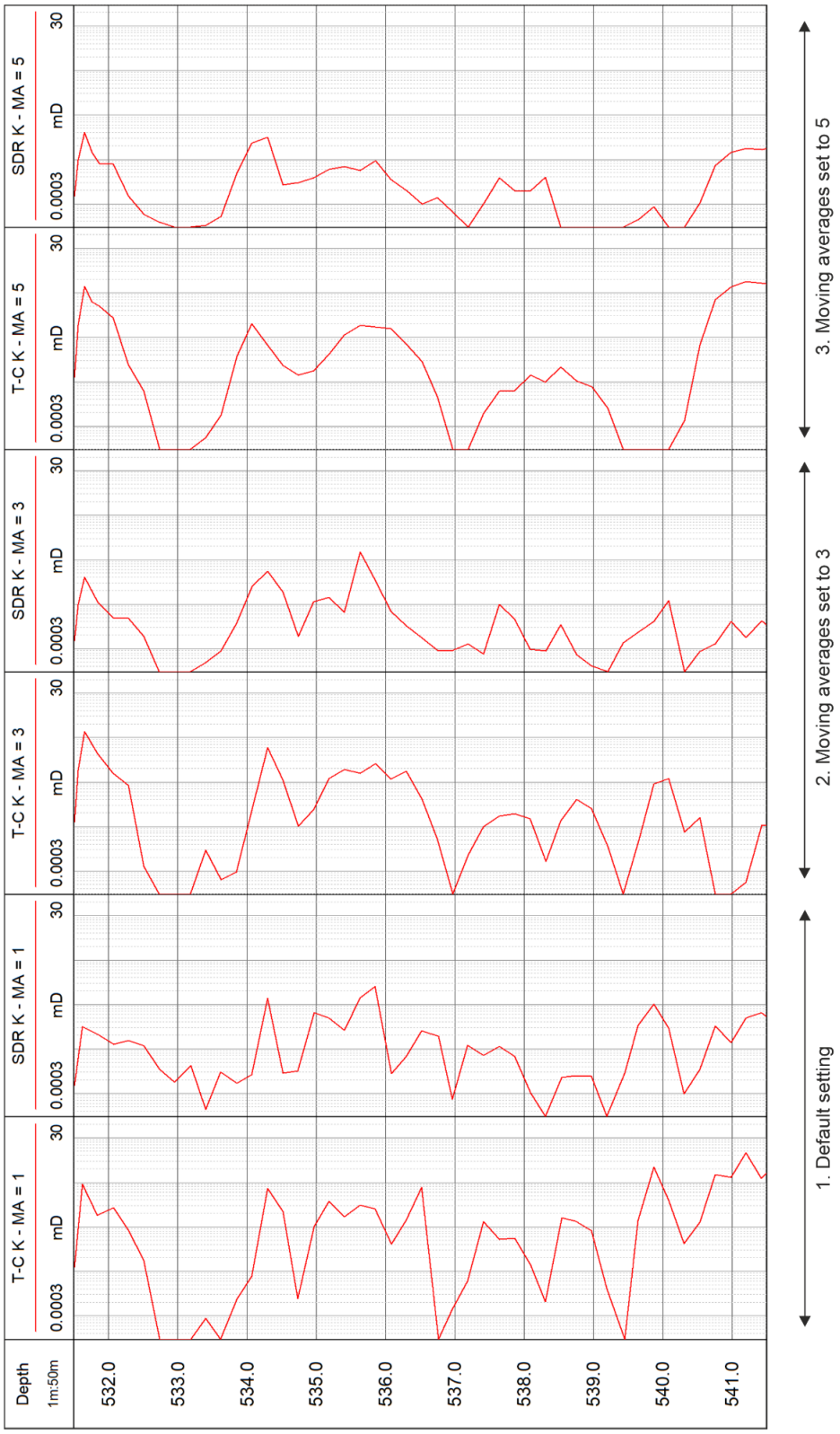

Figure 22: Timur-Coates (T-C) and Schlumberger-Doll (SDR) permeabilitites with 1) Moving averages set to 1 (default setting), 2) Moving averages set to 3 and 3) Moving averages set to 5. Other processing parameters were kept at default settings.

5.1.3. Temperature gradient

Values 1.4 °C / 100.0 m and 2.2 °C / 100.0 m (default setting) were tested for temperature gradient. The default value, which is typical in sedimentary environments, is 2.2 °C / 100.0 m but in Olkiluoto the temperature gradient is 1.4 °C / 100.0 m (Sedighi et al. 2014). The temperature at depth depends also on the surface temperature, which has a default value of 21 °C. Surface temperature was not recorded on the measurement day and thus, the default value was used. The default value is probably close to the real temperature; the measurement was performed in June, when 21 °C is a typical temperature in Olkiluoto in daytime (Ikonen 2007).

No significant differences were found in the processing tests. However, it was decided to use real values (1.4 °C / 100.0 m) instead of estimate. Results from the test section are in Figures 23 and 24.

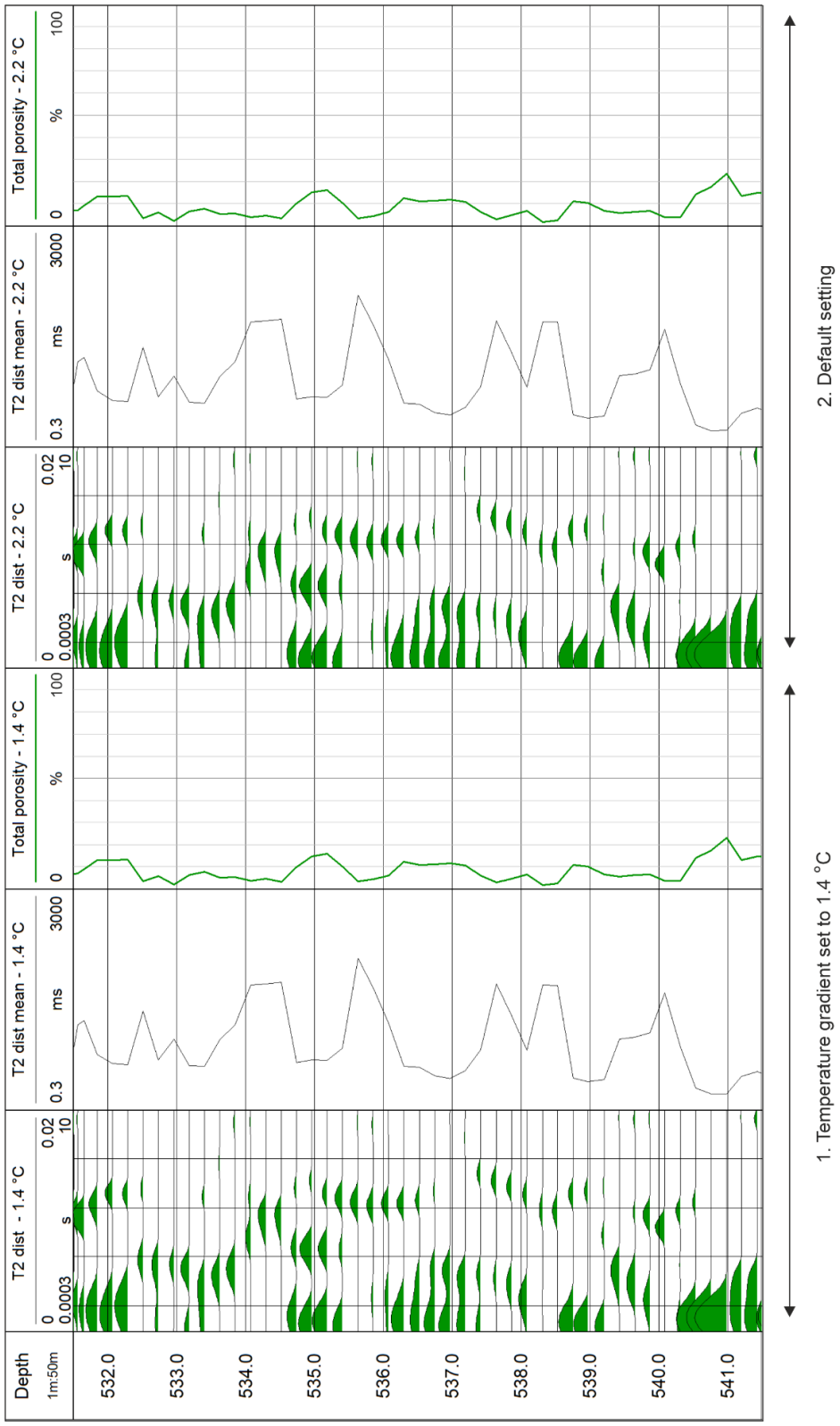

Figure 23: T_2 distribution (T2 dist) and T_2 distribution mean (T2 dist mean) and total porosity with temperature gradient values 1) 1.4 °C / 100.0 m and 2) 2.2 °C / 100.0 m (default setting). T_2 distribution log has two scales: top one is amplitude in meters and bottom one is relaxation time in seconds. Other processing parameters were kept at default settings.

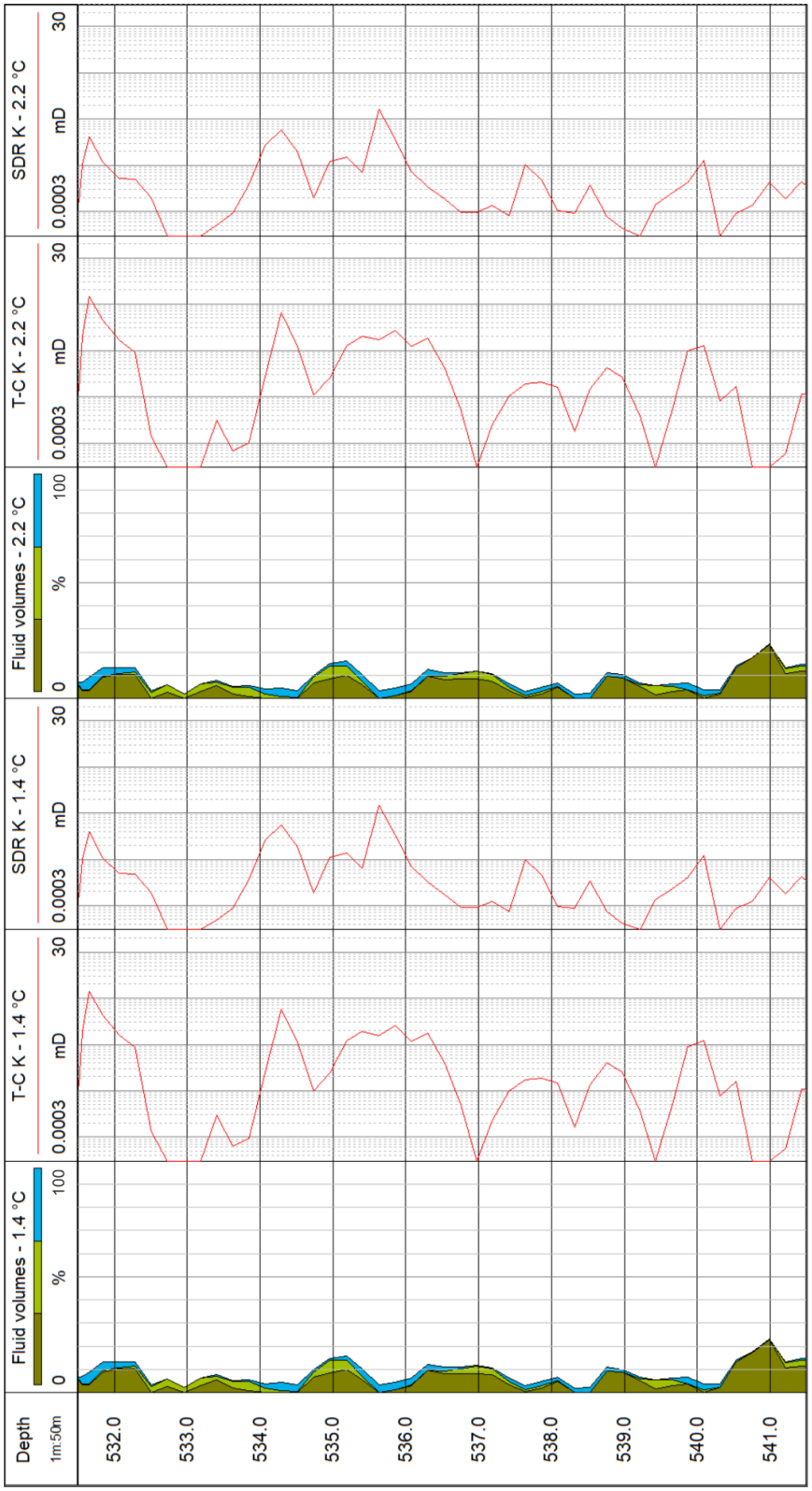

Figure 24: Fluid volumes (dark green is clay bound water, light green is capillary bound water and blue is moveable water), Timur-Coates (T-C) and Schlumberger-Doll (SDR) permeabilities with temperature gradient (GRAD) values 1) 1.4 °C / 100.0 m and 2) 2.2 °C / 100.0 m (default setting). Other processing parameters were kept at default settings.

5.1.4. Cutoff values

To separate clay bound water, capillary bound water and moveable water, three cutoff values can be adjusted (Section 3.5.1. in Theoretical background). The default values, suitable for sandstones, are 0.003 s for cutoff 1 (clay bound water), 0.033 s for cutoff 2 (capillary bound water) and 5 s for cutoff 3 (moveable water) (Table 3) (discussed more in Section 3.5.1.). These values are approximately correct to separate the clay bound water from capillary bound water, the bound water from the moveable water and moveable water from noise. These were set in preliminary processing by a single value for the whole log, but later adjusted and cut to desired sections in the NMR Workspace for more detailed assessment.

The cutoff values are essential in estimating total porosity, fluid volumes and permeability (Section 3.5.1. in Theoretical background). Cutoff 3 has the greatest effect; it separates signal from noise, i.e. which part of the T_2 distribution will be utilized for total porosity, fluid volume and permeability estimates. Cutoff 2 separates the bound water volume from moveable water, which is important when assessing moveable groundwater and estimating T-C permeability, which is dependent on the ratio of moveable water volume to bound water volume (Equation 3.19). Cutoff 1 divides the bound water volume to capillary and clay bound water but does not have an effect on total porosity and permeability calculations.

Different cutoff values were tested to determine the water volumes and to separate the signal from the noise. The cutoff 3 value was set to 5 s in the preliminary processing. In the NMR Workspace in was observed that lower value is more suitable, because with 5 s most of the noise remains in the T_2 distribution log. Thus, the cutoff 3 was set to 3 s in the NMR Workspace and further adjusted in more detail to cut all remaining noise. Noise can be recognized from signal with a selection of logs (Figure 25).

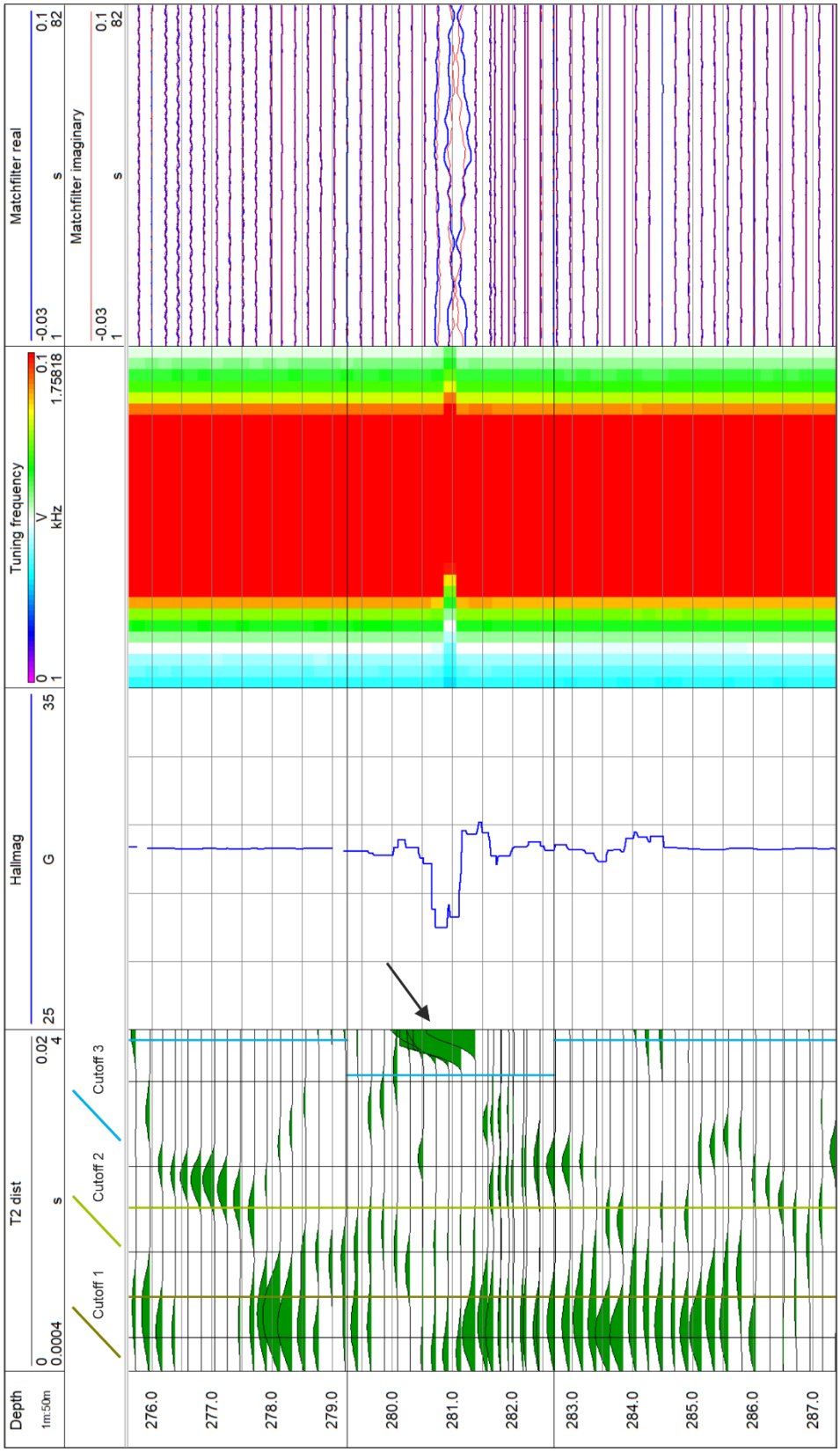

Figure 25: Adjusting cutoff 3 in NMR Workspace for T_2 distribution (T2 dist). Significant noise was encountered at depth of 280–281.5 m (marked with an arrow), which is not cut by the 3 s cutoff 3. Thus, the section 279.0–282.5 m was divided into a zone and the cutoff 3 moved to left, in a way that all the noisy T2 distribution is on the right side of the cutoff 3. Magnetic flux density (Hallmag), tuning frequency and matched filter (real and imaginary components) placed on top of each other) logs are used to recognize the noise; all three show disturbance around 280.0–281.5 m. T_2 distribution log has two scales: top one is amplitude in meters and bottom one is relaxation time in seconds.

The following criteria were used for recognizing noise from the data. The signal was decided to be noise if

1. If two or more of the hallmag, tuning frequency and matchfilter logs had disturbance
2. If the hallmag log had significant (over 3 G) disturbance
3. At uncertain locations, the data was compared to other available drillhole logs showing fractures (acoustic and optical televiewer images, core logging results) to ensure that the signal is coming from fracturing

Cutoff 3 was not touched if there was no data to suggest the presence of noise.

Hallmag log represents magnetic flux density, which alters easily if some magnetic material is present. Tuning frequency is the tuned frequency of the BMR tool; the relevant transmission frequency is its most sensitive frequency range which is achieved by tuning (Coates et al. 1999, Bruker BioSpin 2014). Matchfilter log is a representation of the average of the first 600 echoes (personal communication with Benjamin Birt 24.11.2020). Noise can be easily recognized when real and imaginary parts cross each other due to formation effects causing phase changes.

Adjusting of cutoff 2 value was tested regarding to the calculation of permeability. The default value set in the preliminary processing was 0.033 s, which was shifted to 0.01 s in the NMR Workspace. Cutoff 2 should be placed in between two peaks of the T_2 distribution, but due to the heterogeneity of the distribution, placing the cutoff is hard and multiple positions can be considered. On average, 0.01 s seemed to fit slightly better between the two peaks, though at some locations 0.033 s was better. The effect on permeability is discussed more in Section 5.3.

Necessity of cutoff 1 value was considered by comparing the fluid volume data to core logging results. Bedrock of Olkiluoto does not generally have clay minerals, but they may occur as fracture fillings. When logging the core, fracture filling minerals are recognized,

and thickness of the filling is estimated by accuracy of 0.1 mm (Toropainen 2012). It was observed that in fractures with distinctive mineral filling (over 10 mm), the fluid volume data shows big amount of clay bound water. However, the amount of clay bound water is equally high also in locations where fracture fillings have been documented to be minor or absent. This may lead to misinterpretation when defining fractures, if the filled fractures are not studied by other methods. Regarding to permeability estimates, the cutoff 1 does not have an effect; SDR permeability is calculated based on the geometric mean of the T_2 distribution (Equation 3.17) and T-C permeability is based on the ratio of the whole bound fluid volume to the free fluid volume (Equation 3.19, Figure 7). These remain the same despite the position of cutoff 1. Because of the minor effect and benefits of cutoff 1, the value was not systematically adjusted but kept at 0.003 s.

5.2. Porosity estimates

Determining total porosity is based on the T_2 distribution. Thus, the chosen cutoff 3 value has a substantial effect on the porosity values; it determines which part of the signal is taken into account to determine the porosity. This is seen in Figure 26; the more signal is cut with the cutoff 3, the lower is the total porosity.

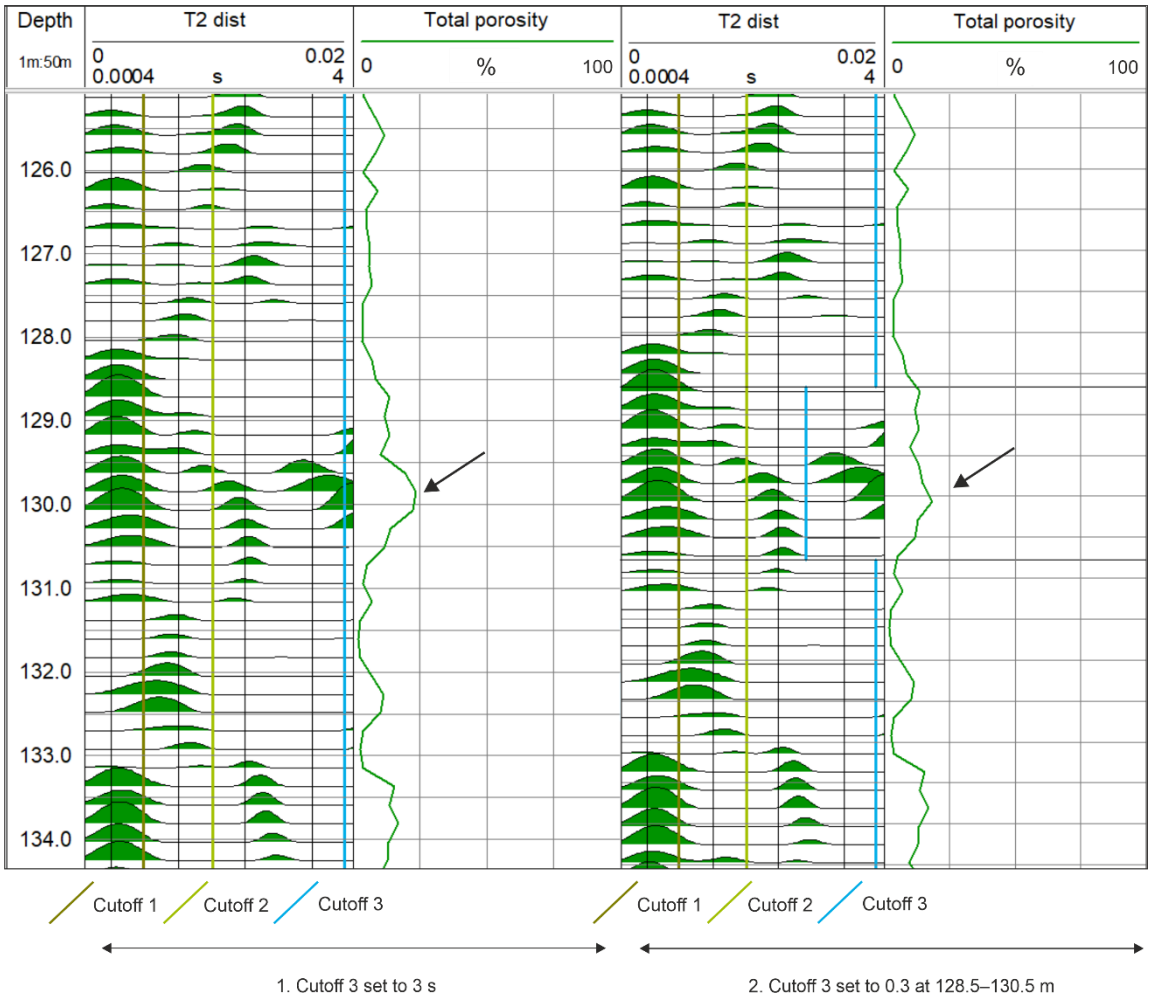

Figure 26: T_2 distribution (T2 dist) and total porosity with two different cutoff 3 values at depth of 128.5–130.5 m. On the left side, T2 dist and total porosity have cutoff 3 value of 3 s. On the right side, T2 dist has been divided into a section and the cutoff 3 moved to 0.3 s. With cutoff 3 value 0.3 s, total porosity is smaller (marked with an arrow). T_2 distribution log has two scales: top one is amplitude in meters and bottom one is relaxation time in seconds.

Overall, porosity in the gneissic bedrock of Olkiluoto is low, around 0.1–8 % (Siitari-Kauppi et al. 2010, Ikonen et al. 2015) and the highest porosity values result from fracture zones. Ikonen et al. (2015) determined average porosity from three drillholes, which derived an average value of 1.07 %. In the BMR data, porosity in OL-KR56 varies between 0.1 and 20 % with an average of 10.3 % and standard deviation of 0.12. However, OL-KR56 is cut by multiple brittle fault zones, which increase the total porosity with fracturing. In reasonably intact bedrock, with only minor fracturing, BMR derives smaller porosity values; for example at 200.0–300.0 m, total porosity gives an average of 8.4 % and at 460.0–470.0 m, 6.2 %.

5.2.1. Porosity and lithology comparison

Porosity does not show clear dependency on lithology. In Figure 27, at depth of 291.8 m, porosity shows a sharp change at lithological contact. However, for the most part porosity does not vary among lithologies and, high porosity results from fractures. In Figure 27, porosity changes at some lithological contacts, e.g. at 288.5 and 291.8 m (marked with arrows in Figure 27). The high porosity peaks are due to fractures (10.0 to 20.0 % porosity), but otherwise porosity remains low (3.0 to 7.0 %).

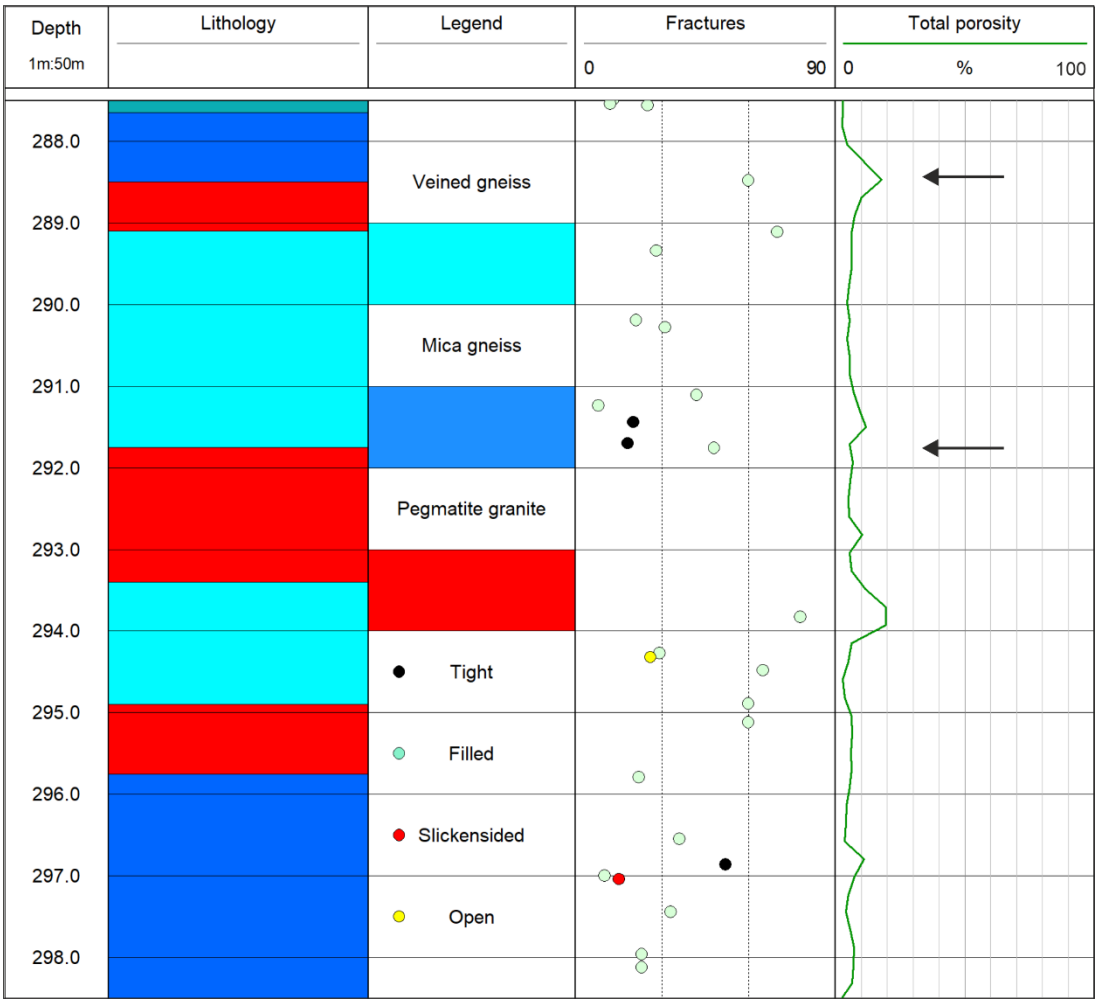

Figure 27: Lithology, fractures observed in the core logging and total porosity at depth of 288–298 m. At 288.5 and 291.8 m, total porosity changes at lithological contact (marked with arrows). Legend has lithological units and fracture types. Filled fracture has fracture filling minerals, tight fracture has no filling minerals, slickensided fracture has a slickenside surface indicating movement of fracture surfaces and open fracture has a large aperture with minor filling minerals. In the fracture log, scale 0 to 90 is dip of the fracture.

Average total porosities were calculated for all lithological units found from OL-KR56 (Table 5) (see also lithological log for the whole drillhole in Appendix B). K-feldspar

porphyry and tonalitic granodioritic granite gneiss have the most distinctive porosities; K-felspar porphyry has the lowest with 3.6 % and tonalitic granodioritic granite gneiss the highest with 11.0 %. However, both are found only as short sections in OL-KR56: K-feldspar porphyry at 202.5–206.7 m and tonalitic granodioritic granite gneiss at 304.3–306.1, 308.2–310.5, 311.7–318.4 and 369.5–374.0 m. Other lithological units have porosities of 8.0±1 %.

Table 5: Average total porosities for lithological units in OL-KR56.

Lithological unit	**Average total porosity (%)**
Diatexitic gneiss	8.3
K-feldspar porphyry	3.6
Mafic gneiss	7.7
Pegmatite granite	8.6
Quartz gneiss	8.5
Tonalitic granodioritic granite gneiss	11.0
Veined gneiss	8.7

5.2.2. Porosity and seismic velocities comparison

Total porosity derived from the T_2 distribution was compared to seismic velocity logs (Figure 28). Porosity is one of the most significant factor affecting seismic velocities. Seismic velocities have been observed to have almost linear dependency on porosity (e.g. Vernik and Nur 1992); when porosity increases, both P- and S-wave velocities decrease. This is because seismic waves do not propagate that efficiently in fluids compared to solids.

The seismic velocity logs included P- and S-wave velocities and full waveform logs. P-wave velocity varies between 3500–6500 m s^{-1} and S-wave velocity 2700–4000 m s^{-1}. Poisson's ratio log was calculated from the P- and S-wave velocities, receiving values -0.16–0.4. The logs from section 420.0–450.0 m are shown in Figure 28.

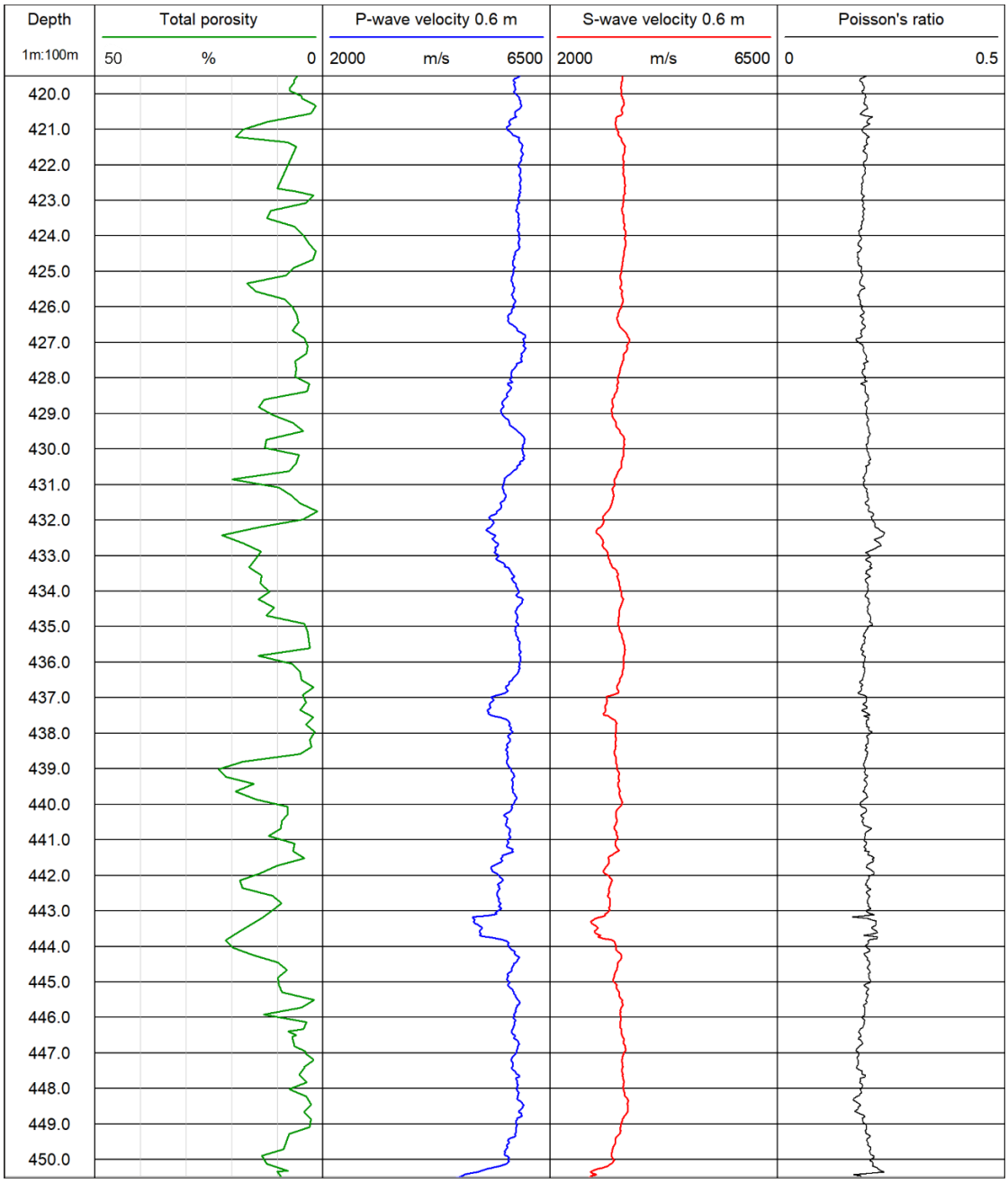

Figure 28: Total porosity (note reversed scale, low values on the right side), P-wave velocity, S-wave velocity and Poisson's ratio with 0.6 m transmitter-receiver interval at depth of 420.0–450.0 m.

Generally, the velocity logs follow the total porosity log rather well. Especially the fractured zones are visible in both as low seismic velocities and high porosity (in Figure 28, e.g. at depth of 443.0–444.0 m). In intact bedrock, the total porosity log shows more variation but has small values (e.g. lower than 10 % in the section 209.0–214.0 m). Poisson's ratio log shows the greatest anomalies in fractured zones, but otherwise remains around 0.2. However, often the seismic velocities and porosity logs show difference in depth; the

high porosity and low seismic velocities have similar series of peaks, but they have difference in depth from 1.0 m to 5.0 m. Additional depth correction was tested to correct the difference; porosity log was moved to match the P-wave velocity log. The depth correction was not systematic, because the porosity log had to be moved both up and down with irregular intervals. With this procedure, the most significant peaks matched in depth.

Depth interval 420.0–450.0 m was utilized for assessing the porosity and seismic velocity comparison in more detail (the logs from this interval are shown in Figure 28). This depth interval shows a reasonably good match between porosity and seismic velocities already without the depth correction. Porosity and P-wave velocity were plotted on a cross plot with and without the depth correction for the whole log and for the 420.0–450.0 m interval.

Figures 29 and 30 have the porosity vs P-wave velocity for the whole log, Figure 29 without the additional depth correction and Figure 30 with the additional depth correction. In both figures, most of the velocities are concentrated between 5500–6200 m s^{-1} and porosities between 0–20.0 %. Figure 29 shows slight decrease of seismic velocity as porosity increases, which is seen as small negative slope of the trend line. In Figure 30, with the depth correction, P-wave velocity shows greater dependency on porosity; slope of the trend line is steeper. The additional depth correction does not provide remarkable differences to the porosity vs P-wave velocity comparison; the data points have moved only slightly closer to each other. No clear dependency on lithology is visible.

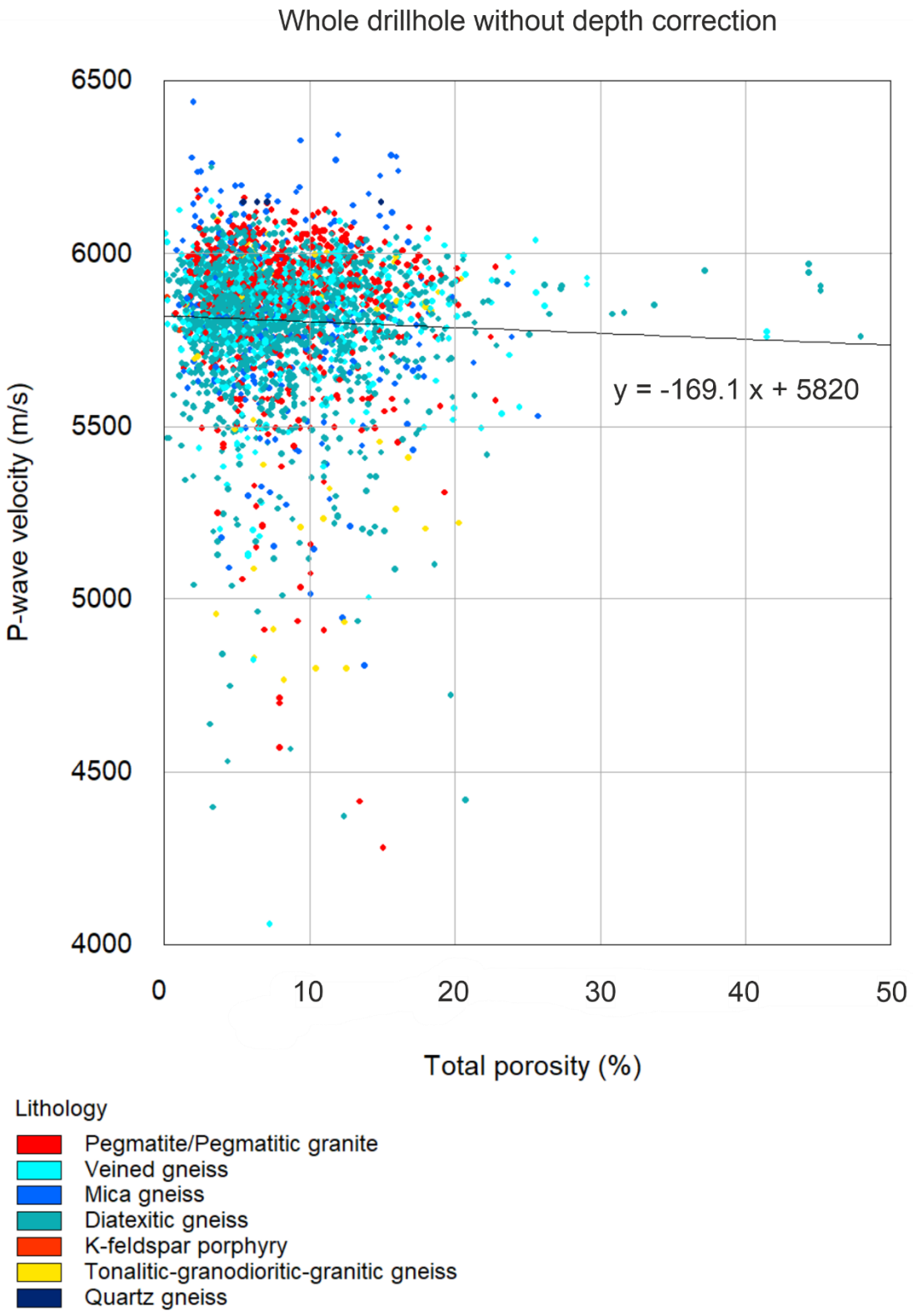

Figure 29: Porosity vs P-wave velocity for the whole log without additional depth correction. Colors represent lithology at the specific depth.

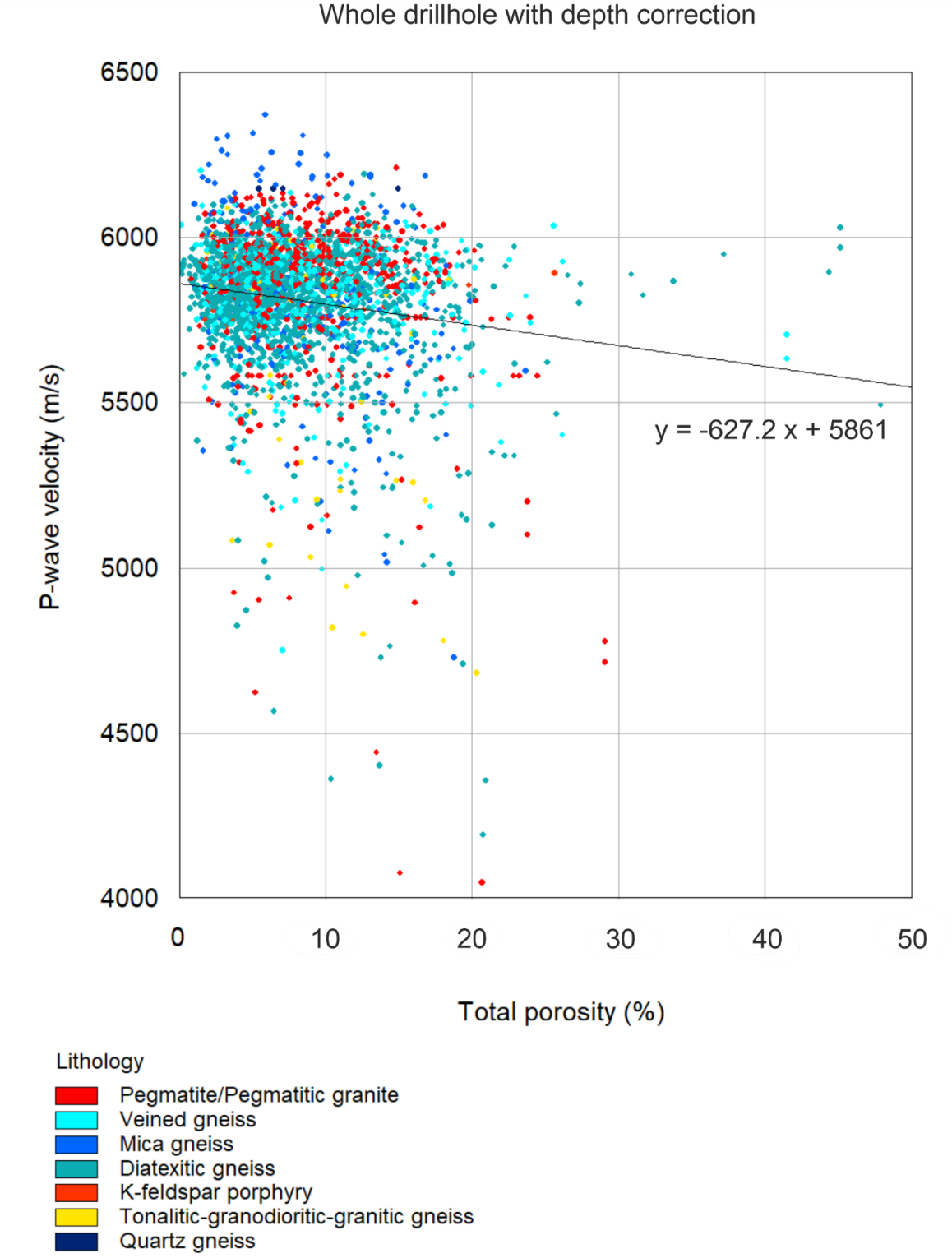

Figure 30: Porosity vs P-wave velocity for the whole log with additional depth correction. Colors represent lithology at the specific depth.

Figure 31 has the 420.0–450.0 m section without depth correction and Figure 32 with depth correction. Figures 31 and 32 both show comparison between P-wave velocity and porosity between 420.0–450.0 m. Most values drop between 5000–6000 m s^{-1} in P-wave velocity and 0–23.0 % in porosity. With the additional depth correction, some of the low-velocity data points are closer to each other. Values resulting from veined gneiss drop mostly on the upper side of the trend line. Compared to the whole log (Figures 29 and 30), 420.0–450.0 m (Figures 31 and 32) shows stronger dependency between porosity and P-wave velocity; slope of the trend line is steeper.

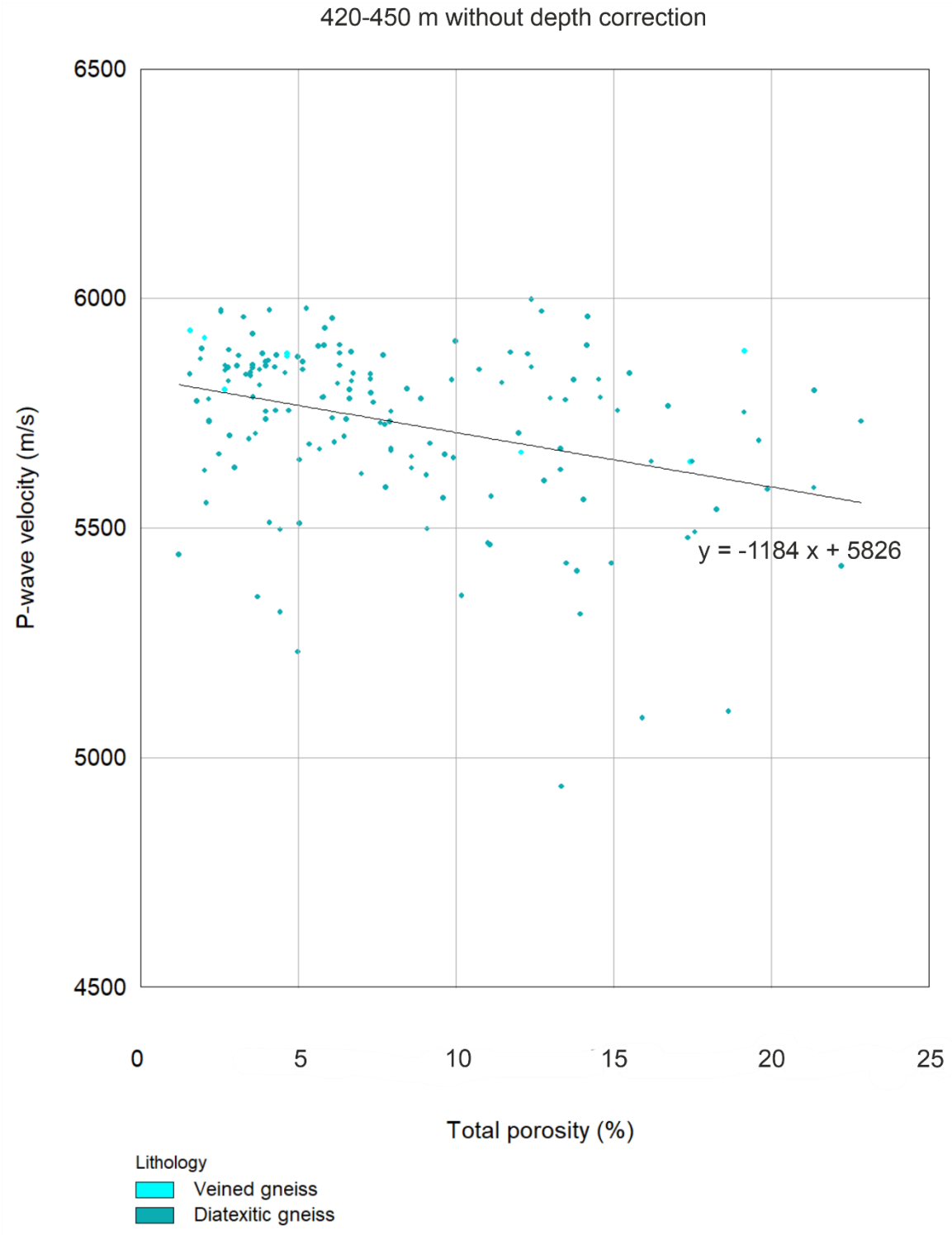

Figure 31: Porosity vs P-wave velocity at depth of 420.0–450.0 m without depth correction. Colors represent lithology at the specific depth.

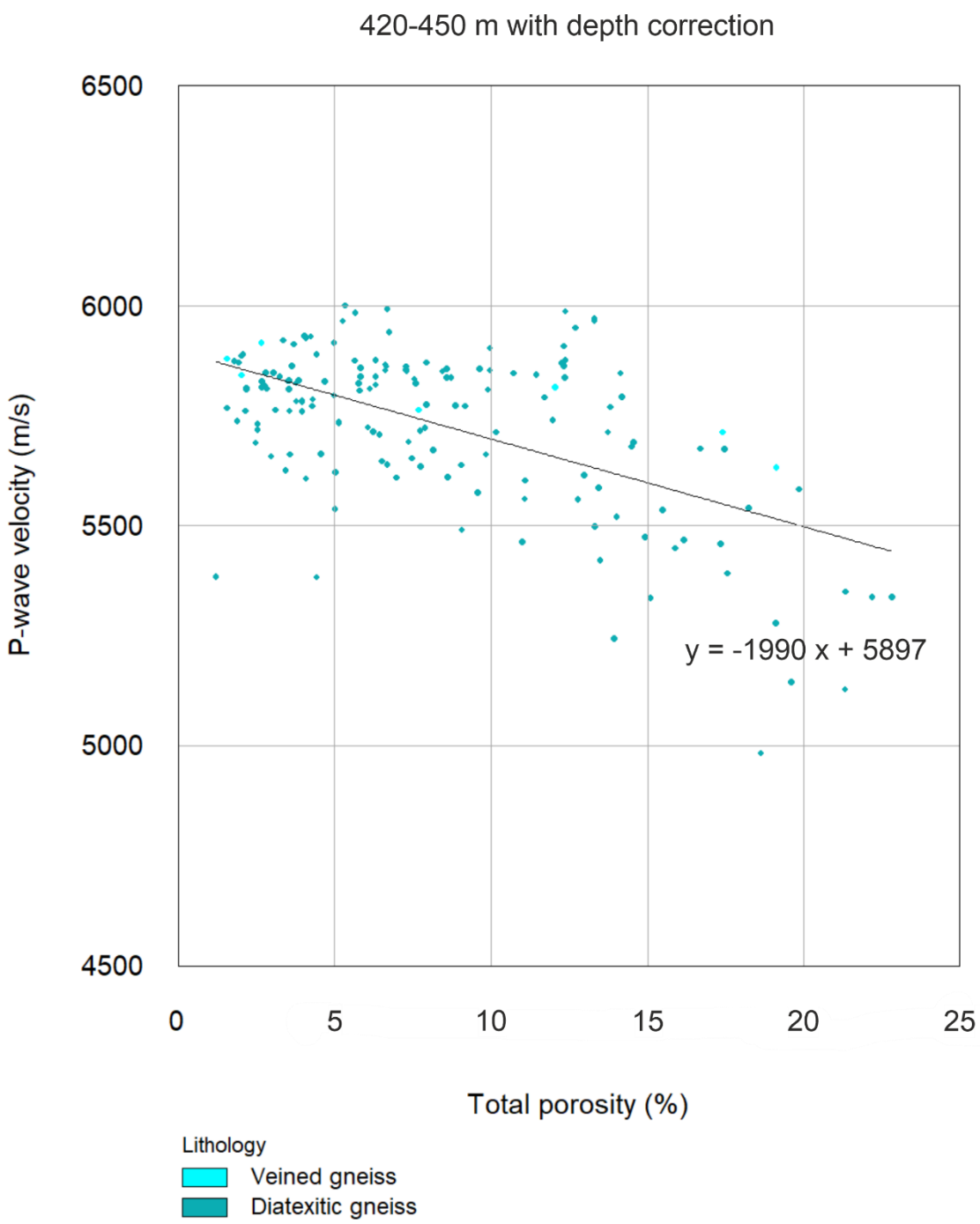

Figure 32: Porosity vs P-wave velocity at depth of 420.0–450.0 m with additional depth correction. Colors represent lithology at the specific depth.

5.3. Permeabilities, comparison and calibration

SDR and T-C permeabilities are estimated from the BMR data based on the Equations 3.17 and 3.19. T-C permeability is dependent on total porosity, free fluid volume to bound fluid volume ratio and constant *C* (Equation 3.19). SDR permeability is dependent on total porosity, geometric mean of the T_2 distribution and constant *a* (Equation 3.17). SDR permability has been considered to be more suitable for crystalline bedrock, as discussed in Section 3.5.3. The permeability values were converted to hydraulic conductivity according to Equation 3.21 and temperature dependency of water viscosity was taken into account with Equation 3.22.

Generally, the permeabilities show a lot of variation. SDR permeability is plotted against depth in Figure 33. For this, four excessive permeability values (20–30 mD) were removed from depths 595.8, 596.0, 373.1 and 634.5 m for more presentable plot. Despite the significant variations, SDR permeability detects intersection of HZL11 at 122.7–124.7 m and HZ146 at 339.6–385.8 m (discussed in Sections 2.4. and 4.2.1.).

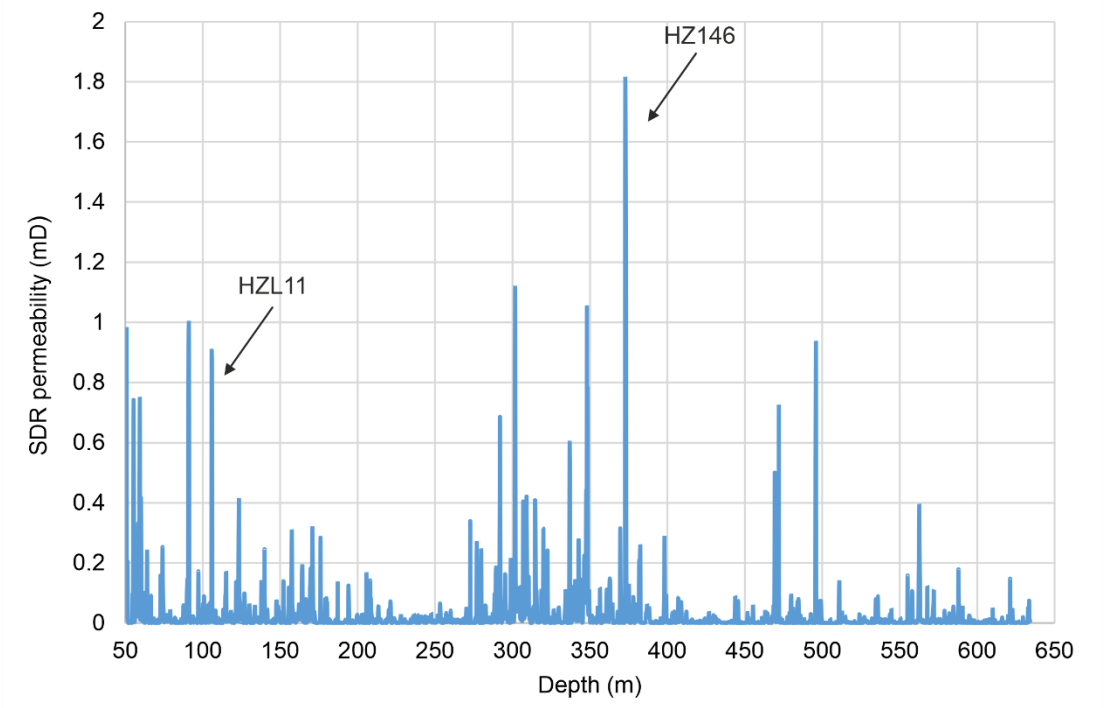

Figure 33: Depth vs SDR permeability. Intersections of HZL11 at 122.7–124.7 m and HZ146 at 339.6–385.8 m are seen as higher permeabilities.

5.3.1 Comparison to HTU hydraulic conductivity data

The hydraulic conductivity values were compared to the hydraulic conductivity data from the HTU measurements (Section 4.2.2.). HTU measurement was performed with 2.0 m packer spacing, i.e. the resulting value represents hydraulic conductivity from the whole 2.0 m section, which often includes both intact rock and fractures (discussed more in Section 4.2.2.). BMR calculates permeability value continuously, approximately every14 cm (discussed more in Section 4.1.1.).

The following procedure was conducted to make the HTU hydraulic conductivity and BMR permeability comparable:

1. BMR's SDR and T-C permeabilities were converted into hydraulic conductivity according to Equations 3.21 and 3.22.

2. BMR hydraulic conductivity values were split into 2.0 m sections corresponding the HTU packer spacing.

3. Maximum value of BMR-based hydraulic conductivity was chosen from each section to be compared to HTU. It was decided to use the HTU hydraulic conductivity values interpreted with the stationary state Moye formula (discussed in Section 4.2.2.), because 1/Q and Horner formulas do not calculate hydraulic conductivity at locations, where transient state is not reached for the flow.

To test the suitability of the T-C permeability model, cutoff 2 was shifted. Cutoff 2 was shifted from the default 0.033 s to 0.01 s, which seemed to locate better between the T_2 distribution peaks. However, the T_2 distribution is overall very heterogeneous and difficult to interpret; it does not show clear trends and number of the peaks varies.

It was observed that generally the hydraulic conductivity values estimated from the BMR permeability models fall into the same range with the HTU values, between 10^{-12}– 10^{-8} ms^{-1}. From the two permeability models, the SDR model showed more similarities with the HTU data. With the default constants, the SDR model succeeded in estimating the hydraulic conductivity to be the same or one tenth smaller than the hydraulic conductivity determined with the HTU. The T-C model showed more variation compared

to HTU results (10^{-15} – 10^{-7} ms^{-1}) and the shift of cutoff 2 did not improve the results. Thus, the hydraulic conductivity values from the SDR model were assessed in more detail. The maximum value from the SDR model from the 2.0 m section corresponding the HTU packer spacing was plotted on a cross plot against the HTU hydraulic conductivity values. The plot is shown Figure 34.

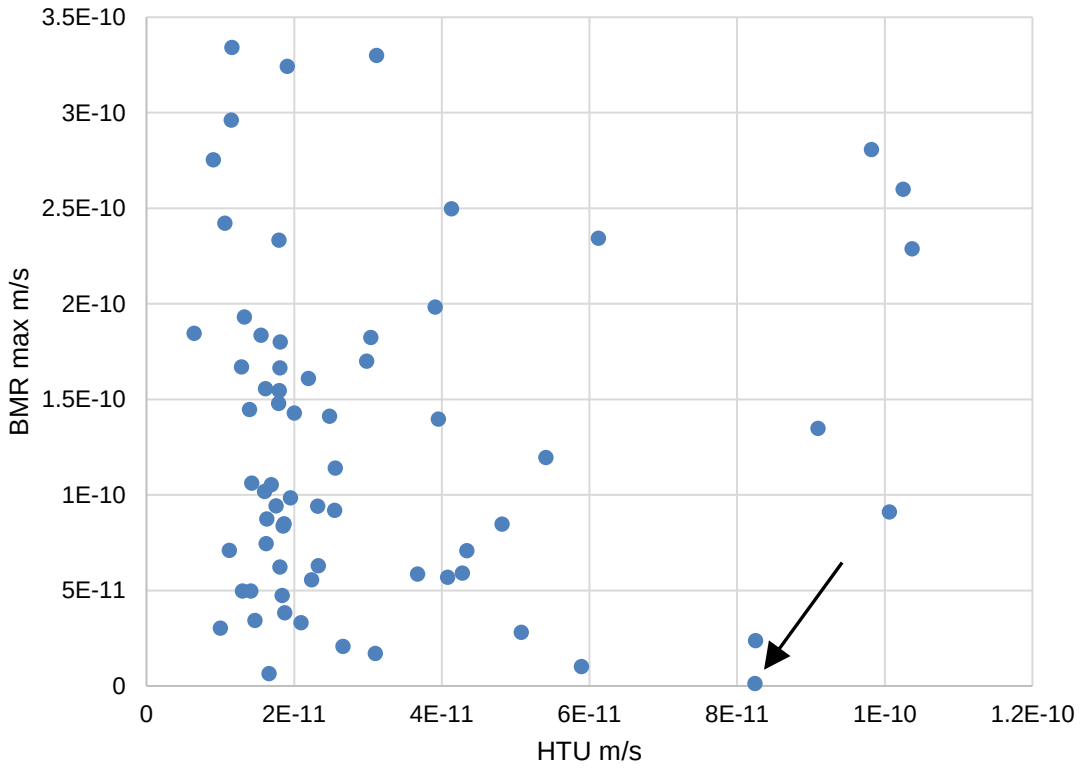

Figure 34: Hydraulic conductivity values from Hydraulic Testing Unit (HTU) vs maximum hydraulic conductivity values from Borehole Magnetic Resonance (BMR) in m s^{-1}. Erroneous signal coming from depth 505.3 m marked with an arrow.

Figure 34 does not show a clear trend between the hydraulic conductivities of HTU and BMR. Most of the values are on the order of 10^{-11} m s^{-1} and at some depths high values are received from one tool while low values from the other. This mismatch probably results from the depth difference between HTU and BMR.HTU has a 2.0 m error limit because of the 2.0 m packer spacing, which means that the real signal (leaking fracture) may come as far as 2.0 m away. . Often the detected hydraulic conductivity from HTU is at slightly different depth from the one detected from BMR. This can be seen in Figure 34, which points out one of the most outstanding errors; at depth of 505.3 m, BMR detects high hydraulic conductivity while HTU detects the same signal 0.7 m lower, where BMR

no longer detects high value. The erroneous signal is marked in the plot in Figure 34 and the location on the logs in Figure 35.

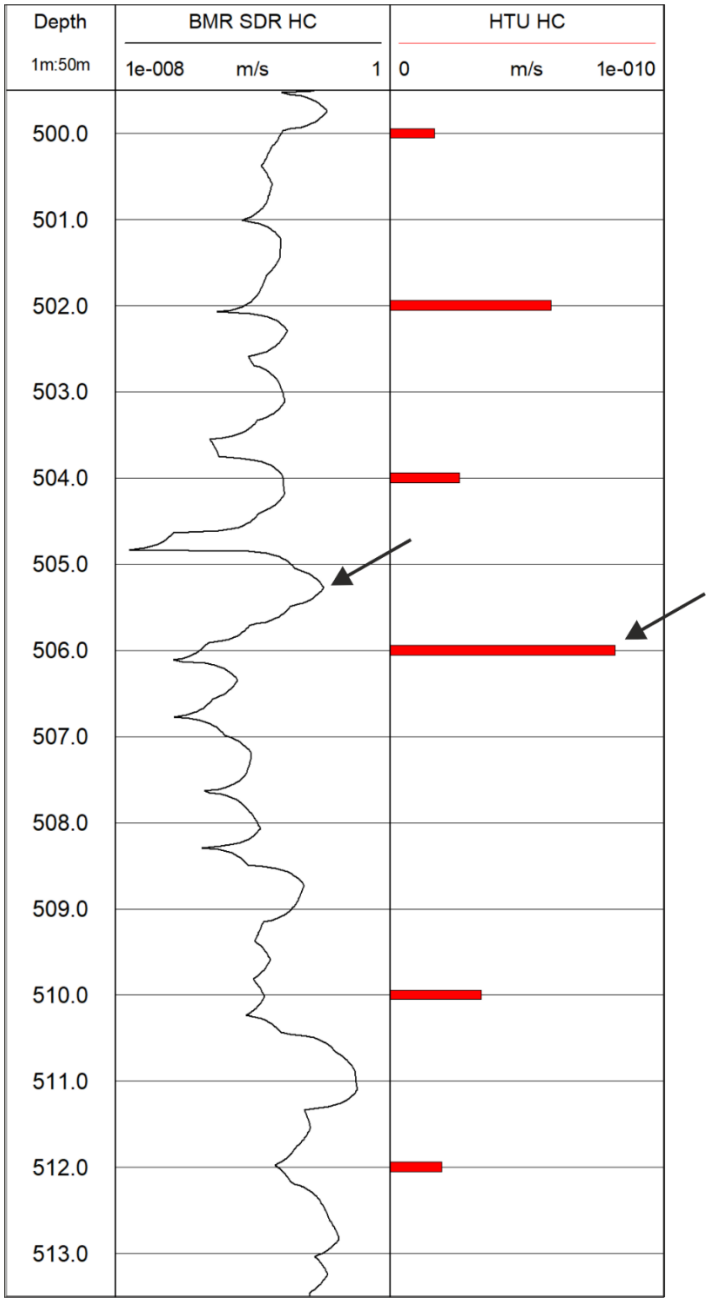

Figure 35: Hydraulic conductivity derived from BMR with Schlumberger-Doll-Research model (K SDR) and hydraulic conductivity measured with Hydraulic Testing Unit (HTU) with Moye model at depth of 500.0–513.0 m. Arrows point out high signal, which should be located at the depth. Due to HTU error limits, they differ by 0.7 m.

5.3.2. Comparison to PFL data

The BMR permeability values were also compared to the transmissivity data from the PFL measurements (Section 4.2.2.). PFL differs from BMR significantly; BMR measures only the first 1.0 cm from the drillhole wall continuously, passing both intact bedrock and fractures (Section 4.1.1.). PFL measures only water conducting fractures; it has flow sensors, which detect the flow and its direction (discussed more in Section 4.2.2.). Because PFL gives a reading only when it passes water conducting fractures, the measurement results are stepped. BMR, on the other hand, measures T_2 distribution and thus permeability continuously. Also, PFL does not derive water conductivity with same variables as BMR. PFL derives fresh water head as mL/h and transmissivity as $m^{-2}s$ (Table 2) and BMR permeability in Darcy's, which can be converted to hydraulic conductivity ($m\ s^{-1}$).

Personal communication with Antti Poteri on 26.10.2020 suggested that the BMR permeability can be made convertible with PFL transmissivity with the following procedure:

1. Changing permeability's unit Darcy into square meters

2. Converting the permeability into hydraulic conductivity according to Equations 3.21 and 3.22.

3. Multiplying the hydraulic conductivity with BMR's measurement spacing, which in this case is the vertical resolution of the BMR tool. Vertical resolution is approximately 14 cm (see Section 4.1.1.), but for more precise approach, it was calculated from the BMR data by calculating difference between lower and upper depth of the readings. After the multiplication, the BMR and PFL measurement results are in the same unit.

4. Matching the BMR transmissivity to same depth with PFL transmissivity. Because PFL gives reading only when passing water conducting fractures, it forms stepped data. Thus, the readings had to be matched with the continuous data of BMR. This was done by selecting the BMR reading approximately from the same depth where PFL gave a reading and placing the BMR readings next to the PFL readings. Then, the result was plotted as a scatter plot, which is in Figure 36.

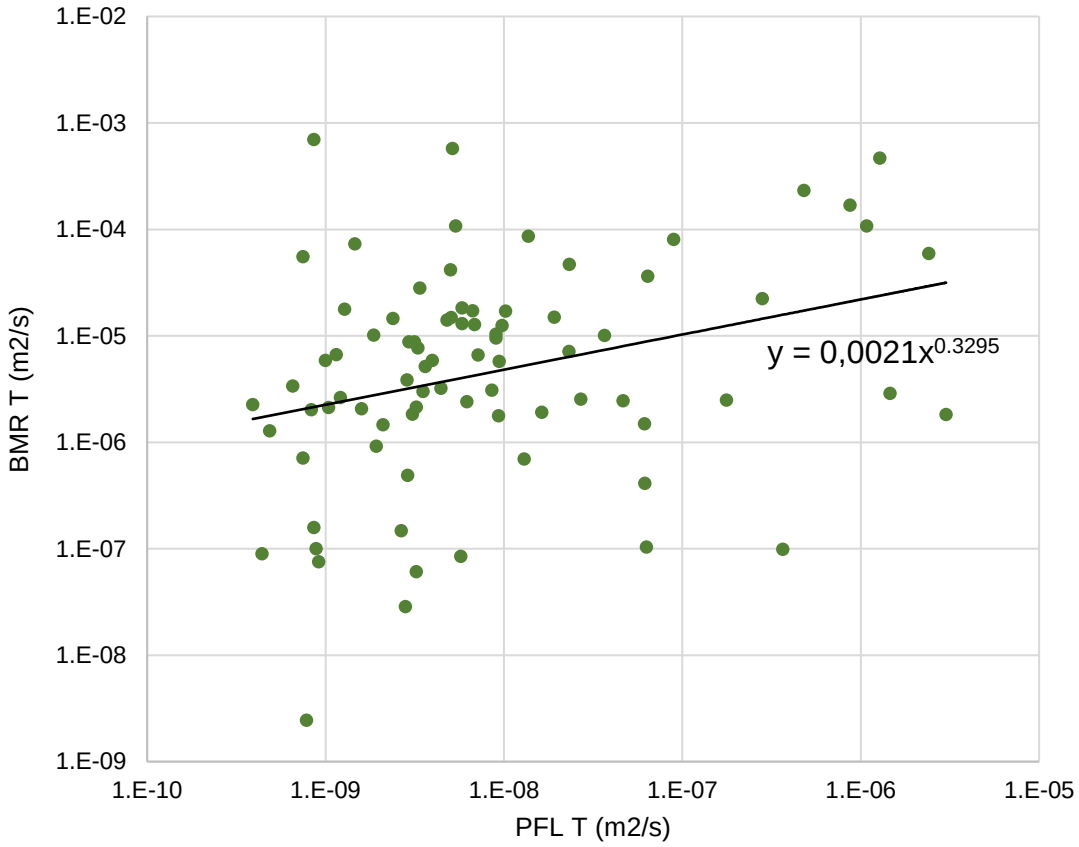

Figure 36: PFL transmissivity data from PFL vs transmissivity data from BMR in $m^{-2}s$ with a trend line. Notice the logarithmic scale.

In Figure 36, the range of the transmissivity values is similar, and the values show some linear dependency; BMR transmissivities are about two orders of magnitude higher than the PFL transmissitivites. However, some deviation exists in Figure 36. This may be caused by depth inaccuracy's; at some depths, targeting PFL to the right, water conducting fracture may been uncertain. If the PFL transmissivity has been targeted to a fracture at wrong depth, i.e. to a fracture which does not conduct water, BMR detects very low transmissivity at the same depth.

5.4. T_2 distribution comparison

5.4.1. T_2 distribution and lithology

The T_2 distribution has minor dependency on lithological variations. Figure 37 has a section of lithology, T_2 distribution and T_2 distribution mean at depth of 67.0–82.0 m. Veined gneiss has a steady T_2 distribution without any significant changes and showing some minor porosity. Mica gneiss shows more variation; the T_2 distribution shows large number of small pores at some locations and is mostly bimodal. Pegmatite granite has the most distinct T_2 distribution; it shows some porosity but does not change its position. This is reasonable, because pegmatite granite is reasonably massive and has a homogeneous structure compared to gneisses. T_2 distribution of diatexitic gneiss does not show significant change from mica gneiss; the peaks move slightly towards right and are a bit smaller but remain variable. At some lithological units, around e.g. at depths of 72.5 and 75.5 m (marked in Figure 37) the T_2 distribution shows large number of small pores, which could result from variation in porosity in different rock types. However, T_2 distribution does not show a single, typical distribution for a specific rock type. This may be due to very minor differences in the porosity between different rock types or small fractures increasing the porosity.

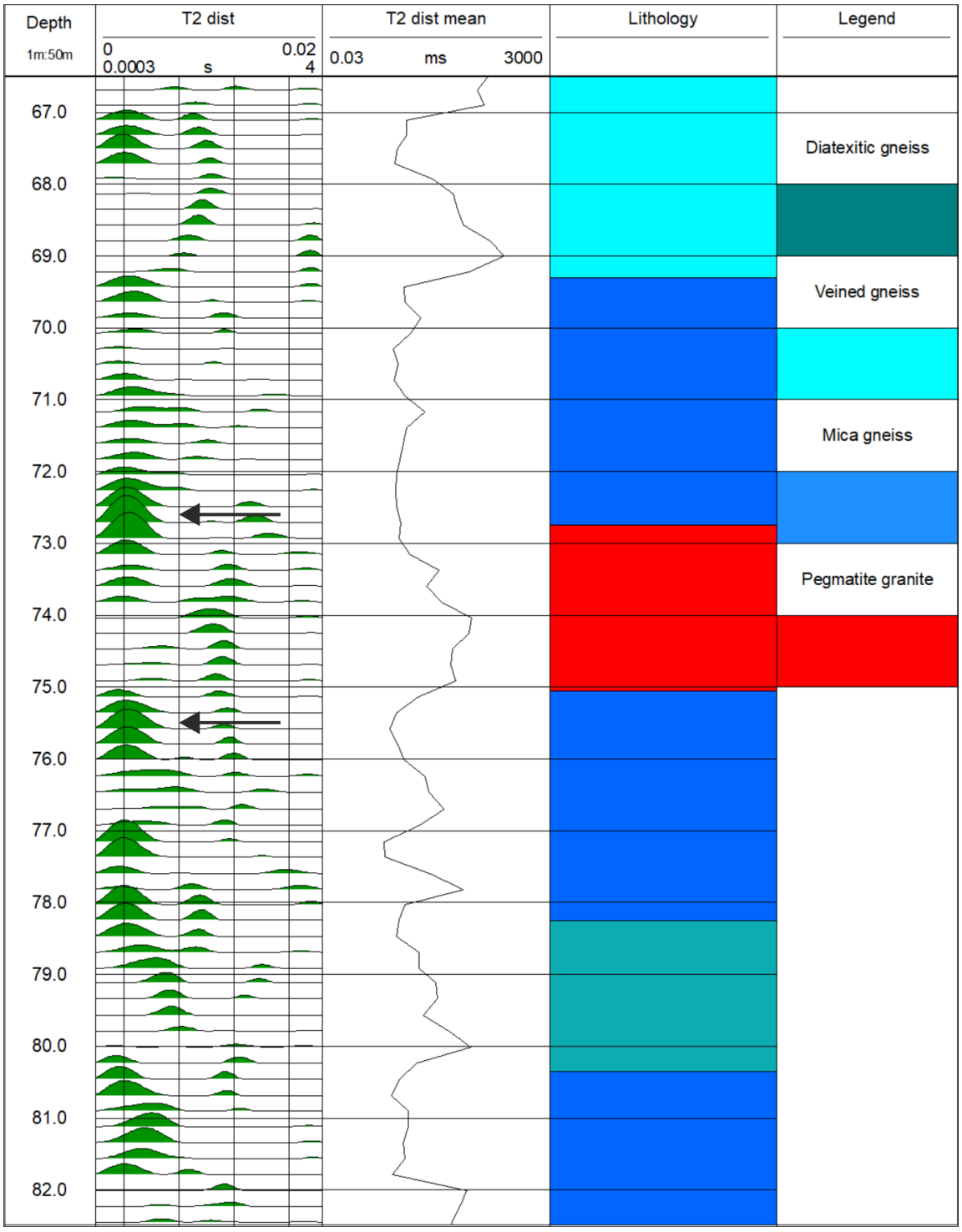

Figure 37: T_2 distribution (T2 dist), T_2 distribution mean (T2 dist mean) and lithology at depth of 67.0.–82.0 m. Mica gneiss shows large number of small pores at 72.5 and 75.5 m (marked with black arrows), which could result from increased porosity compared to pegmatite granite located in between. T_2 distribution log has two scales: top one is amplitude in meters and bottom one is relaxation time in seconds.

5.4.2. T_2 distribution and fracturing

T_2 distribution is a good indicator for fracturing. Most of the fractures observed in the core logging and acoustic and optical imaging of the drillhole are visible in the T_2 distribution as large number of small pores or small number of large pores. Especially the signal in the range of 0.1–1.0 s is most probably due to fracturing. Figure 38 has a section at depth of 168.0–174.0 m showing distinctive fracturing in the T_2 distribution, fractures observed in the core logging and in the optical and acoustic imaging. Around the depth of 170.0–172.0 m, the drillhole is highly fractured which is seen especially in the acoustic image. T_2 distribution shows large number of small pores at the depth of 170.0–171.0 m, and then small number of large pores at 171.0–172.0 m (marked in Figure 38). Around 170.0–171.0 m, core logging does not show any fractures; this is because the core sample has been flushed away when drilling (Posiva Oy and Suomen Malmi 2012 A).

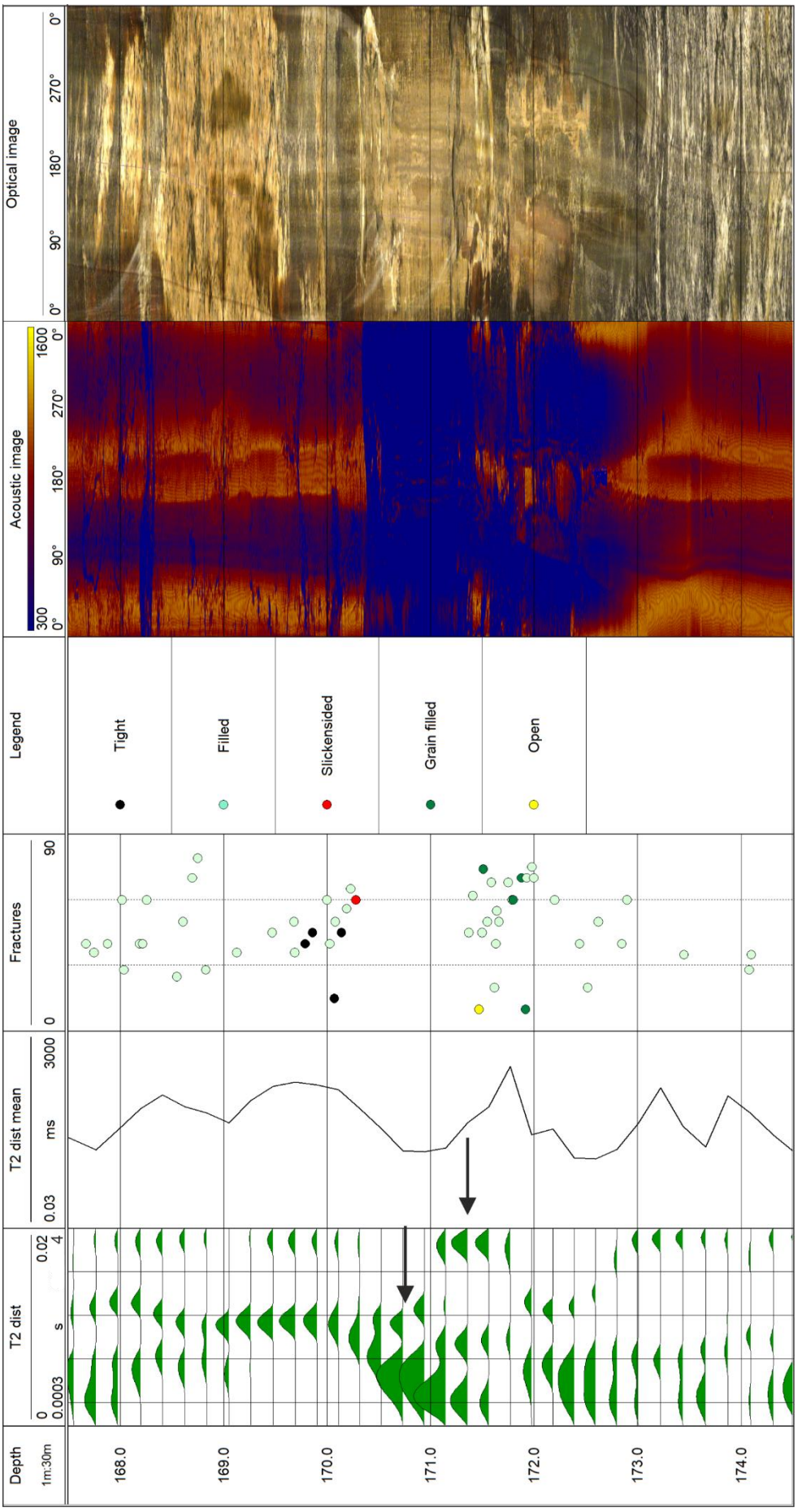

Figure 38: T_2 distribution (T2 dist) and T_2 distribution mean (T2 dist mean), fractures observed in core logging, optical and acoustic images at depth of 168.0–174.0 m. T_2 distribution shows large number of small pores at 170.0–171.0 m, and then small number of large pores at 171.0–172.0 m (marked with black arrows). T_2 distribution log has two scales: top one is amplitude in meters and bottom one is relaxation time in seconds. In the fracture log, scale 0 to 90 is dip of the fracture.

6. DISCUSSION

6.1. Earlier NMR studies in sedimentary and hard rock environments

Drillhole NMR has been used in sedimentary rock environments especially for oil and gas exploration, but NMR logging studies in hard rock environments have been lacking. NMRSA's BMR tool is one of the first drillhole NMR tools, which is suitable for hard rock environments, as it is small enough to fit into narrow drillholes. However, experience in NMR logging in hard rock environments is lacking.

NMR data processing has been calibrated to sedimentary rock environments, where rocks are more homogeneous and porous compared to crystalline bedrock. Data processing includes calculation of permeability, which is based on permeability models designed for sedimentary rocks (Equations 3.17 and 3.19). The permeability models have been an objective of research also in sedimentary environments (e.g. Dlubac et al. 2013), because they include multiple adjustable coefficients which have to be calibrated to fit the particular measured rock type. Accuracy and need of calibration was a point of interest in the Dlubac et al. (2013) study. They observed, that if high accuracy of permeability values is needed, the models have to calibrated for groundwater logging purposes.

Use of NMR logging in hard rock environments requires testing the method and calibrating the data processing. Use of the same processing workflow and calculation models as in sedimentary environments have to tested and carefully considered, because crystalline and sedimentary bedrock differ significantly. Calibration of the permeability models can be done by comparing to other permeability logs obtained with other methods or by laboratory measurements.

6.2. Data processing workflow in WellCAD

6.2.1. Preliminary processing in NMRSA Post Processing module

BMR data processing in WellCAD begins with preliminary processing in NMRSA Post Processing module. As discussed in Section 5.1., the module allows the user to modify multiple processing parameters to adjust them to fit the current environment. However, only few of them proved to be beneficial to change: moving averages, temperature gradient and the cutoff values. Other parameters did not show changes in the processed data. However, the cutoff values were assessed and tested in more detail in NMR Workspace.

6.2.2. Detailed processing in NMR Workspace

The next stage is to move the preliminary processed logs to NMR Workspace. In the workspace, the cutoff values are adjusted in more detail. The workspace proved to be useful for recognizing noisy parts of the data and removing them. BMR derives multiple logs, which can be used for noise recognition, and placing them side by side next to the T_2 distribution log provides an easy layout for noise assessment. However, noise recognition has to be done carefully with specified criteria comparing the logs to other drillhole data (a list of criteria is determined in Section 5.1.4.). The third criteria on the list, comparing the BMR data to other drillhole logs, was found extremely important at locations where both real data and noise coexisted. Some anomalies in the BMR data were recognized as real data only by comparing the data to other logs showing fractures from OL-KR56 (acoustic and optical televiewer images, core logging results). Without the other logs, the anomalies would have been considered as noise and neglected. This would cause major misinterpretation. This suggests that BMR may need other, supportive logs for careful noise recognition. Cutoff 1 could possibly be utilized for recognizing thick clay mineral fracture fillings (as discussed in Section 5.1.4.), as it may show high amount of clay bound water when encountering clay minerals. However, this would require further, more detailed study and assessment of cutoff 1 to locate it correctly.

6.2.3. Suitability of the permeability models

Two widely used permeability models are the SDR model (Equation 3.17) and T-C model (Equation 3.19). Both models were tested when making comparison to HTU measurements (discussed in the following section) and as it was predicted (see Section 3.5.3.), SDR model turned out to be more suitable for crystalline bedrock as it reached more similar values with HTU. Calibration of the T-C model was attempted by shifting cutoff 2, but because the shift did not have any improving effect on the data, no more calibration was attempted for the T-C model and only SDR model was applied when comparing to PFL.

Despite the calibration difficulties, SDR model detected water flow patterns at correct locations (see Figure 33). Observing the highly water conducting zones HZL11 and HZ146 is important for modelling hydrogeological structures in Olkiluoto, because the same zones are seen also in other drillholes. Thus, location of the final disposal facility can be directed far from water conductive structures.

6.3. Comparison to hydrogeological data

Comparison of the permeability and water content data to other hydrogeological measurement conducted in OL-KR56 proved to be challenging. In general, the measurement technique and derived parameters differ from the BMR significantly, and thus, comparison requires many data modifications. Compared to the other hydrogeological drillhole measurements conducted in Olkiluoto, BMR gives better vertical resolution, because it does not use packers; in HTU and PFL measurements, the vertical resolution is dependent essentially on the packer spacing. BMR is also faster, but as discussed in the following sections, it results as different measurement technique for flowing water.

Equations 3.21 and 3.22 were utilized in the comparisons. It was observed that Equation 3.22, that notes temperature dependency of water viscosity, has a significant effect on the conversion. In in the measurement range of BMR, 44.45–634.45 m, water viscosity changes from $5.87716 \cdot 10^{-9}$ Pa·s to $1.69156 \cdot 10^{-8}$ Pa·s according to Equation 3.22. If the

temperature dependence of the viscosity would not have been taken into account, that would have decreased the values with five orders of magnitude. Equation 3.22 has empirically determined constants A, B and C, which receive different values in different studies; according to Viswanath and Natarajan (1989), for water A is $0.02939 \cdot 10^{-3}$ Pa·s, B is 507.88 K and C is 149.3 K . Values A is $2.414 \cdot 10^{-5}$ Pa·s, B is 247.8 K, C is 140 K were provided by NMRSA. In the future, using this equation and defining its constants should be carefully considered and possibly studied further, because it may have major effect on the hydraulic conductivity results. The effect of this equation has to be considered also when interpreting the HTU and PFL comparisons; the converted results from BMR data may be too high.

6.3.1. Comparison to the HTU data

Comparison of HTU hydraulic conductivity and BMR's converted hydraulic conductivity did not show linear dependency (see Figure 34). This results essentially from differences in the observed water leakage depth; because of the HTU packer spacing, it has a 2.0 m error limit, while BMR gives a reading approximately every 14 cm. At some locations, the hydraulic conductivity peaks are at different depths (Figure 35), which results as different values.

At locations where there was no depth difference, the BMR derived often smaller values than HTU. The HTU measurement does not recognize the number of water conducting fractures inside the test section, it only gives one hydraulic conductivity value for the whole 2 m section. However, BMR detects flow separately from every fracture. When selecting the maximum value from test section, it is assumed that all hydraulic conductivity comes from that one location. It is likely, that the test section has multiple other water conducting fractures, which are not taken into account with this approach. For more precise approach, BMR hydraulic conductivity peaks from the corresponding test section could be converted into transmissivity or flow rate and summed up. This would enable calculating hydraulic conductivity coming from all the fractures within the test section and the result would be more representable.

6.3.2. Comparison to the PFL data

Comparison to PFL transmissivity showed some linear dependency (see Figure 36). However, this comparison assumes that

1. The BMR permeability comes entirely from fractures and not from the surrounding bedrock.

2. Porosity of the BMR's 1 cm measurement depth represents well also the porosity deeper in the bedrock, i.e. fractures are radially homogeneous.

BMR has a vertical resolution of approximately 14 cm; it gives a reading approximately every 14 cm (discussed more in Section 4.1.1.), which takes into account also surrounding bedrock when passing fractures, because fractures rarely have an opening of over 14 cm. However, in highly fractured or crushed zones, where the rock is broken for several meters, the vertical resolution does not have that big of an effect.

PFL has been designed to measure flow from single fractures, which can reach several meters away from the drillhole. BMR's sensitive measurement volume in crystalline bedrock is approximately 1 cm from the drillhole wall (discussed more in Section 4.1.1.), which is not enough for estimating permeability of a long fracture. This is highly unlikely in heterogeneous, gneissic bedrock of Olkiluoto.

The detected transmissivity of PFL comes almost entirely from fractures in between the packers and thus, the data is stepped. The fractures have been targeted to correct depth using SPR and core logging results, but some inaccuracy may exist; targeting to correct fractures is not always straightforward, especially in highly fractured zones. BMR collects continuous data with a vertical resolution of about 14 cm (discussed more in Section 4.1.1.), which makes comparison to PFL's stepped data challenging. The comparison was conducted by placing BMR's and PFL's logs side by side and choosing transmissivity values from corresponding depths.

Despite the challenges, Figure 36 shows some linear dependency for PFL and BMR. BMR detects approximately two orders of magnitude higher transmissivities than PFL.

This suggests that SDR model could be more representative if being multiplied by 0.01. However, precise calibration would need more certainty and use of Equation 3.22 may rise BMR's transmissivity values.

Comparison to PFL data proved more successful than comparison to HTU data; HTU comparison could not derive observable linear dependency. This is likely due to better vertical resolution of PFL than HTU; HTU has a packer spacing of 2.0 m and PFL 2.0 m and 0.5 m with targeting to fractures with SPR and core logging results. Thus, the BMR results could be more precisely targeted to corresponding depths.

6.4. T_2 distribution and porosity

6.4.1. T_2 distribution and fractures

The basis of all data produced by the NMR measurements is the T_2 distribution, or pore size distribution, which cannot be measured with any other kind of measurement tool. It describes the size and amount of pores, which correlates especially to fractures in crystalline bedrock. As observed in Section 5.4.2., fractures appear in the T_2 distribution as large pores (Figure 38). Large pores are the most typical for open fractures, but also significant amount of small pores were observed in fractured zones. Small pores may refer to presence of clay minerals (see Section 3.5.2.), if the fracture has been filled. Possibly, in Figure 38, topmost part of the fractured zone is filled later on with clay minerals and the bottom part remains open; this would explain the difference in the T_2 distribution.

In the core logging, a certain fracture type is defined for every fracture (discussed more in Section 4.2.1.). In Figure 38, at depth of 171.0–172.0 m, core logging shows open and grain filled fractures which appears as large pores in the T_2 distribution. This is reasonable, because open fractures have an opening, which can produce a signal of large pores. Grain filled fractures have a thick filling of loose, possibly clay-rich material, which can also produce a signal of large pores, because of the space in between the loosely bound grains.

6.4.2. T_2 distribution and lithology

T_2 distribution is dependent also on lithological variations. Lithological units have different porosities and thus, different amount of hydrogen producing the T_2 distribution signal. However, lithology did not show systematic comparison to the T_2 distribution (see Section 5.4.1.). The T_2 distribution changes at some lithological contacts but does not show a clear trend for each lithology. This may be due to high dependency on fracturing or due to minor changes in porosity between the lithological units. The comparison suggests, that T_2 distribution can be utilized for recognizing lithological contacts at locations where fracturing is minor and the contact is clear, but not for recognizing specific lithological units.

In crystalline bedrock, the porosity variation could rise from different grain sizes between different lithological units; bigger grain size allows more pore space between the grains (see Section 3.5.2.). However, Olkiluoto island has gone through multiple stages of deformation and metamorphosis (discussed more in Sections 2.2. and 2.3.), where the grain surfaces have been compressed tightly and no pore space has been left. This could be one reason why the lithological units do not seem to have systematic variation in T_2 distribution.

6.4.3. Porosity and seismic velocities

Porosity correlates to seismic velocities reasonably., The correlation gave a reasonable comparison to the total porosity in short sections (see Section 5.2.2.). For the whole log, the comparison was minor. This resulted essentially from depth difference problems. Some seismic velocity peaks seemed to have different depths when compared to BMR's total porosity, and the difference was not systematic. It is possible, that this results from some depth correction or depth measurement problems with either seismic velocities or BMR.

6.5. Suggestions for further study

BMR method gave promising results in Olkiluoto; data processing parameters were adjusted, some comparison to other hydrogeological measurements was found and the most significant water conducting structures were recognized. However, precise calibration of the permeability models and noise recognition and control need further study.

Calibration of the permeability models by comparing the results to other hydrogeological measurements proved to be challenging, especially due to significant differences between BMR and conventional packer test measurements. Comparison to PFL gave some linear dependency, but not enough for precise calibration. This suggests that calibration should be done by laboratory measurements of core samples and a database for the most common lithological units encountered in crystalline bedrock should be created.

T-C and SDR permeability models have been developed for sedimentary rocks, where pores are essentially in the rock matrix and the rocks are homogeneous compared to crystalline bedrock. In this study, SDR model was observed to suit crystalline bedrock better, but not perfectly; it does not take into account that almost all permeability in crystalline bedrock comes from fractures. Developing a new permeability model, more suitable for heterogeneous, fractured crystalline bedrock should be considered.

When drilling into crystalline bedrock, drillholes are not always long; for bedrock characterization purposes, they may be only tens of meters long. Data recovered from the two short ONKALO drillholes had poor signal-to-noise ratio and it could not be used in this study. This was due to environmental reasons. Some noise was encountered also deep in OL-KR56 and for recognizing it, a list of criteria was created. The criteria made the noise recognition more straightforward, but depths where both real data and noise existed were difficult to handle. However, this could be resolved with comparison to other measurements.

This study utilized only a small part of all drillhole data available from OL-KR56. Comparison to all other drillhole data was not possible within this study. Comparison of high

amount of data could be assisted with modern data mining tools, e.g. self-organizing map (Kohonen 1982, Kohonen 2001).

7. CONCLUSIONS

BMR has proved to derive successfully T_2 distribution and total porosity data from crystalline bedrock and recognize major water conducting zones. This is confirmed by comparison to fracture logging of the core, optical and acoustic images, seismic velocities and hydrogeological measurements. However, because of the noise sensitivity, the data has to be carefully interpreted and criteria created to cut off the noisy parts from the T_2 distribution data. This requires expertise from the person processing the data. The measurement environment in the ONKALO tunnel is challenging, because of high amount of magnetizing materials, which results as poor signal-to-noise ratio in short drillholes.

Deriving permeability and fluid volumes is based on calculation formulas, which could not be precisely calibrated to fit into crystalline bedrock by comparison to other hydrogeological studies. BMR differs significantly from other hydrogeological measurement tools, which makes the comparison challenging. The calibration should be conducted by calibrating the drillhole core by laboratory measurements. This would enable creating a database of different constants for different lithological units in crystalline bedrock, which could be used in the future BMR measurements. Also, creating a new permeability model for crystalline bedrock should be considered.

As such, BMR is suitable for long drillholes in crystalline bedrock for determining T_2 distribution, total porosity and recognizing water conducting zones. However, derived permeability and water content data has to be interpreted carefully; without precise calibration, the derived permeability values remain uncertain.

ACKNOWLEDGEMENTS

I have had three intelligent, supportive and educating supervisors. I deeply thank Emilia Koivisto, Minna Kuusisto and Kirsti Korkka-Niemi for your guidance. Thank you, Emilia Koivisto, for your dedication and many comments on my thesis. I also received prominent peer support and had many conversations about BMR with Salla Eeva. Thank you Salla, I hope that our cooperation continues in the future.

I would like to thank Posiva and its people for the possibility to conduct this study and letting me use high amount of their research material. I received help from multiple colleagues and had many educational conversations. I have gained valuable experience from working for Posiva during summers of my studies, which also helped me with my thesis. For this, I would like to thank especially Antti Joutsen, for recruiting me and for excellent familiarization into geology of Olkiluoto.

Thank you NMRSA, for making the BMR measurements possible in Olkiluoto. From the people of NMRSA, I would like to give special thanks to Ryan Gee, for helping me with WellCAD and data processing. WellCAD software was an essential part of my thesis. I thank ALT for providing me both basic and NMR module licences for WellCAD.

During moments of despair, I have received incredible support from my friends. I would like to thank my friends at the University and the ones who have known me since childhood. Thank you Mimmi, Elina, Noora, Katriina, Kia, Katariina, Joona, Oliver, Theo and many other for the years of studying, I hope that our friendship continues throughout the years. Thank you Noora and Emma, for always being there whenever I have needed you. Finally, I would like to thank my family. I have always been able to rely on my little sister and parents. Thank you for your advice in studying, especially in mathematics and physics, through my school years. I would not be here without you.

Bibliography

Aaltonen, I., Engström, J., Front, K., Gehör, S., Kosunen, P., Kärki, A., Mattila, J., Paananen, M. and Paulamäki, S. 2016. Geology of Olkiluoto. Posiva report 2016-16. Posiva Oy, 398 p.

Appel, M., Freeman, J.J., Perkins, R.B. and Hofman, J.P. 1999. Restricted Diffusion And Internal Field Gradients. SPWLA 40th Annual Logging Symposium Transactions. In Oslo, Norway, 30.5.–3-6.1999. Society of Petrophysicists and Well-Log Analysts, 13 p.

Bendel, P. 1990. Spin-echo attenuation by diffusion in non-uniform field gradients. Journal of Magnetic Resonance 86, 509–515.

Bloch, R. 1946. Nuclear Induction. Physical Review 70, 460–474.

Brown, R.J.S. and Gamson, B.W. 1960. Nuclear magnetism logging. Petroleum Transactions of AIME 219, 201–209.

Brownstein, K.R. and Tarr, C.E. 1979. Importance of classical diffusion in NMR studies of water in biological cells. Physical Review 19, 2446–2453.

Bruker BioSpin. 2014. AVANCE Beginners Guide, User Guide, Version 006. Bruker Corporation, Rheinstetten, 83 p.

Carman, P. C. 1956. Flow of Gases Through Porous Media. Academic press, New York, 182 p.

Carr, H.Y. and Purcell, E.M. 1954. Effects of diffusion on free precession in nuclear magnetic resonance experiments. Physical Reviews 94, 630–638.

Chabay, R. and Sherwood, B. 2011. Matter & Interactions, 3rd edition. John Wiley and Sons Inc., New Jersey, 1128 p.

Chang, D., Vinegar, H.J., Morriss, C. and Stralet, C. 1994. Effective porosity, producible fluid and permeability in carbonates from NMR logging. SPWLA 35th Annual Logging Symposium. In Tulsa, Oklahoma, USA, 19.–22.6.1994. Society of Petrophysicists and Well-Log Analysts, 21 p.

Coates, G. and Denoo, S. 1981. The producibility answer product. The Technical Review 29, 54–63.

Coates, G., Marschall, A., Mardon, D. and Galford, J. 1997, A new characterization of bulk-volume irreducible using magnetic resonance. SPWLA 38th Annual Logging Symposium Transactions. In Houston, Texas, USA, 15.-18.6.1997. Society of Petrophysicists and Well-Log Analysts, 14 p.

Coates, G.R., Xiao, L. and Prammer, M.G. 1999. NMR Logging Principles and Applications. Halliburton energy services, Houston, 234 p.

Cowan, B. P. 1997. Nuclear magnetic resonance and relaxation. Cambridge University Press, Cambridge, 434 p.

Darcy, H. 1846. Les fontaines publiques de la ville de Dijon. Dalmont, Paris, 647 p.

De Marsily, G. 1986. Quantitative Hydrogeology. Academic Press Inc, Cambridge, 464 p.

Dlubac, K., Knight, R., Song, Y.Q., Bachman, N., Grau, N., Cannia, J. and Williams, J. 2013. Use of NMR logging to obtain estimates of hydraulic conductivity in the High Plains aquifer, Nebraska, USA. Water Resources Research 49, 1871–1886.

Fox, A., Forchhammer, K., Pettersson, A., La Pointe, P. and Lim, D-H. 2012. Geological discrete fracture network model for the Olkiluoto site, Version 2. Posiva report 2012-27. Posiva Oy, 346 p.

Freedman R., Boyd A., Gubelin G., Mckeon D., Morriss C.E. and Flaum C. 1997. Measurement of total NMR porosity adds new value to NMR logging. SPWLA 38th Annual Logging Symposium. In Houston, Texas, USA, 15.-18.6.1997, 14 p.

Fukushima, E. and Roader, S.B.W. 1981. Experimental pulse NMR: A Nuts and Bolts Approach. Addison-Wesley, Massachusetts, USA, 539 p.

Fulcher, G.S. 1925. Analysis of recent measurements of the viscosity of glasses. Journal of the American Ceramic Society 8. 339–355.

Golub, G.H. and Van Loan, C.F. 1983. Matrix computations. The Johns Hopkins University Press, Baltimore and London, 694 p.

Gueguen, Y., and V. Palcaiuckas. 1994. Introduction to the Physics of Rocks. Princeton University Press, Princeton, 294 p.

Guimaraes, A.P. 1998. Magnetism and magnetic resonance in solids. John Wiley & Sons Inc., New York, 203–225.

Hellä, P., Ikonen, A., Mattila, J., Torvela, T. and Wikström, L. 2009. RSC-Programme - Interim Report. Approach and Basis for RSC Development, Layout Determining Features and Preliminary Criteria for Tunnel and Deposition Hole Scale. Posiva working report 2009-29. Posiva Oy, 118 p.

Herrick, R.C., Couturie, S.H. and Best, D.L. 1979. An improved nuclear magnetism logging system and its application to formation evaluation. SPE Annual Technical Conference and Exhibition. In Las Vegas, Nevada, USA, 23.-26.9.1979. Society of Petroleum Engineers, 8 p.

Hirvonen, H. and Hatanpää, E. 2006. Results of Sampling and Analysis of Groundwater from Open Boreholes OL-KR7, OL-KR10, OL-KR19, OL-KR20 and OL-KR27 at Olkiluoto, Eurajoki, in 2004. Posiva working report 2006-80. Posiva Oy, 95 p.

Humborstad. G. 2014. Dynamic Pulsed-Field-Gradient NMR. Springer, Trondheim, 243–296.

Ikonen, A.T.K. 2007. Meteorological data and update of climate statistics of Olkiluoto 2005–2006. Posiva Working Report 2007-86. Posiva Oy, 72 p.

Ikonen, J., Sammaljärvi, J., Siitari-Kauppi, M., Voutilainen, M., Lindberg, A., Kuva, J. and Timonen, J. 2015. Investigation of Rock Matrix Retention Properties Supporting Laboratory Studies I: Mineralogy, Porosity and Pore Structure. Posiva working report 2014-68. Posiva Oy, 82 p.

Johnson, C.D., Keating, K., Walsh, D.O., Lane, J.W. and Falzone, S. 2012. Use of borehole and surface nuclear magnetic resonance methods at Haddam Meadows State Park, Connecticut. 25th Symposium on the application of geophysics to engineering and environmental problems. In Tucson, Arizona, USA, 25.-29.3.2012. Environmental and Engineering Geophysical Society.

Kenyon, W.E., Day, P.I., Straley, C. and Willemsen, J.F. 1986. Compact and consistent representation of rock NMR data from permeability estimation. SPE Annual Technical Conference and Exhibition preprint. In New Orleans, Los Angeles, USA, 5.10.1986. Later published in 1988 as a three-part study of NMR longitudinal relaxation properties of water-saturated sandstones. SPE Formation Evaluation 3. 622–636.

Kenyon, W.E., Day, P.I., Straley, C. 1988. A Three-Part Study of NMR Longitudinal Relaxation Properties of Water-Saturated Sandstones. SPE Formation Evaluation 3, 15 p.

Kenyon, W.E., Howard, J.J., Sezginer, A., Straley, C., Matteson, A., Horkowitz, K. and Ehrlich, R. 1989. Pore-size distribution and NMR in microporous cherty sandstones. SPWLA 30th Annual Logging Symposium Transactions. In Denver, Colorado, USA, 11.-14.6.1989. Society of Petrophysicists and Well-log Analysts, 24 p.

Kenyon, W.E. 1992. Nuclear magnetic resonance as a petrophysical measurement. Nuclear geophysics 6, 153–171.

Kenyon, W.E. 1997. Petrophysical principles of applications of NMR logging, The Log Analyst 38, 21–43.

Kleinberg, R.L., Kenyon, W.E. and Mitra, P.P. 1994. Mechanism of NMR relaxation of fluids in rock. Journal of Magnetic Resonance 108, 206–214.

Kleinberg, R.L. and Jackson, J.A. 2001. An Introduction to the History of NMR Well Logging. Concepts in Magnetic Resonance 13, 340–342.

Kohonen, T. 1982. Self-Organized formation of topologically correct feature maps. Biological Cybernetics 43, 59–69.

Kohonen, T. 2001. Self-Organizing Maps, 3rd edition. Springer, New York, USA, 487 p.

Korsman, K., Holtta, P., Hautala, T. and Wasenius, P. 1984. Metamorphism as an indicator of evolution and structure of the crust in Eastern Finland. Geological Survey of Finland, Bulletin 328, 40 p.

Korsman, K., Korja, T., Pajunen, M., Virransalo, P. and GGT/SVEKAWorking Group. 1999. The GGT/SVEKA transect: structure and evolution of the continental crust in the Paleoproterozoic Svecofennian Orogen in Finland. International Geology Review 41. 47 p.

Koskinen, L., Ahokas, H., Vaittinen, T., Hartley, L., Löfman, J. and Mészáros, F. 2012. Hydrogeology in Olkiluoto Site Description 2011. Posiva Working report 2011-02. Posiva Oy, 347–501.

Kozeny, J. 1927. Ueber kapillare leitung des wasser im boden, Wein Akad Wiss, 136, 271–307.

Krejci, M., Lett, M., Lloyd, A., Hopper, T., Neville, T. and Birt, B. 2018. Groundwater assessment in a coal measures sequence using borehole magnetic resonance. ASEG Extended Abstracts 2018:1, 1–5.

Kuusela, A. 1986. About measurements of hydraulic conductivity in bedrock and interpretation of the results. Master's thesis, Technical University of Helsinki. Unpublished.

Lahtinen, R. 1994. Crustal evolution of the Svecofennian and Karelian domains during 2.1–1.79 Ga, with special emphasis on the geochemistry and origin of 1.93–1.91 Ga gneissic tonalities and associated supracrustal rocks in the Rautalampi area, Central Finland. Geological survey of Finland, Bulletin 378, 128 p.

Lahtinen, R., Korja, A. and Nironen, M. 2005. Paleoproterozoic tectonic evolution. In: Lehtinen, M., Nurmi, P.A. and Rämö, O.T. Precambrian Geology of Finland: Key to the Evolution of the Fennoscandian Shield. Developments in Precambrian Geology 14, 481–531.

Löfman, J. 1999. Site Scale Groundwater Flow in Olkiluoto. Posiva report 99-03. Posiva Oy, 121 p.

Mardon, D., Prammer, M.G. and Coates, G.R. 1996. Characterization of light hydrocarbon reservoirs by gradient-NMR well logging. Magnetic Resonance Imaging 14, 769–777.

Marschall, D., Gardner, J.S. and Curby, F.M. 1997. MR Laboratory Measurements—Requirments to Assure Successful Measurements that Will Enhance MRI Log Interpretation. Society of Core Analysts International Symposium. In Calgary, Alberta, Canada, 7.-10.9.1997. Society of Core Analysts, 12 p.

Marsily, G. 1986. Quantitative Hydrology, Groundwater Hydrology for Engineers. Academic Press Inc., London, 440 p.

Martin P. and Dacy J., 2004. Effective Qv by NMR tests. SPWLA 45th Annual Logging Symposium In Noordwijk, The Netherlands, 6.-9.6.2003. Society of Petrophysicists and Well Log Analysts, 14 p.

McEwen, T. and Äikäs, T. 2000. The site selection process for a spent fuel repository in Finland – Summary report. Posiva report 2000-15. Posiva Oy, 224 p.

Meiboom, S. and Gill, D. 1958. Modified spin-echo method for measuring nuclear relaxation times. Review of Scientific Instruments 29, 688–691.

Morriss, C.E., MacInnes, J., Freedman, R., Smaardyk, J., Straley, C., Kenyon, W.E., Vinegar, H.J., and Tutunjian, P.N. 1993. Field test of an experimental pulsed nuclear magnetism tool. SPWLA 34th Annual Logging Symposium. In Calgary, Alberta, Canada, 13.-16.6.1993. Society of Petrophysicists and Well Log Analysts, 23 p.

Moye, D. G. 1967. Diamond Drilling for Foundation Exploration. The Institution of Engineers Australia Investigation Symposium. In Brisbane, Australia, 1966. Institution of Engineers Australia, 95–100.

Nironen, M. 1997. The Svecofennian Orogen: a tectonic model. Precambrian Research 86, 21–44.

Nironen, M. 1999. Structural and magmatic evolution in the Loimaa area, southwestern Finland. Geological Survey Finland, Bulletin 71, 57–71.

NMRRSA's website 2020. Visited on 5.11.2020. https://www.nmrservices.com.au/

Lauterbur P.C. 1973. Image Formation by Induced Local Interaction; Examples Employing Nuclear Magnetic Resonance. Nature 242, 190–191.

Nikias, P.A. and Eyraud, L.E. 1963. Some Examples of Nuclear Magnetism Logging in Three San Joaquin Valley Oil Fields. Journal of Petroleum Technology 15, 23–27.

OL-KR56 hauraat lävistykset. 2020. Table about all brittle intersections of drillhole OL-KR56. Unpublished.

Pittman, E.D. 1992. Relationship of porosity and permeability to various parameters derived from mercury injection-capillary pressure curves for sandstone. American Association of Petroleum Geologists, Bulletin 76, 191–198.

Posiva Oy and Suomen Malmi Oy . 2012 A. Core logging table of OL-KR56. Unpublished.

Posiva Oy and Suomen Malmi Oy. 2012 B. Core box photos of OL-KR56. Unpublished.

Posiva Oy. 2013. KBS-3H Complementary Studies 2008–2010. Posiva report 2013-03. Posiva Oy, 322 p.

Posiva Oy's website 2020. Final disposal: Selecting the Site: the Final Disposal at Olkiluoto. Website visited on 5.6.2020. http://www.posiva.fi/en/final_disposal/selecting_the_site_the_final_disposal_at_olkiluoto#.X4BdMGgzbIU

Posiva Oy's website 2020. Research and development: Groundwater investigations. Website visited on 16.6.2020. http://www.posiva.fi/en/final_disposal/research_and_development/groundwater_investigations#.X32hEWgzYuU

Prammer, M.G., Mardon, D., Coates, G.R. and Miller, M.N. 1995. Lithology-independent gas detection by gradient-NMR logging. SPE Annual technical conference and exhibition. In Dallas, Texas, USA, 22.–25.10.1999. Soviety of Petroleum Engineers, 12 p.

Pulkkinen, P. and Hurmerinta, E. 2019. Hydraulic conductivity measurements with HTU at Eurajoki, Olkiluoto, in drillhole OL-KR56 in 2017. Posiva working report 2018-28. Posiva Oy, 38 p.

Purcell, E.M., Torrey, H.C. and Pound, R.V. 1946. Resonance absorption by nuclear magnetic moments in solid. Physical Review 69, 37–38.

Qteq Pty Ltd. 2018. Principles and applications of Borehole Magnetic Resonance. Unpublished.

Ripatti, K., Komulainen, J. and Pöllänen, J. 2013. Difference flow and electrical conductivity measurements at the Olkiluoto site in Eurajoki, drillholes OL-KR56, OL-KR57 and OL-KR57B. Posiva working report 2013-26. Posiva Oy, 176 p.

Sedighi, M., Bennett, D., Masum, S.A., Thomas, H.R. and Johansson, E. 2014. Analysis of temperature data at the Olkiluoto. Posiva working report 2013-58. Posiva Oy, 78 p.

Selonen, O. and Ehlers, C. 1998. Structural observations on the Uusikaupunki trondhjemite sheet, southwestern Finland. GFF, Journal of the Geological Society of Sweden, 120. 379–382.

Siitari-Kauppi, M., Ikonen, J., Kauppi, L. and Lindberg, A. 2010. Investigation of Porosity and Pore Structure Adjacent to Fractures by PMMA Method; Samples Taken from Drill Cores at Olkiluoto. Posiva working report 2010-66. Posiva Oy, 86 p.

Spencer, R.G. 2010. Equivalence of the Time-Domain Matched Filter and the Spectral-Domain Matched Filter in One-Dimensional NMR spectroscopy. Concepts in Magnetic Resonance Part A 36, 255–265.

Straley C., Rossini D., Vinegar H.J., Tutunjian P. and Morriss C.E. 1997. Core analysis by low-field NMR. Log Analyst 38, 84–93.

Tammann, G. and Hesse, W. 1926. Die Abhängigkeit der Viscosität von der Temperatur bie unterkühlten Flüssigkeiten. Zeitschrift für anorganische und allgemeine Chemie 156. 245–257.

Testamanti, M.N. and Rezaee, R. 2017. Determination of NMR T_2 cut-off for clay bound water in shales: A casestudy of Carynginia Formation, Perth Basin, Western Australia. Journal of Petroleum Science and Engineering 149, 497–503.

Thompson, A., Katz, A.J. and Krohn, C.E. 1987. The micro-geometry and transport properties of sedimentary rock. Advances in Physics 36, 625–694.

Timur, A. 1968. An investigation of permeability, porosity, and residual water saturation relationships for sandstone reservoirs. The Log Analyst 9, 8–17.

Toropainen, V. 2011. Core drilling of Hydco drillholes ONK-PP262 and ONK-PP274 in ONKALO at Olkiluoto 2010. Posiva working report 2011-71. Posiva Oy, 36 p.

Toropainen, V. 2012. Core drilling of deep drillhole OL-KR56 at Olkiluoto in Eurajoki 2011–2012. Posiva working report 2012–52. Posiva Oy, 212 p.

Tuisku, P. and Kärki, A. 2010. Metamorphic Petrology of Olkiluoto. Posiva Working report 2010-54. Posiva Oy, 76 p.

Vaittinen, T., Ahokas, H., Nummela, J., Pentti, E. and Paulamäki, S. 2020. Hydrogeological structure model of the Olkiluoto site in 2015. Posiva working report 2019-06. Posiva Oy, 443 p.

Venard, J.K. and Street, R.L. 1975. Elementary Fluid Mechanics, 5th edition. Wiley, New York, 760 p.

Vernik, L. and Nur, A. 1992. Petrophysical classification of siliciclastics for lithology and porosity prediction from seismic velocities. AAPG Bulletin 76, 1295–1309 p.

Vinegar, H. 1995. Relaxation mechanisms, chapter 3. 36th Annual SPWLA Logging symposium: Nuclear magnetic resonance logging shot course notes, variously paginated. In Abu Dhabi, United Arab Emirates, 13.-16.11.2017. Society of Petroleum Engineers, 24 p.

Viswanath, D.S. and Natarajan, G. 1989. Data book on the viscosity of liquids. Hemisphere Publishing Corporation, New York, 990 p.

Vogel, H.1921. Das Temperaturabhaengigkeitsgesetz der Viskositaet von Fluessigkeiten. Physikalische Zeitschrift 22. 645 p.

Väisänen, M. 1999. Structural and metamorphic evolution of the Turku migmatite complex, southwestern Finland. Geological Survey of Finland, Bulletin 71. 177–21.

Walsh, D., Turner, P., Grunewald, E., Zhang, H., Butler, J.J., Reboulet, E., Knobbe, S., Christy, T., Lane, J.W., Johnson, C.D., Munday, T. and Fitzpatrick, A. 2013. A small-diameter NMR logging tool for groundwater investigations. Ground Water 51, 914–926.

Warren, J.E. and Root, P.J. 1963. The Behavior of Naturally Fractured Reservoirs. Society of Petroleum Engineers Journal 3. 245–256.

Ylinen, A. 1994. N-Dimensional flow behaviour in the single borehole pumping test. Working report PATU-94-54. Teollisuuden Voima Oy. Unpublished.

APPENDICES

Appendix A: BMR logs from OL-KR56

Processed BMR logs from OL-KR56. The logs contain T_2 distribution (T2 dist) on top of T_2 distribution mean (T2 dist mean), total porosity, fluid volumes (dark green is clay bound water, light green is capillary bound water and blue is moveable water) and Timur-Coates (T-C K) and Schlumberger-Doll-Research (SDR K) permeabilities.

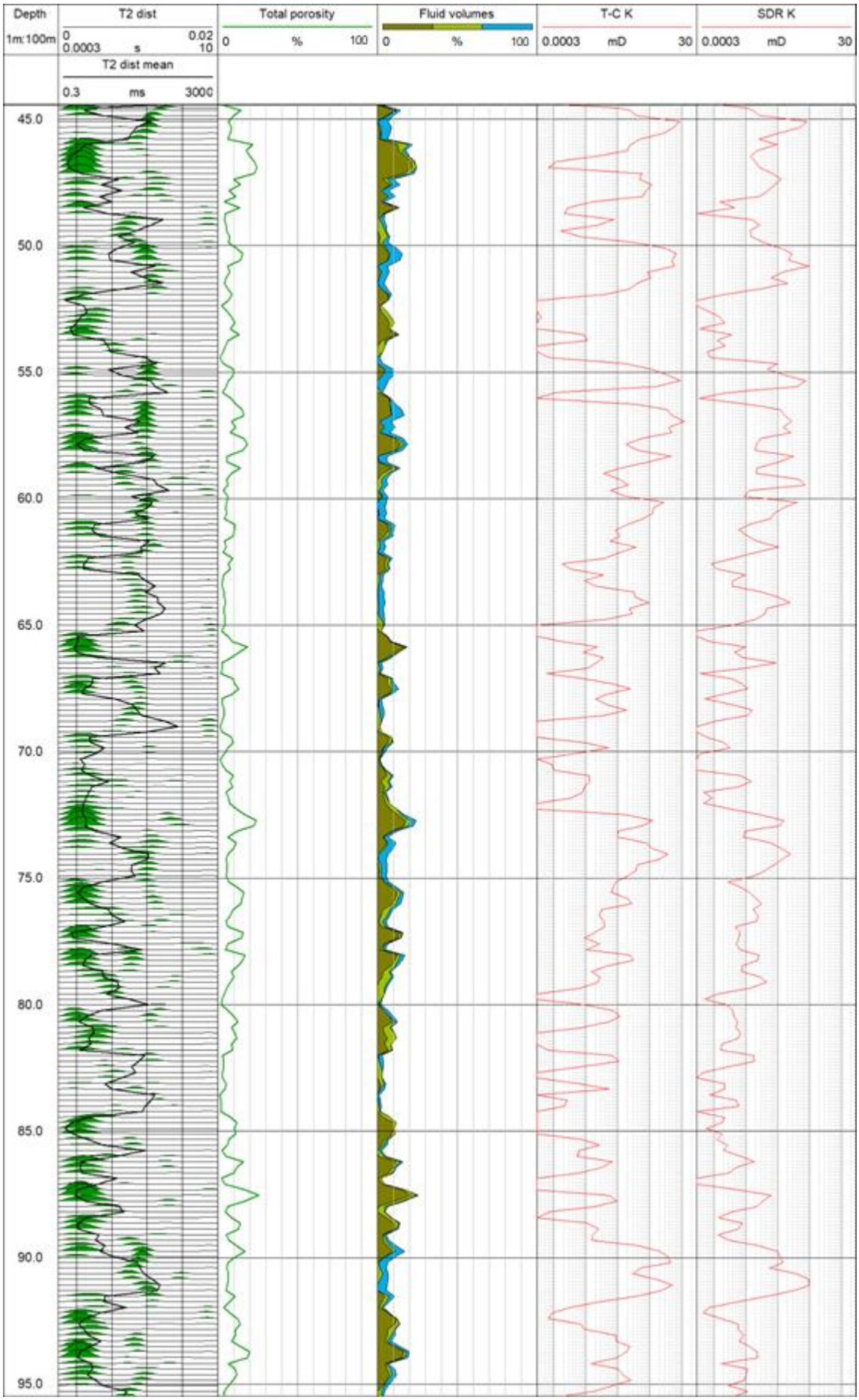
Depth
1m:100m
T2 dist
0
0.0003
s
0.02
10
T2 dist mean
0.3
ms
3000
Total porosity
0
%
100
Fluid volumes
0
%
100
T-C K
0.0003
mD
30
SDR K
0.0003
mD
30
45.0
50.0
55.0
60.0
65.0
70.0
75.0
80.0
85.0
90.0
95.0

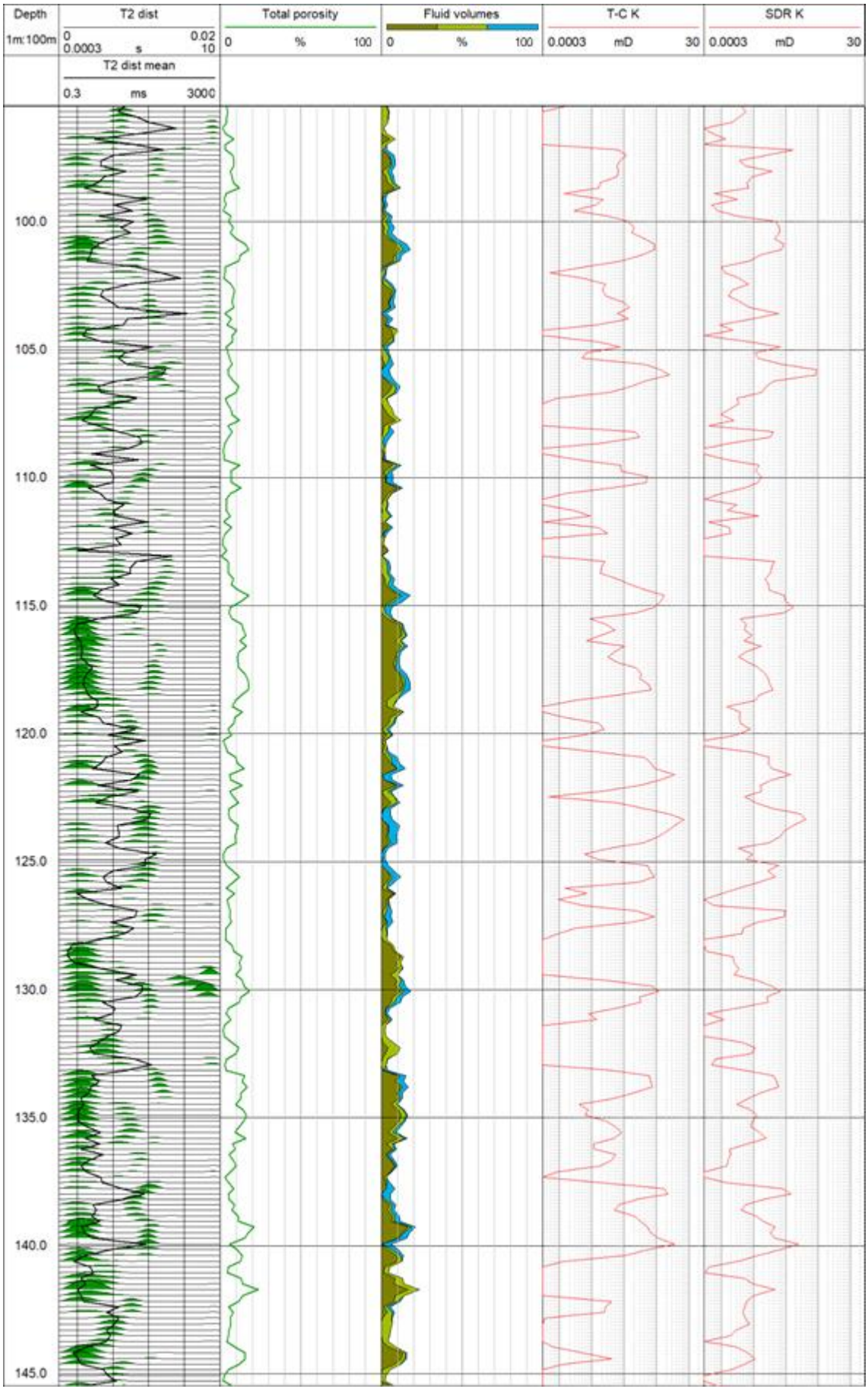
Depth
1m:100m
T2 dist
0
0.0003
s
0.02
10
T2 dist mean
0.3
ms
3000
Total porosity
0
%
100
Fluid volumes
0
%
100
T-C K
0.0003
mD
30
SDR K
0.0003
mD
30
100.0
105.0
110.0
115.0
120.0
125.0
130.0
135.0
140.0
145.0

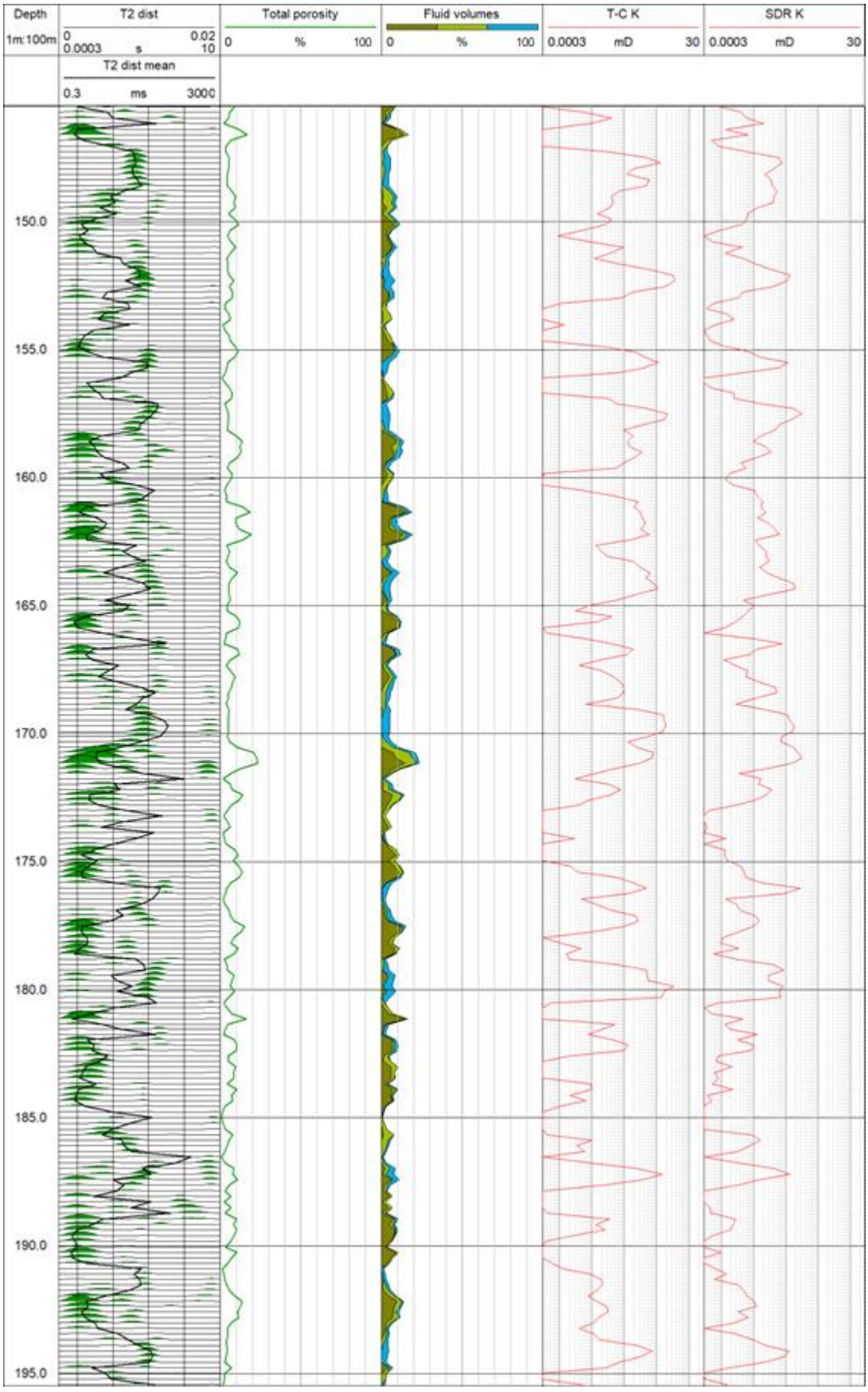
Depth
1m:100m
T2 dist
0
0.0003
s
0.02
10
T2 dist mean
0.3
ms
3000
Total porosity
0
%
100
Fluid volumes
0
%
100
T-C K
0.0003
mD
30
SDR K
0.0003
mD
30
150.0
155.0
160.0
165.0
170.0
175.0
180.0
185.0
190.0
195.0

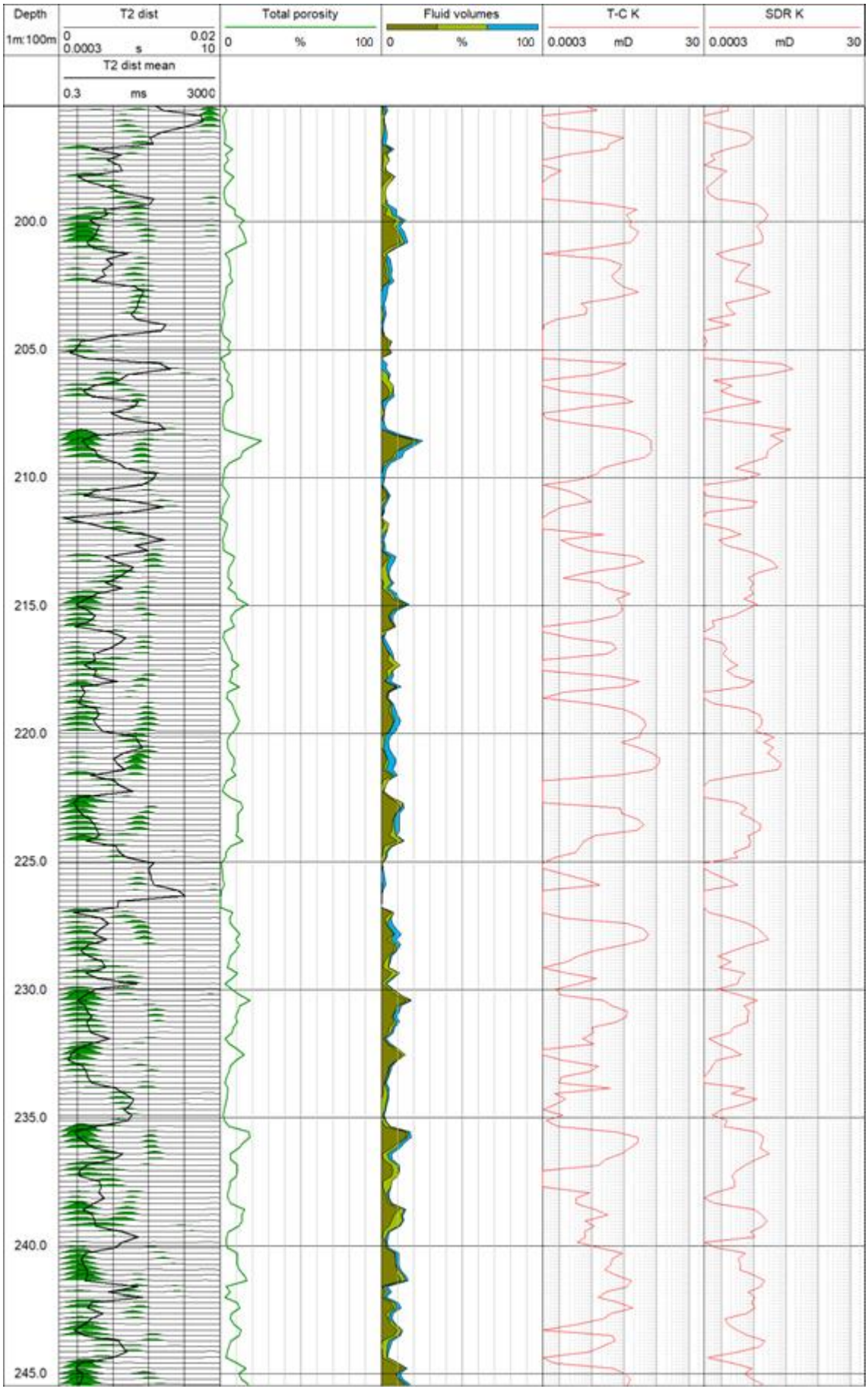
Depth
1m:100m
T2 dist
0
0.0003
s
0.02
10
T2 dist mean
0.3
ms
3000
Total porosity
0
%
100
Fluid volumes
0
%
100
T-C K
0.0003
mD
30
SDR K
0.0003
mD
30
200.0
205.0
210.0
215.0
220.0
225.0
230.0
235.0
240.0
245.0

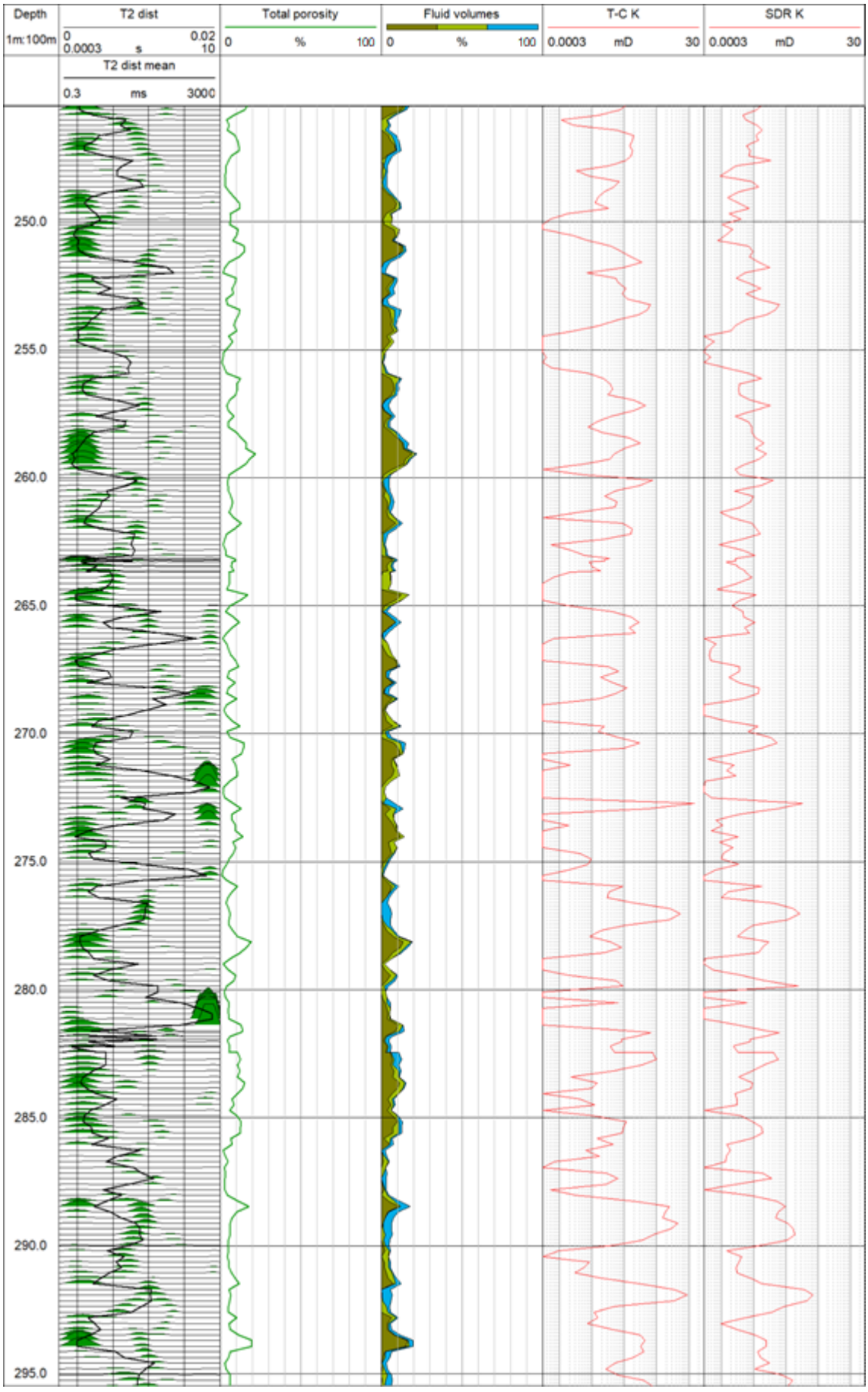
Depth
1m:100m
T2 dist
0
0.0003
s
0.02
10
T2 dist mean
0.3
ms
3000
Total porosity
0
%
100
Fluid volumes
0
%
100
T-C K
0.0003
mD
30
SDR K
0.0003
mD
30
250.0
255.0
260.0
265.0
270.0
275.0
280.0
285.0
290.0
295.0

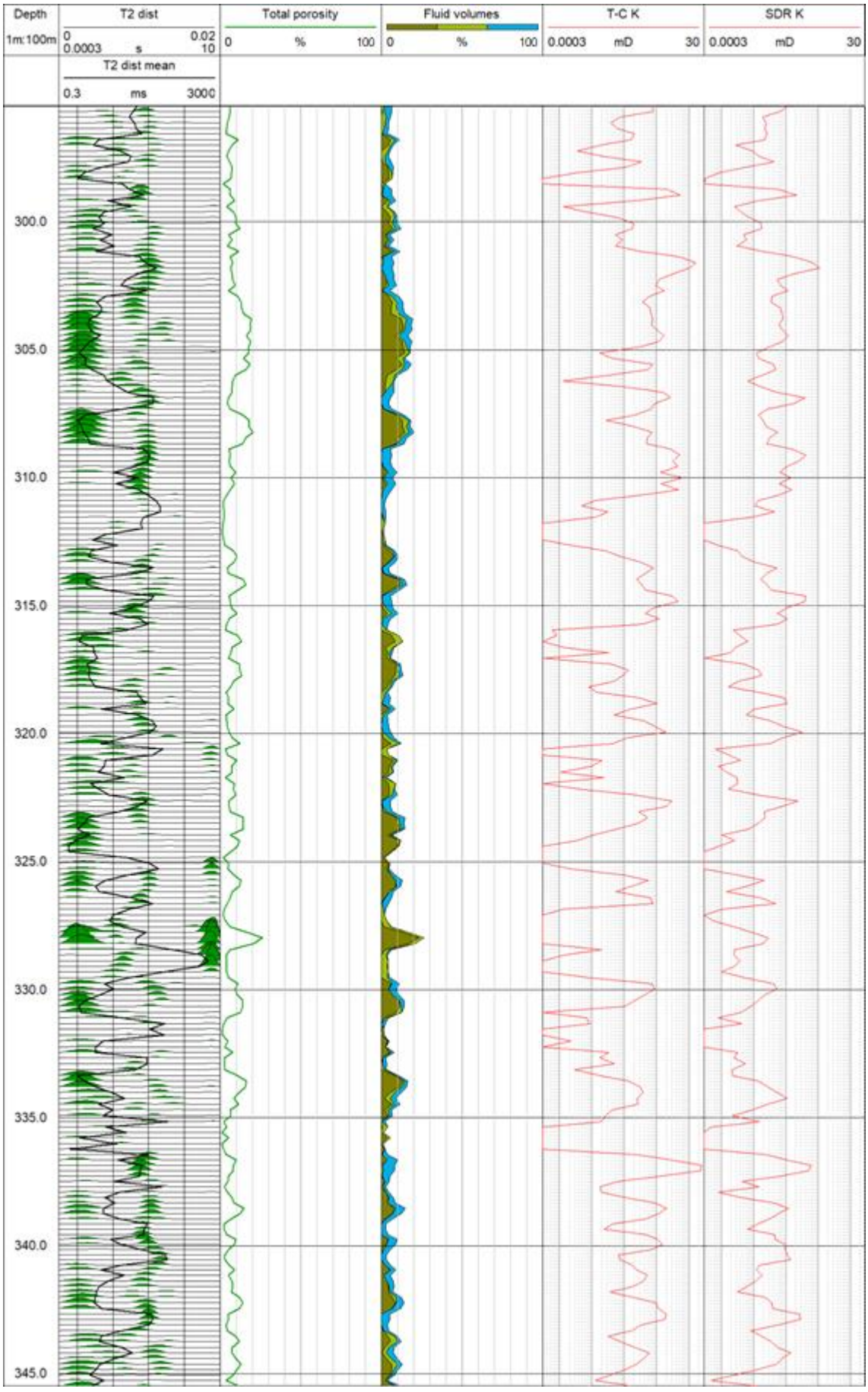
Depth
1m:100m
T2 dist
0
0.0003
s
0.02
10
T2 dist mean
0.3
ms
3000
Total porosity
0
%
100
Fluid volumes
0
%
100
T-C K
0.0003
mD
30
SDR K
0.0003
mD
30
300.0
305.0
310.0
315.0
320.0
325.0
330.0
335.0
340.0
345.0

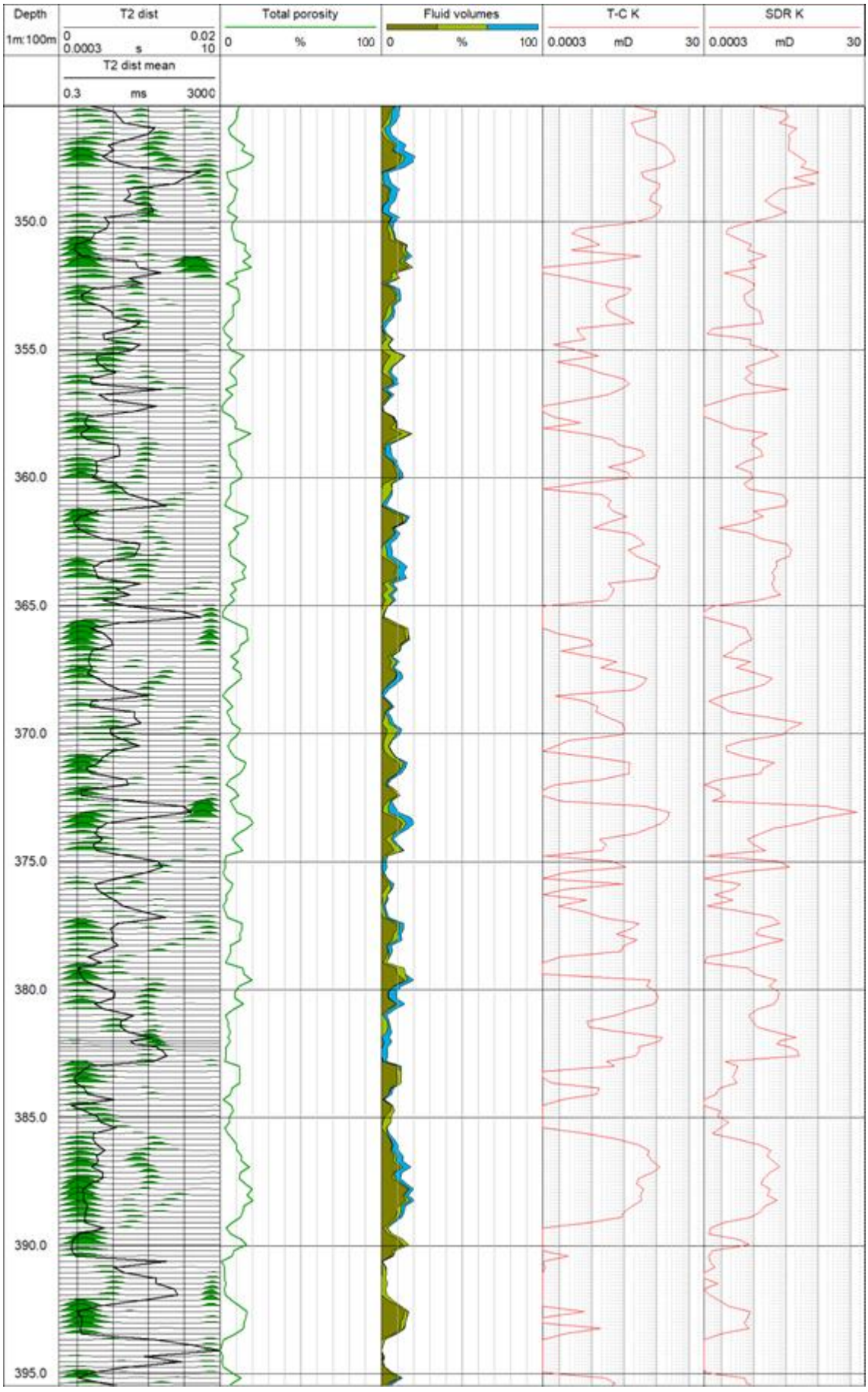
Depth
1m:100m
T2 dist
0
0.0003
s
0.02
10
T2 dist mean
0.3
ms
3000
Total porosity
0
%
100
Fluid volumes
0
%
100
T-C K
0.0003
mD
30
SDR K
0.0003
mD
30
350.0
355.0
360.0
365.0
370.0
375.0
380.0
385.0
390.0
395.0

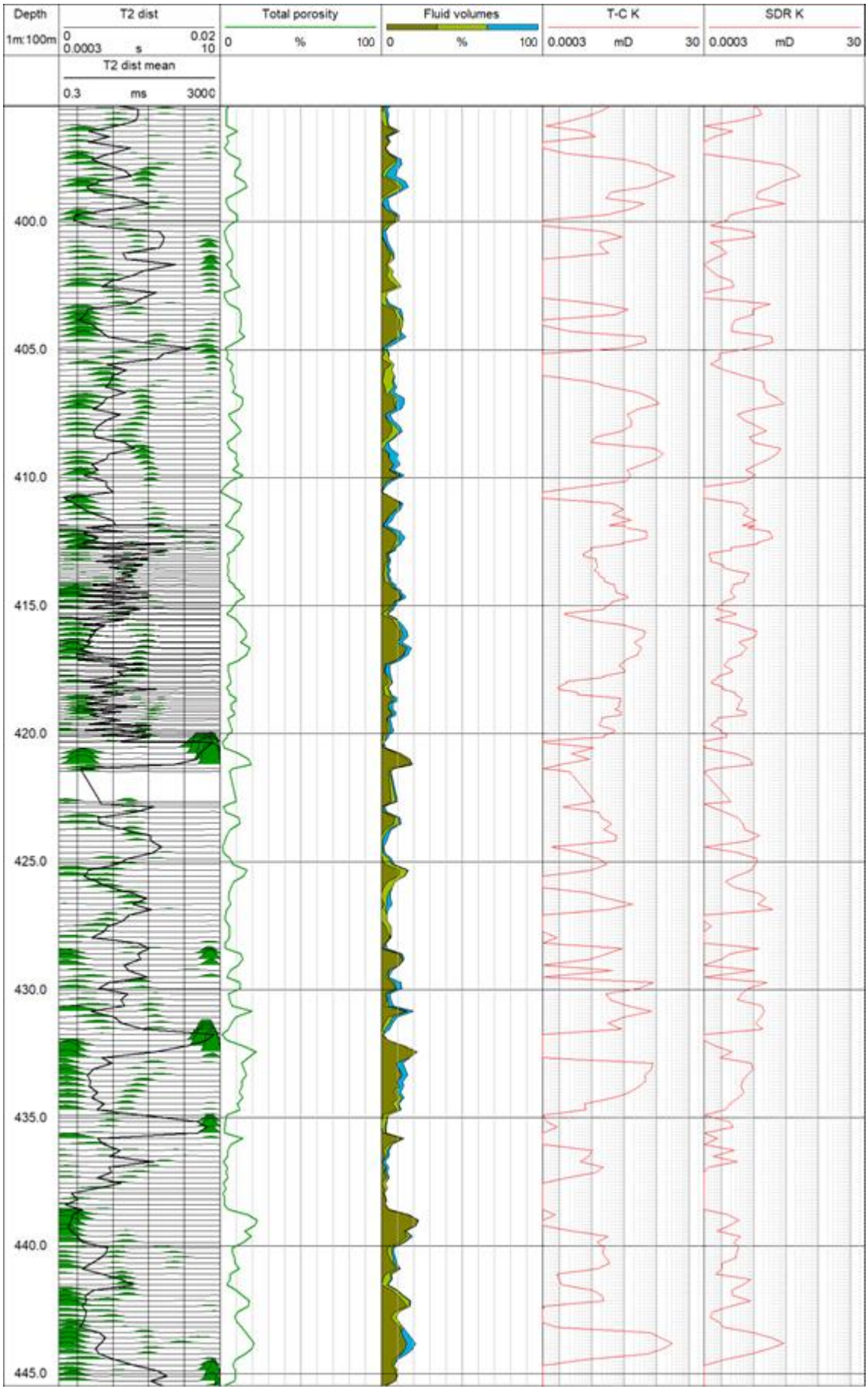
Depth
1m:100m
T2 dist
0
0.0003
s
0.02
10
T2 dist mean
0.3
ms
3000
Total porosity
0
%
100
Fluid volumes
0
%
100
T-C K
0.0003
mD
30
SDR K
0.0003
mD
30
400.0
405.0
410.0
415.0
420.0
425.0
430.0
435.0
440.0
445.0

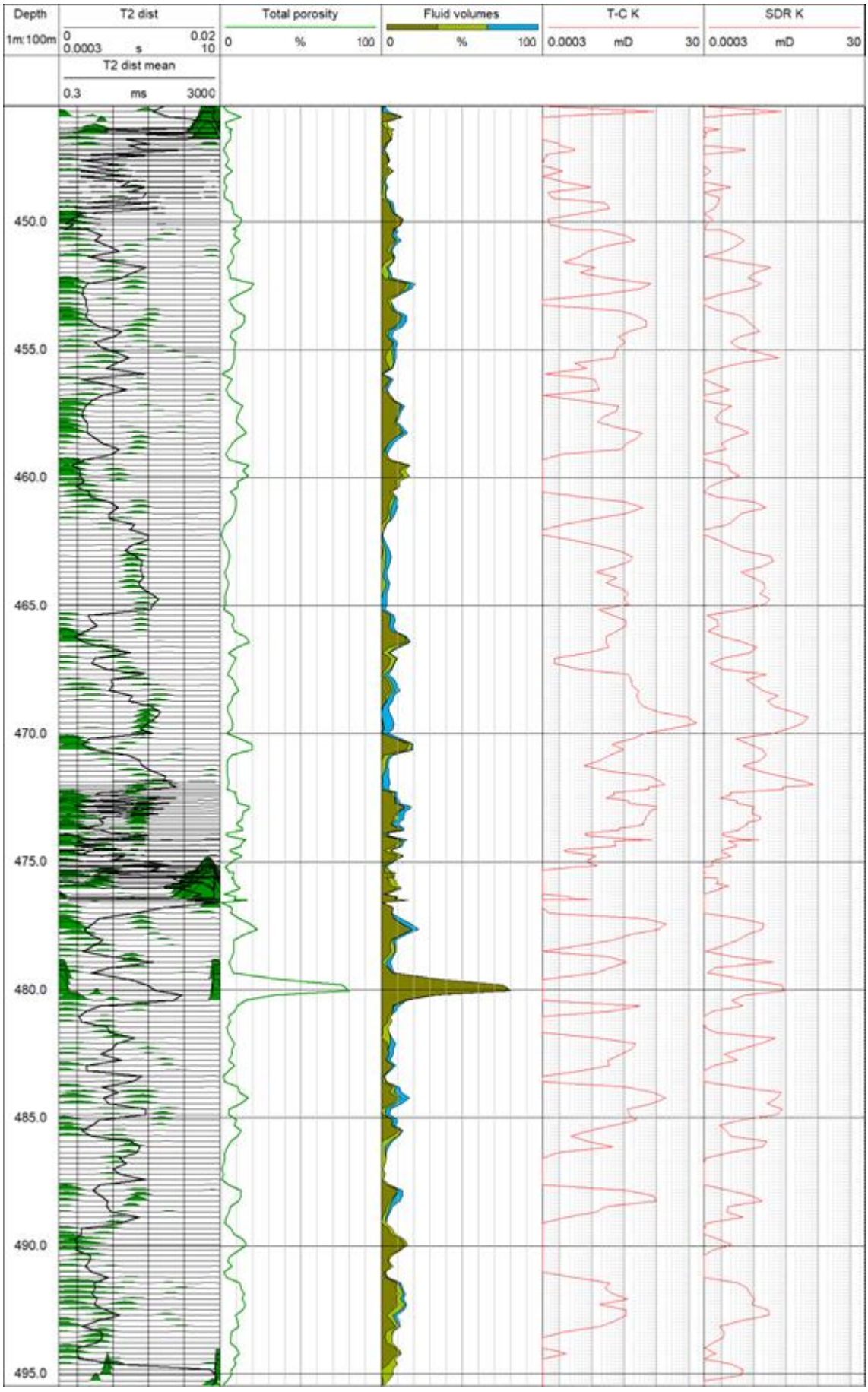
Depth
1m:100m
T2 dist
0
0.0003
s
0.02
10
T2 dist mean
0.3
ms
3000
Total porosity
0
%
100
Fluid volumes
0
%
100
T-C K
0.0003
mD
30
SDR K
0.0003
mD
30
450.0
455.0
460.0
465.0
470.0
475.0
480.0
485.0
490.0
495.0

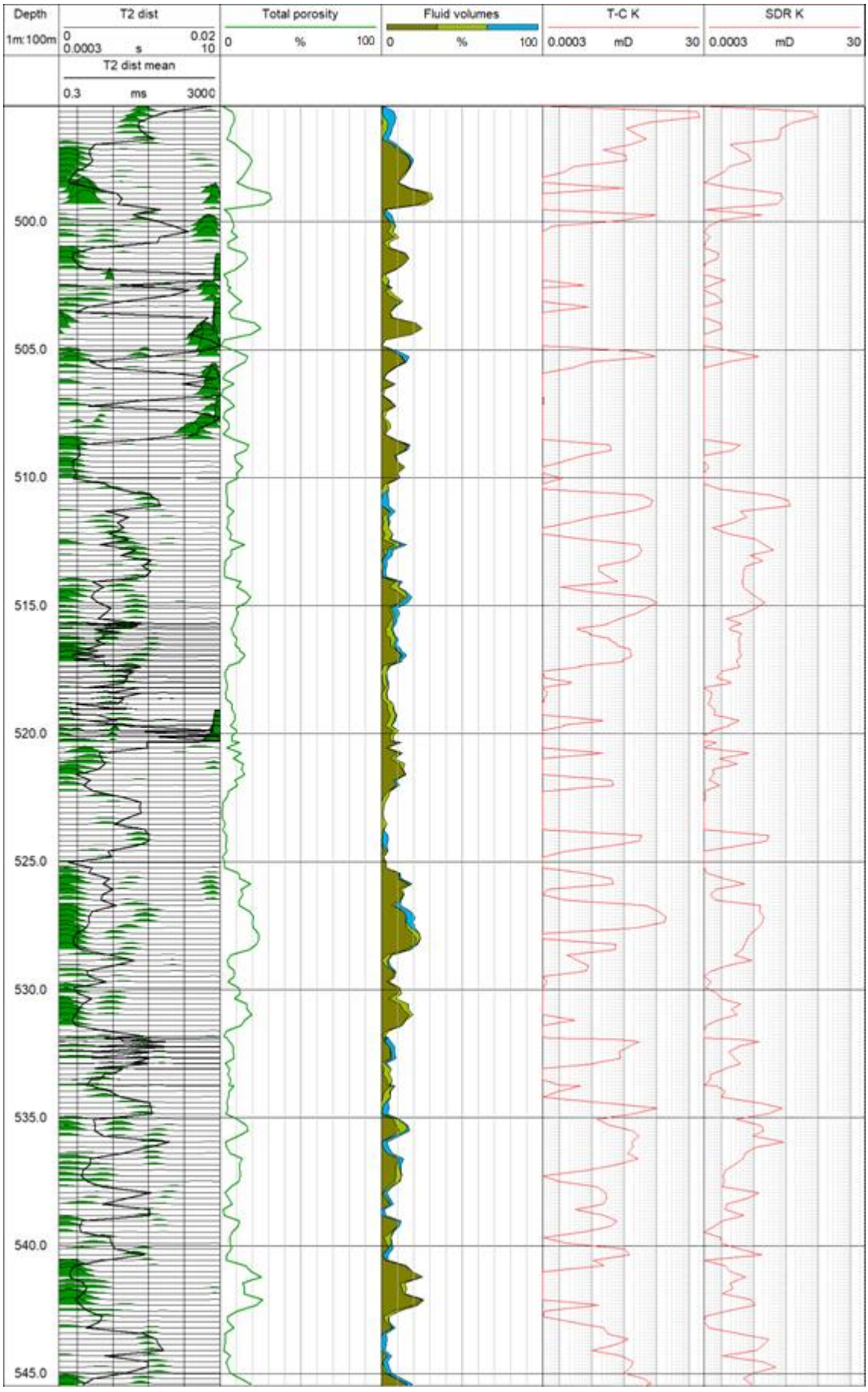
Depth
1m:100m
T2 dist
0
0.0003
s
0.02
10
T2 dist mean
0.3
ms
3000
Total porosity
0
%
100
Fluid volumes
0
%
100
T-C K
0.0003
mD
30
SDR K
0.0003
mD
30
500.0
505.0
510.0
515.0
520.0
525.0
530.0
535.0
540.0
545.0

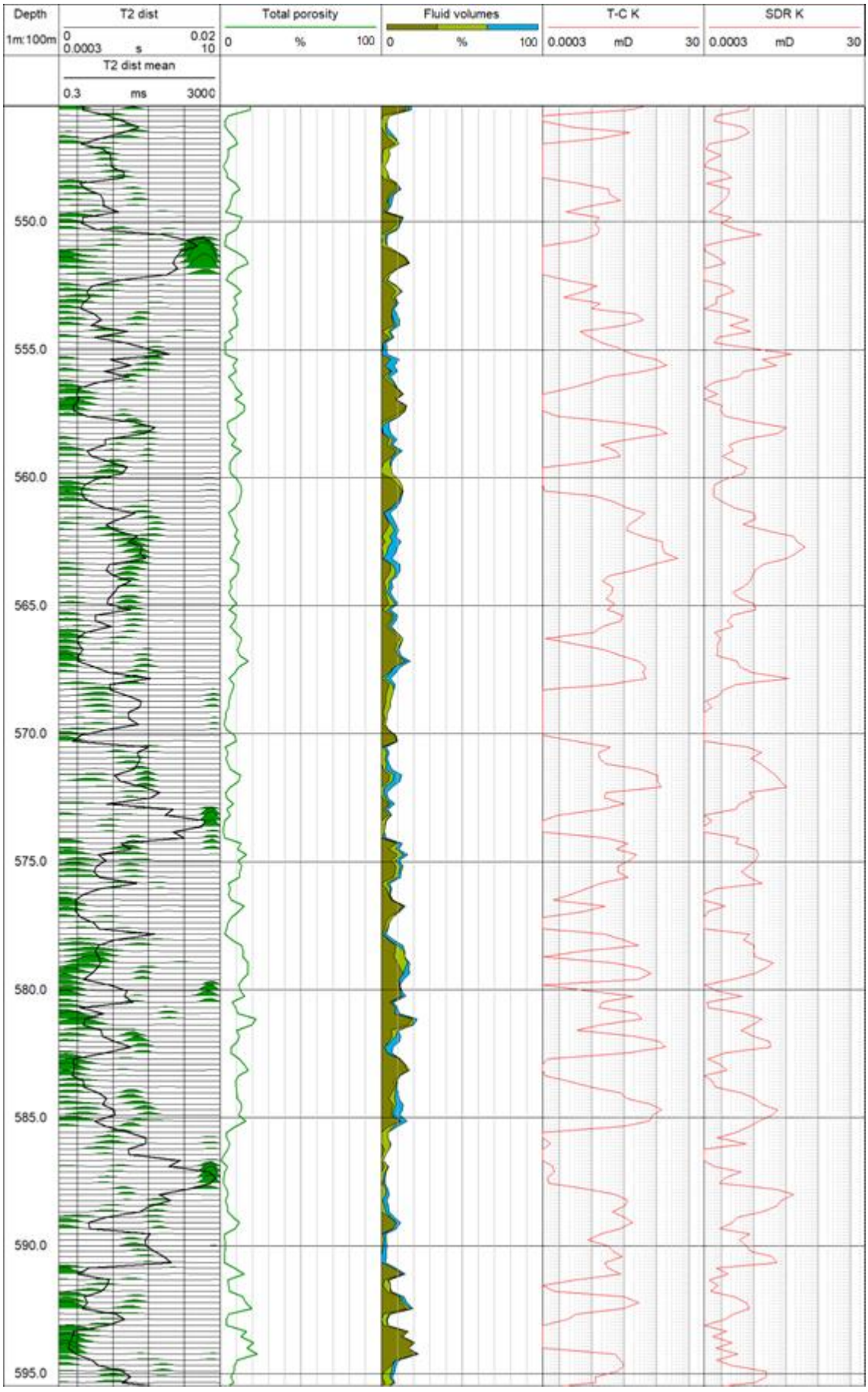
Depth
1m:100m
T2 dist
0
0.0003
s
0.02
10
T2 dist mean
0.3
ms
3000
Total porosity
0
%
100
Fluid volumes
0
%
100
T-C K
0.0003
mD
30
SDR K
0.0003
mD
30
550.0
555.0
560.0
565.0
570.0
575.0
580.0
585.0
590.0
595.0

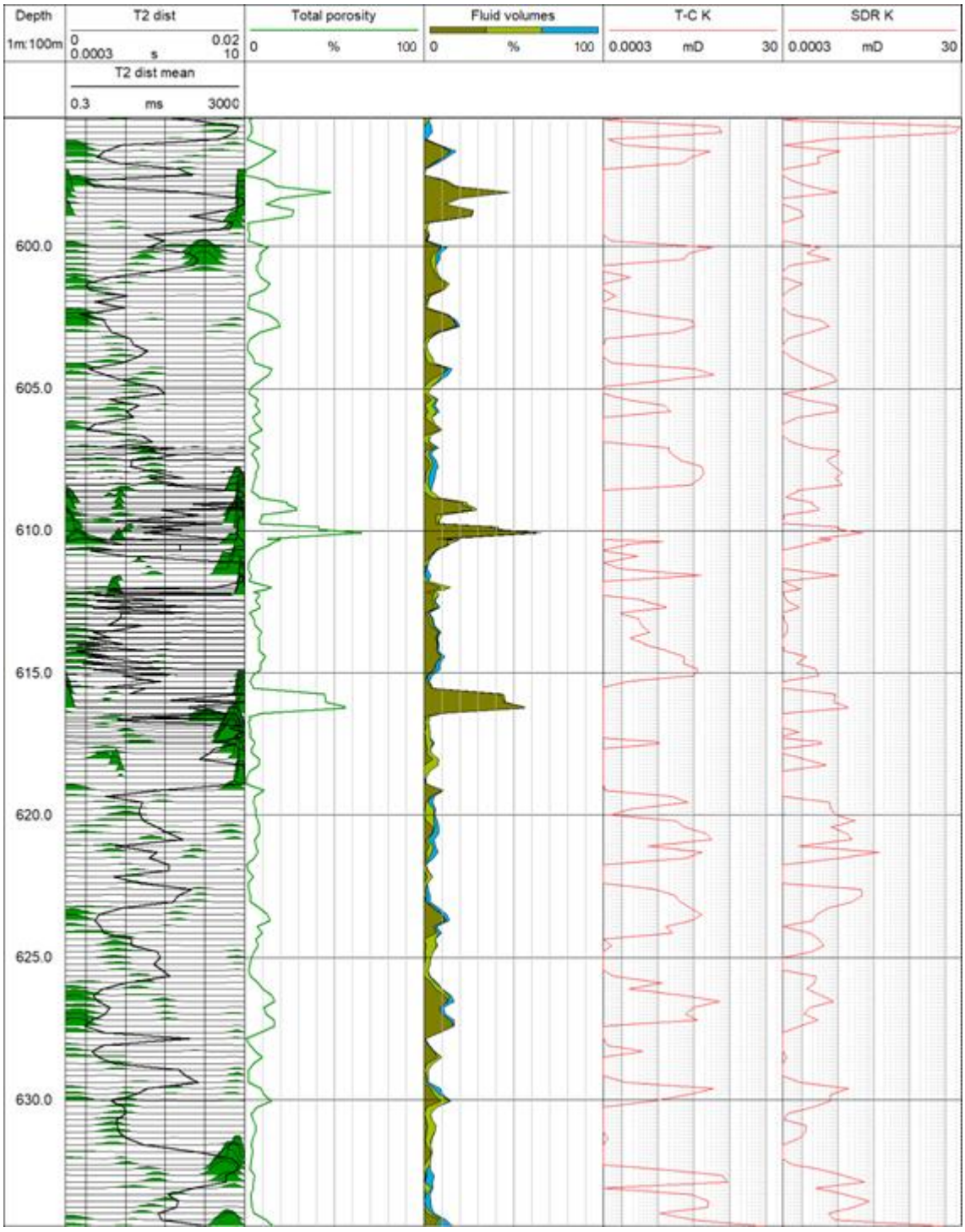
Depth
1m:100m
T2 dist
0
0.0003
s
0.02
10
T2 dist mean
0.3
ms
3000
Total porosity
0
%
100
Fluid volumes
0
%
100
T-C K
0.0003
mD
30
SDR K
0.0003
mD
30
600.0
605.0
610.0
615.0
620.0
625.0
630.0

Appendix B: Lithological and fracture logs of OL-KR56 from 45.0–645.0 m

LEGEND

Lithology

	Diatexitic gneiss
	Veined gneiss
	Mica gneiss
	Mafic gneiss
	Quartz gneiss
	Pegmatite granite
	Tonalitic granodioritic granite gneiss
	K-feldspar porphyry
	No lithology data

Fracture types

	Not assigned
	Open
	Tight
	Filled
	Slickenside
	Clay filled
	Grain filled

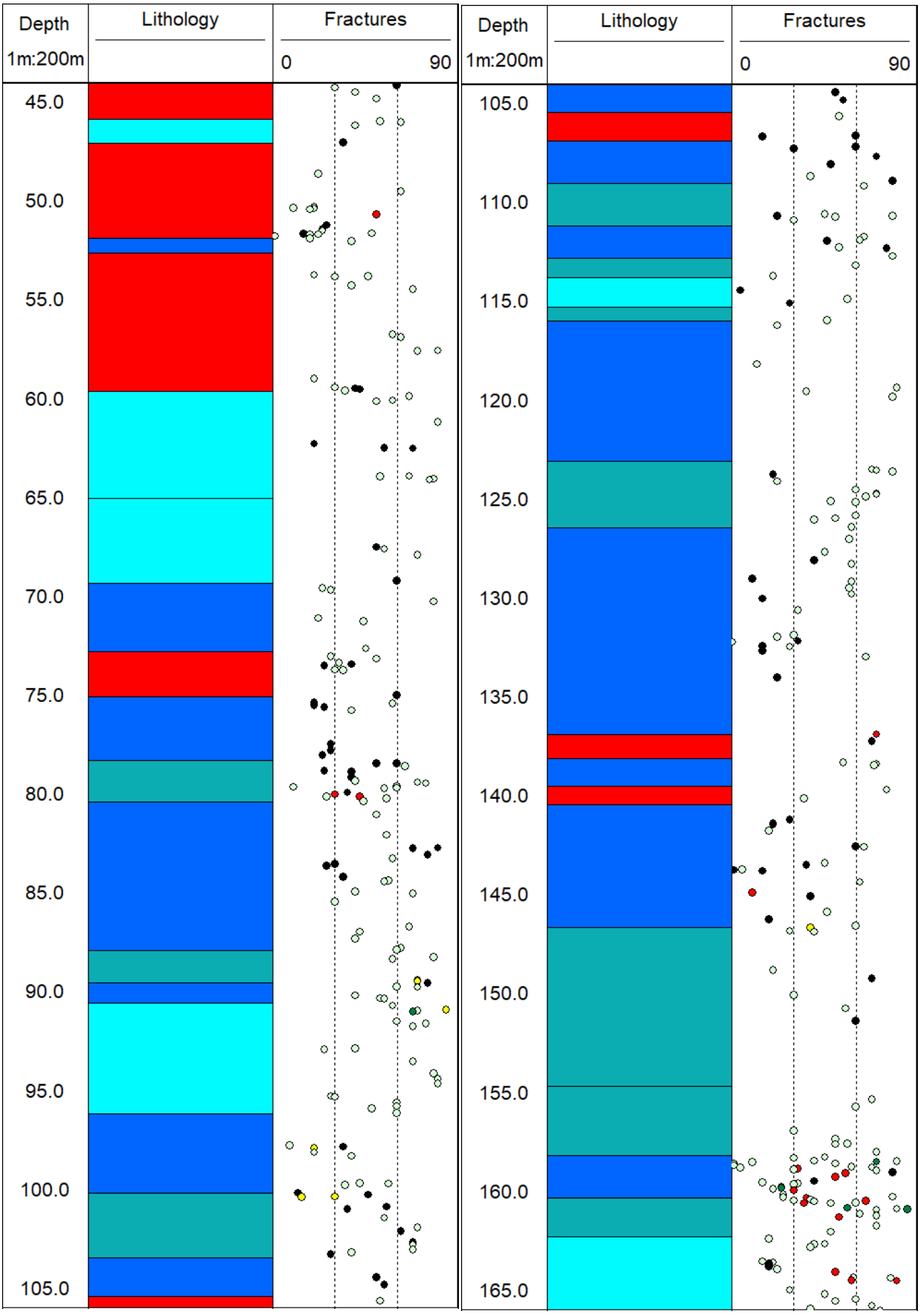
Depth
1m:200m
Lithology
Fractures
0
90
45.0
50.0
55.0
60.0
65.0
70.0
75.0
80.0
85.0
90.0
95.0
100.0
105.0
Depth
1m:200m
Lithology
Fractures
0
90
105.0
110.0
115.0
120.0
125.0
130.0
135.0
140.0
145.0
150.0
155.0
160.0
165.0

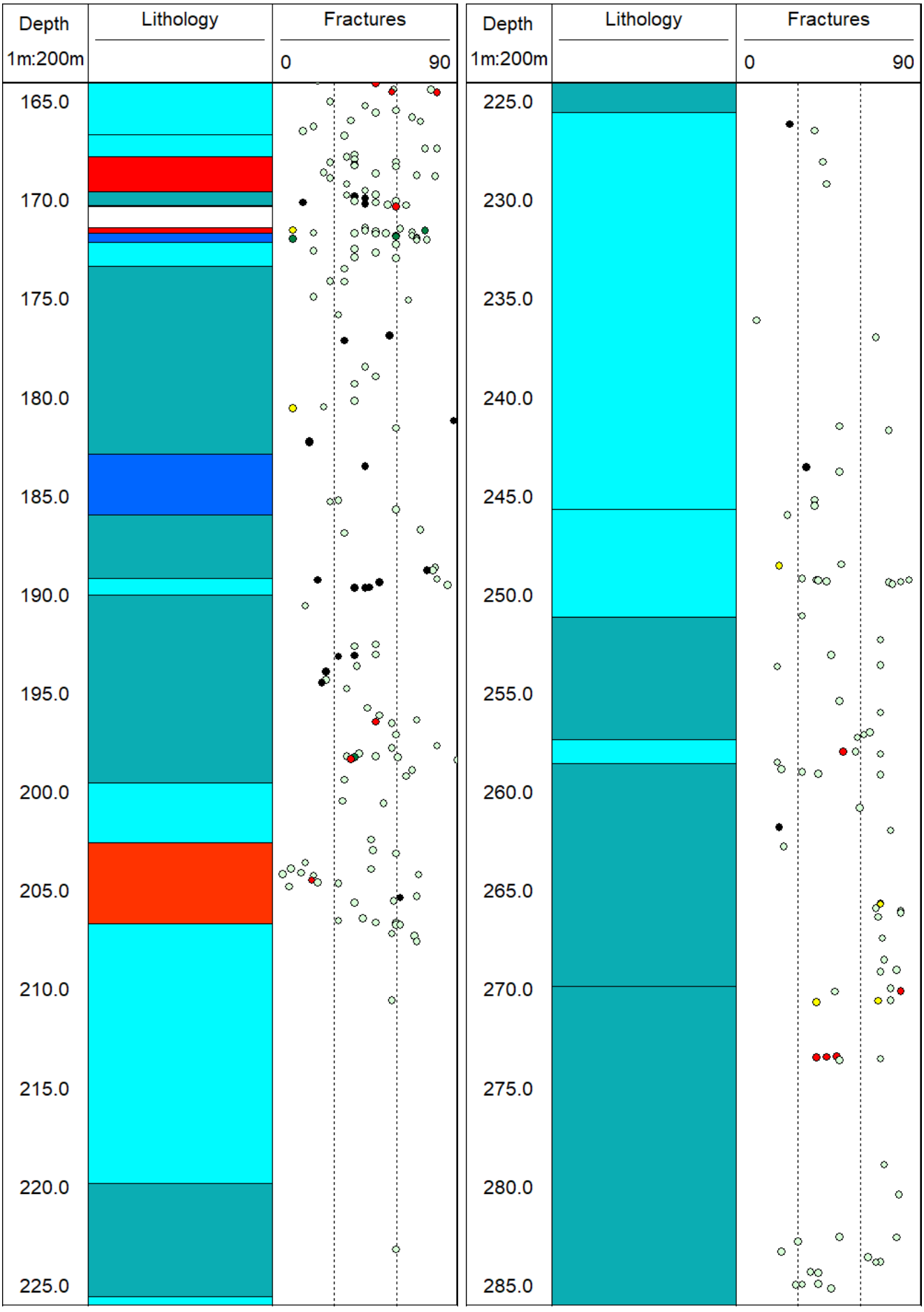
Depth
1m:200m
Lithology
Fractures
0
90
165.0
170.0
175.0
180.0
185.0
190.0
195.0
200.0
205.0
210.0
215.0
220.0
225.0
Depth
1m:200m
Lithology
Fractures
0
90
225.0
230.0
235.0
240.0
245.0
250.0
255.0
260.0
265.0
270.0
275.0
280.0
285.0

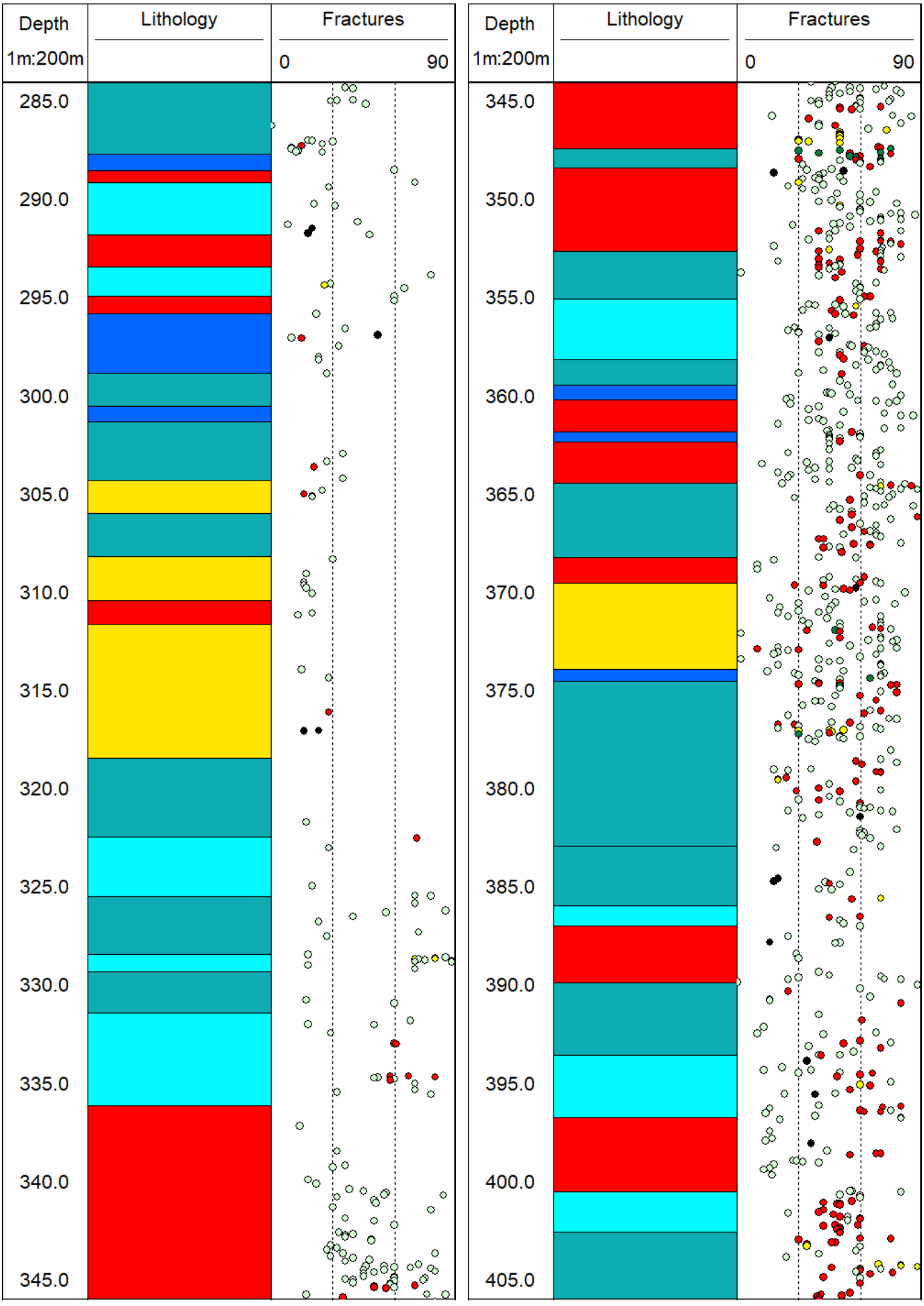
Depth
1m:200m
Lithology
Fractures
0
90
285.0
290.0
295.0
300.0
305.0
310.0
315.0
320.0
325.0
330.0
335.0
340.0
345.0
Depth
1m:200m
Lithology
Fractures
0
90
345.0
350.0
355.0
360.0
365.0
370.0
375.0
380.0
385.0
390.0
395.0
400.0
405.0

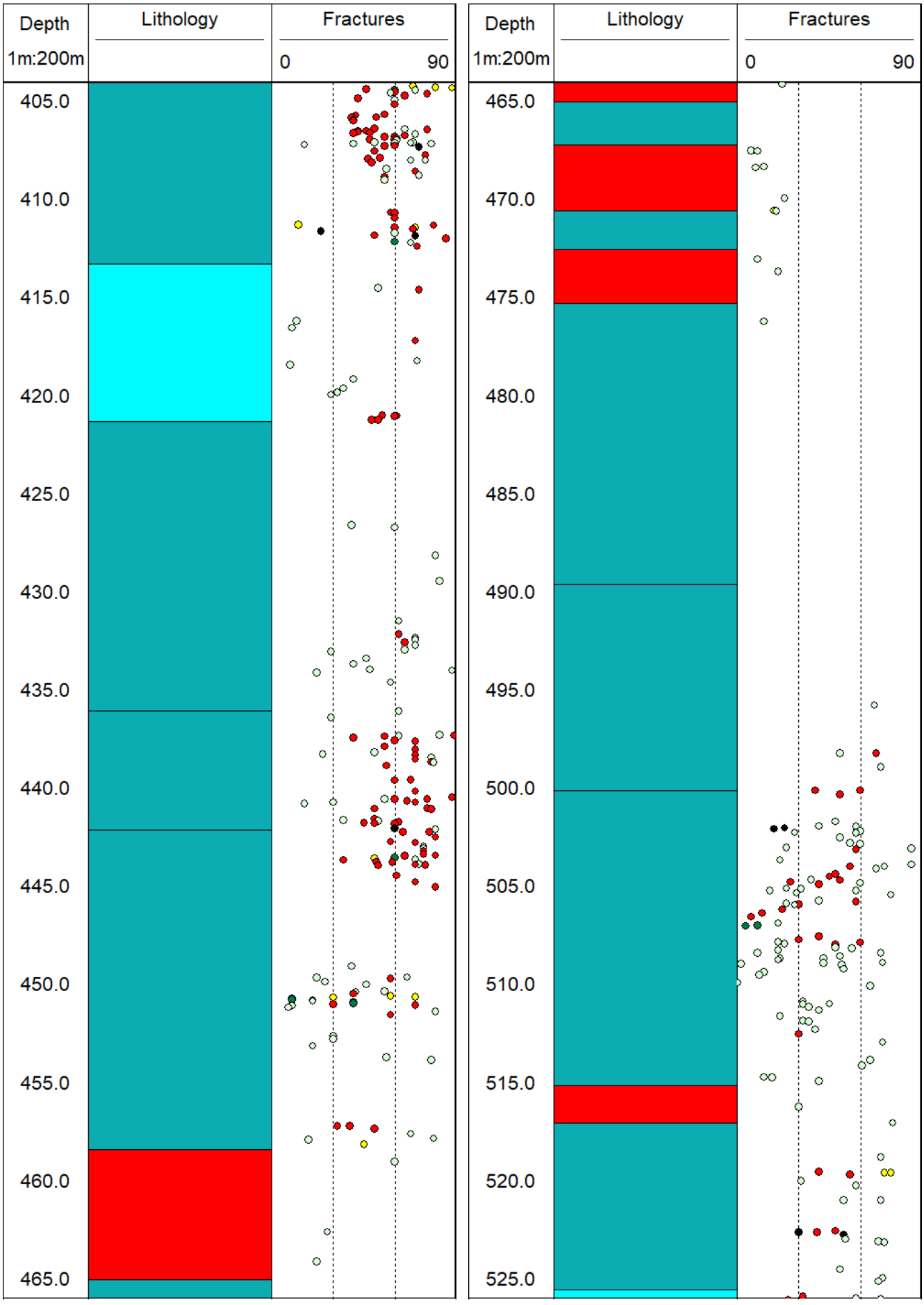
Depth
1m:200m
Lithology
Fractures
0
90
405.0
410.0
415.0
420.0
425.0
430.0
435.0
440.0
445.0
450.0
455.0
460.0
465.0
Depth
1m:200m
Lithology
Fractures
0
90
465.0
470.0
475.0
480.0
485.0
490.0
495.0
500.0
505.0
510.0
515.0
520.0
525.0

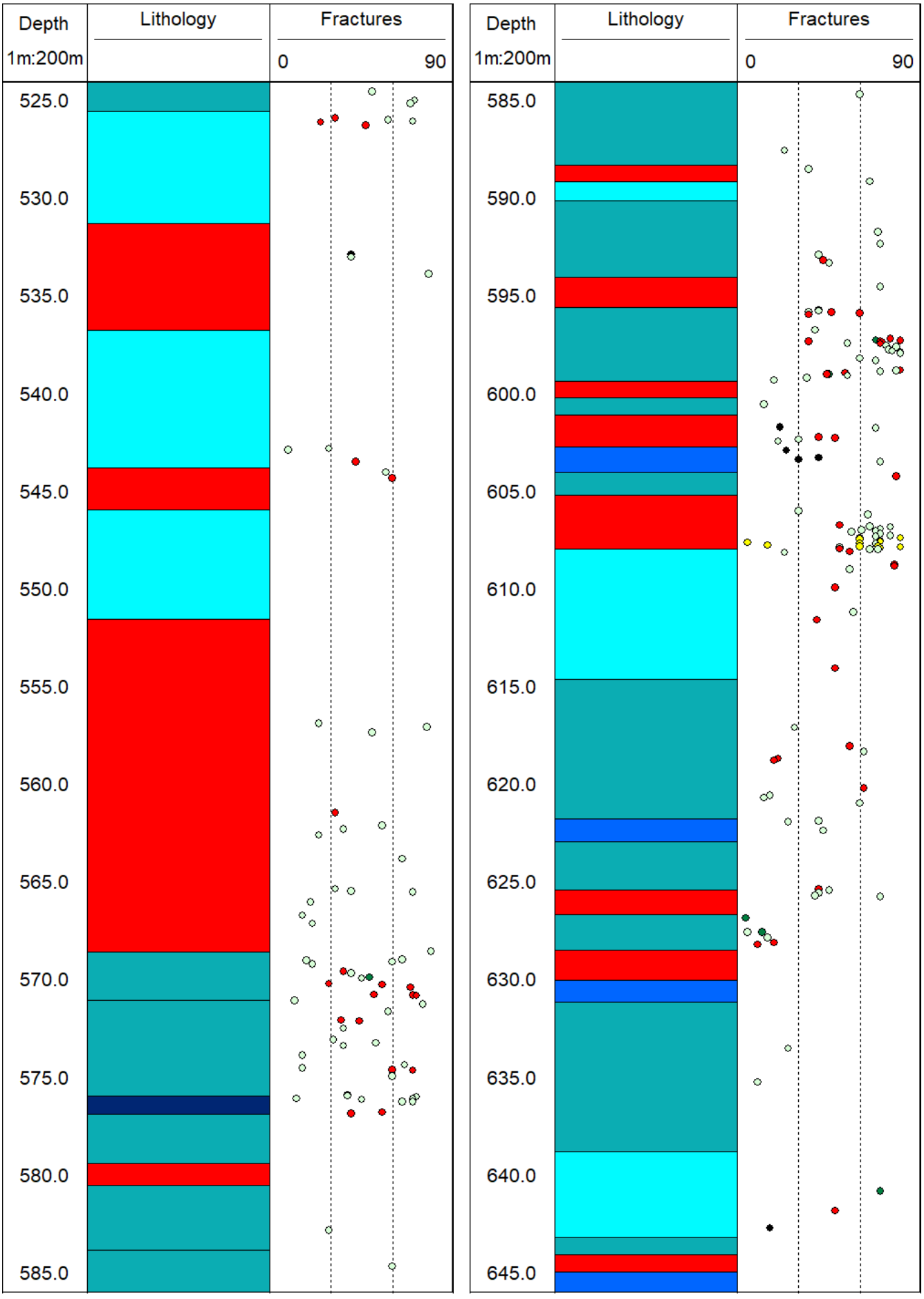
Depth
1m:200m
Lithology
Fractures
0
90
525.0
530.0
535.0
540.0
545.0
550.0
555.0
560.0
565.0
570.0
575.0
580.0
585.0
Depth
1m:200m
Lithology
Fractures
0
90
585.0
590.0
595.0
600.0
605.0
610.0
615.0
620.0
625.0
630.0
635.0
640.0
645.0